Plasma Physics and Controlled Fusion

TOPICAL REVIEW

Polarization of incoherent Thomson scattering for electron temperature measurement

To cite this article: V V Mirnov and D J Den Hartog 2017 *Plasma Phys. Control. Fusion* **59** 063001

View the article online for updates and enhancements.

Related content

- On the calibration of polarimetric Thomson scattering by Raman polarimetry
L Giudicotti and R Pasqualotto
- Polarimetric Thomson scattering for high T_e fusion plasmas
L. Giudicotti
- A primer on the theory of Thomson scattering for high-temperature fusion plasmas
S L Prunty

Recent citations

- The energy tree: Non-equilibrium energy transfer in collision-dominated plasmas
He-Ping Li *et al*
- Relativistic electron kinetic effects on laser diagnostics in burning plasmas
V.V. Mirnov and D.J. Den Hartog
- First observation of the depolarization of Thomson scattering radiation by a fusion plasma
L. Giudicotti *et al*

IOP ebooks™

Bringing you innovative digital publishing with leading voices to create your essential collection of books in STEM research.

Start exploring the collection - download the first chapter of every title for free.

This content was downloaded from IP address 128.104.165.51 on 09/11/2018 at 20:20

IOP Publishing Plasma Physics and Controlled Fusion
Plasma Phys. Control. Fusion **59** (2017) 063001 (32pp) https://doi.org/10.1088/1361-6587/aa61e2

Topical Review

Polarization of incoherent Thomson scattering for electron temperature measurement

V V Mirnov and D J Den Hartog

Department of Physics and the Center for Magnetic Self-Organization in Laboratory and Astrophysical Plasmas, University of Wisconsin—Madison, Madison, WI 53706, United States of America

E-mail: vvmirnov@wisc.edu

Received 30 August 2016, revised 10 February 2017
Accepted for publication 21 February 2017
Published 25 April 2017

Abstract

This paper reviews the polarization properties of Thomson scattered (TS) light as applied to electron temperature measurement. The theoretical background is based on Stokes vector transformations and Mueller matrices. The review starts from scattering on a single electron and proceeds to the combined effect of many particles. Then, this general approach is subdivided into frequency-integrated and frequency-resolved applications. For each of them, the exact relativistic analytical solutions are presented in the form of Mueller matrix elements averaged over the relativistic Maxwellian distribution function. The dependencies of the elements on the scattering angle, electron temperature, and frequency of the scattered radiation (in the frequency-resolved case) are presented. These solutions form the basis for accurate analysis of the degree of depolarization of TS radiation. Results obtained for the frequency-integrated regime are reviewed and new solutions for the frequency-resolved case are reported, making a bridge between the two limiting cases. Experimental setups for polarization-based TS diagnostics are compared. A combination of polarization-based and spectral-based techniques are also described.

Supplementary material for this article is available online

Keywords: incoherent Thomson scattering, electron temperature, measurement

(Some figures may appear in colour only in the online journal)

1. Introduction

The incoherent Thomson scattering (TS) of monochromatic laser light is the basis for a plasma diagnostic widely used to measure electron temperature. The electron temperature, T_e, is proportional to the square of the frequency width of the scattered spectrum [1]. The finite spectrum width is produced by the Doppler shift of the frequency of the incident monochromatic wave in the reference frame of an electron moving with a thermal velocity v_{Te}. At small photon energies compared to the electron rest mass energy the scattering in this reference frame occurs almost elastically but with a change in the photon propagation direction. Due to the change of direction, the inverse transformation to the laboratory reference frame results in a scattered photon frequency different from the original incident frequency, and the difference is proportional to the electron thermal velocity. Thus, the Doppler effect and the corresponding frequency shift lead to the spectrum broadening observed in the standard frequency-based TS method of T_e measurement.

An electromagnetic wave is characterized not only by wave frequency but also by wave polarization. Instead of frequency spectrum broadening, we analyze in this paper the polarization properties of TS radiation as a method of electron temperature measurement. The change in the polarization of the scattered

 © 2017 IOP Publishing Ltd Printed in the UK

light is significant in high-temperature plasmas, and must be accounted for when analyzing the scattered radiation for temperature measurement. It has been typically characterized in TS literature by the relativistic depolarization factor q (see [1–4]). When the scattered light collection system selects for a specific orientation of linear polarization, as is often the case, the factor q quantifies the reduction of the collected spectral intensity due to changes in the polarization of the incident linearly polarized laser light. The factor q arises from relativistic terms $\propto v_{Te}^2/c^2$ in the polarization part of the scattering operator. The origin of the relativistic terms is thoroughly analyzed in [5]. The full set of equations of special relativity is used to transform the scattered electromagnetic fields from the reference frame of the electron at rest to the observer where the electron is assumed to move with an arbitrary relativistic velocity.

Although q is referred to as a depolarization factor, this nomenclature differs from the use of depolarization in the present paper. For example, the previously mentioned reduction in scattered light intensity occurs even for scattering from a single moving electron. In such a case, the scattered electromagnetic wave is Doppler-shifted in frequency but remains monochromatic and completely polarized. The transition from fully-polarized incident light to partially-polarized scattered light is caused by the superposition effect of a large number of randomly moving electrons. It results in broadening of the frequency spectrum and also renders the scattered radiation partially polarized even though the incident light is fully polarized. We focus our attention on this mechanism of loss of polarization in the process of incoherent TS.

It is generally applicable to quantify the loss of polarization by the *degree of polarization* P, or equivalently by the *degree of depolarization* $D = 1 - P$. The possibility of determining the plasma electron temperature by measuring the degree of depolarization was suggested as early as 1968 in [6] and more recently in [7]. If the degree of polarization dependence on electron temperature is accurately known from theory, the accuracy of such a diagnostic could potentially exceed that of the conventional spectrum-based TS method. First order in T_e/m_ec^2 effects were analyzed theoretically in [6, 8, 9].

The most general and complete description of TS radiation is based on Mueller matrix formalism. The 4×4 Mueller matrix links the Stokes vectors of the incident and scattered light and gives full information about the power and polarization of the scattered wave for arbitrary polarization of the incident wave. The use of this formalism for the TS applications was first suggested by Segre and Zanza in [9] in 2000. Although their calculations were limited to first order terms in $T_e/m_ec^2 \ll 1$ and performed with an incorrect form of the scattering operator, the paper was of a fundamental importance as it illustrated the powerful capabilities of the Mueller matrix approach. This work motivated further interest and progress in theoretical studies devoted to polarization effects and their application to advanced polarization-based TS diagnostics.

Reference [10] was built on this previous work and presented exact analytical relativistic solutions for the frequency-integrated Mueller matrix elements. This result was applied to the LIDAR ITER Thomson scattering system. The analytical solutions enable optimization of a polarization-based TS diagnostic setup over multidimensional parameter space. These solutions were used to study the general properties of the degree of depolarization in a wide range of T_e and scattering angle θ variations [11, 12]. Possible implementations of a polarization-based T_e diagnostic were discussed in [13].

Earlier publications [10–12] were mostly devoted to parametric studies of the degree of polarization. In all these papers, expressions for the Mueller matrix elements were used without derivation. A self-consistent theoretical model of TS polarization and the method of derivation of the exact relativistic expressions were described recently in [14]. The frequency integrated Mueller matrix solutions are expressed in a compact form after analytical integration of the three-dimensional, relativistic scattering operator over a relativistic Maxwellian distribution function and universally valid for the full range of electron thermal motion from non-relativistic to ultra-relativistic.

The topic of the TS polarization is not well known in plasma community. We present many details in order to make the article self-contained and readable without the need for frequent use of references. A description of the general polarization formalism is given in section 2. In section 3, the review begins with the key elements of the theoretical approach presented in [14].

The polarization properties for incoherent Thomson scattering from a single electron provide a convenient starting point, and are described in section 3.1 by the Lienard–Wiechert solution for the scattered electric field re-emitted by an electron moving along an unperturbed trajectory with arbitrary relativistic velocity and oscillating in the field of the incident monochromatic wave. The important element of the Mueller matrix formalism developed in [14] is a transformation of the time averaging in the definition of the Stokes vector components to integration over the spectrum. The resulting expressions are linked with the frequency-integrated products of the Fourier components of the truncated fields. A set of three Mueller matrices and corresponding Stokes vectors (auxiliary, spectral, and frequency integrated) are introduced in section 3.2. They describe the change of polarization in the process of scattering on an individual electron moving in unbounded space.

The zero-component of the spectral Stokes vector corresponds to the spectral intensity from a single electron. The result of [14] for this component is consistent with the expression in the first part of [15] devoted to the infinite scattering volume (infinite transit time, ITT) case. It yields the spectral intensity on the detector $P^{(\mathrm{single})}(\omega) \propto \delta(\omega - \omega_d)/(1 - \beta_s)^6$ scattered by a single electron moving with the velocity $\boldsymbol{\beta} = \mathbf{v}/c$ in the infinite scattering volume where β_s is the projection of $\boldsymbol{\beta}$ on the scattered wave direction and ω_d is the Doppler shifted frequency of the wave. The key dependencies of $P^{(\mathrm{single})}(\omega)$ on ω and β_s are also identical to equation (7.2.19) in [2] and equation (4.35) in [16]. According to the terminology of [2] the spectral intensity $P^{(\mathrm{single})}(\omega)$ represents the *time-at-observer* power from a single electron. The complicated polarization factor in the expression for $P^{(\mathrm{single})}(\omega)$ was additionally verified in [14] by comparison of the frequency integrated solution with the scattering cross section presented in the classical book by Landau and Lifshitz [17].

This special attention paid to verification was caused by disagreement about proper solution for $P^{(\mathrm{single})}(\omega)$ (see, for example, [1, p 53 and 5, p 488] and the opposite conclusion made in [14]). The confusion arose because the result of [15] was declared in [18] to be incorrect due to improper handling of the square of a δ-function in the derivation of the spectral power equation. The arguments in [18] were reviewed recently in a detailed tutorial article [16]. In point of fact, the square of the δ-function is properly treated in [15]. The inconsistency between [18] and [15] originates not from a mathematical mistake in [15] but from the erroneous comparison of the *time-at-particle* power treated in [18] with the *time-at-observer* power analyzed in [15]. This issue is reviewed in section 3.3 with mathematical arguments shown in appendix A.3.

The single electron Mueller matrices obtained in section 3 are used as an elementary process to account for the combined effect of many particles as reviewed in section 4. The effect of many electrons was originally expressed in [15] by two different weighting factors used for averaging over Maxwellian distribution function: by the weighting factor $P_{\mathrm{ITT}} \propto (1-\beta_s)^{-6}$ presented in the first ITT part of [15] and another scaling, $P_{\mathrm{FTT}} \propto (1-\beta_s)^{-5}$, derived in the second part of [15] devoted to the finite scattering volume (finite transit time, FTT) regime. The ITT scaling corresponds to the instantaneous spectral intensity $P^{(\mathrm{single})}(\omega)$ multiplied by the number of particles (assumed stationary) residing in the scattering volume. This operation is invalid in the case of a finite scattering volume due to the interruption of radiation caused by the boundaries of the scattering zone. The FTT scaling has an additional factor $(1-\beta_s)$ compared to the ITT expression. This factor takes into account modification of the mean power on the detector due to the impulsive character of the scattered radiation. The quantitative justification of this effect is illustrated in section 3.1. The FTT form of the weighting factor is generally accepted in all present-day relativistic treatments of TS radiation. This expression was used in [14] while the incorrect ITT weighting factor was used for averaging over Maxwellian distribution function in [9].

The method of exact integration over the relativistic Maxwellian distribution function is presented in detail in [14] for the case of the frequency integrated Mueller matrix. It is discussed briefly in section 5.1. The frequency integrated quantities and the properties of the corresponding degree of depolarization are reviewed in section 5.2. The technique of exact integration can also be formally applied to the ITT weighting factor used in [9]. This also yields Mueller matrix elements valid at all temperatures, and are discussed in section 5.3 and appendix B. Their low temperature limits verify the first-order expansions in T_e obtained in [9] for the ITT model, and increases confidence in both the first-order calculations in [9] and the correctness of the scheme of exact analytical integration.

The general formalism of the Mueller matrix and Stokes vectors is subdivided into the frequency-integrated and frequency-resolved applications. The frequency-integrated analysis is fully covered in [14]. For completeness new exact relativistic solutions are obtained and presented in section 6 for the frequency-resolved Mueller matrix. The verification of these new results is confirmed analytically and numerically by integrating over the entire frequency interval and comparing with the frequency-integrated quantities [14]. The correctness is also confirmed by full consistency of the spectral powers calculated from the newly derived general equations with the previous exact relativistic spectral power calculations reported in [3].

The present overview is focused on theoretical results obtained during the last two decades and practical realizations of polarization-based TS diagnostics. There are a number of publications [13, 19–22] describing the optimization of their potential capabilities. Variations of polarization-based TS diagnostics are compared, searching for the variant with the smallest experimental error bars. Combinations of polarization-based and spectral-based techniques are discussed in section 7, including the hybrid method suggested recently by Giudicotti and co-authors [22] for the ITER core TS system.

Brief concluding remarks related to the ITER core TS system are made in the summary. The polarization TS method, however, is not applicable only to high electron temperature burning plasmas such as in ITER. In addition to the ITER core TS application there are a number of other opportunities for implementing polarization-based Thomson scattering diagnostics. Although these methods have not yet been fully investigated in experiments, an attempt to measure the depolarization effect has recently been performed on JET. In addition to JET, an experiment to measure the depolarization of the TS radiation has been proposed on the Frascati Tokamak Upgrade (FTU). This information as well as a possible experimental test of a polarimetric Thomson scattering diagnostic technique on the W7-X stellarator are briefly discussed in the summary. Finally, we conclude by identifying the various problems that still remain open to investigation in this area.

2. General description of polarized light

TS radiation is always contained in a finite frequency bandwidth $\Delta\omega$. Consider a plane wave propagating along the z-axis and let ω be some average frequency such that the wave electric field is proportional to $\mathbf{E}(t)\exp(-\mathrm{i}\omega t)$ where the complex amplitude $\mathbf{E}(t)$ is some slowly varying function of time responsible for the frequency broadening $\Delta\omega$. For a pure monochromatic wave $\mathbf{E}(t)$ is a constant. In this case, the tip of the electric field vector rotates in the xy-plane describing an ellipse that is called the polarization ellipse. Thus, every pure monochromatic wave is, by definition, completely polarized.

For a non-monochromatic wave, the electric field vector at a given point z is a superposition of oscillations with different frequencies. Since $\mathbf{E}(t)$ determines the size and the inclination angle of the polarization ellipse, its shape changes with time. Such a wave is partially polarized. The resulting tip of the electric field vector describes, as a function of time, a trajectory like that shown in figure 1. The polarization properties of a non-monochromatic plane wave are characterized

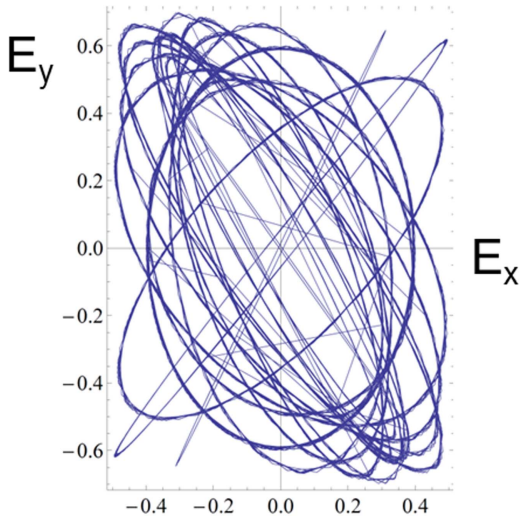

Figure 1. Example of trajectory of the tip of the electric field vector at given point z, as a function of time, for partially polarized non-monochromatic wave with $\Delta\omega/\omega \simeq 0.1$ and $P \simeq 0.85$. The electric field is in arbitrary units.

by a 2×2 complex Hermitian coherency matrix $\mathbf{J}$, called also the polarization tensor. The matrix is constructed from time averaged quadratic combinations of the field components (see [23]). It is represented, in general, by four real quantities which are equivalently expressed by four Stokes parameters or the 4-component Stokes vector $\mathbf{S}$

$$\hat{\mathbf{J}} = \begin{pmatrix} \langle E_x E_x^\star \rangle & \langle E_x E_y^\star \rangle \\ \langle E_y E_x^\star \rangle & \langle E_y E_y^\star \rangle \end{pmatrix} = \frac{1}{2}\begin{pmatrix} S_0 + S_1 & S_2 + \mathrm{i}S_3 \\ S_2 - \mathrm{i}S_3 & S_0 - S_1 \end{pmatrix}. \quad (1)$$

The S_0 component is a measure of the total intensity I of the wave and the remaining components describe the polarization properties. For a purely monochromatic, fully polarized incident wave, the amplitudes and the phases of E_x and E_y are independent of time so that $\langle E_x E_x^\star \rangle = |E_x|^2$, $\langle E_y E_y^\star \rangle = |E_y|^2$, $\langle E_x E_y^\star \rangle = E_x E_y^\star$, $\langle E_y E_x^\star \rangle = E_y E_x^\star$. In this case, $\det\ |\hat{\mathbf{J}}| = 0$ is equivalent to the relationship $S_0^2 = S_1^2 + S_2^2 + S_3^2$. Due to this connection between the components, the state of polarization of the incident laser light used in Thomson scattering systems, and the evolution of the polarization of monochromatic laser light used for interferometric/polarimetric diagnostics, is often described by the three-component unit Stokes vector S_i/S_0 $(i = 1, 2, 3)$. This unit vector is characterized by the azimuth (orientation angle) of the polarization ellipse $0 \leqslant \psi < \pi$ and the ellipticity angle $\chi = \pm\arctan(b_2/b_1)$ determined by the ratio of the minor and the major semi-axis $(-\pi/4 < \chi \leqslant \pi/4)$. In this paper, we use the full four-component Stokes vector $\mathbf{S}^{(i)}$ to characterize monochromatic incident laser light with arbitrary elliptical polarization described by equation (11). Following the transformations in appendix A.1 yields $\mathbf{S}^{(i)}$ in the form

$$\mathbf{S}^{(i)} = E_0^2(1,\ \cos 2\psi \cos 2\chi,\ \sin 2\psi \cos 2\chi,\ \sin 2\chi). \quad (2)$$

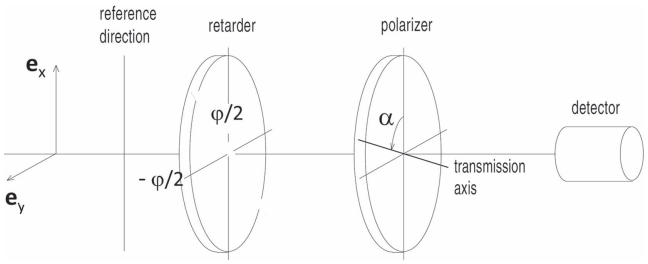

Figure 2. Schematic representation of the experimental setup for the measurement of the Stokes vector polarization components.

Consider now the opposite case of fully unpolarized or natural light. The complete absence of polarization means that all directions in the xy-plane are equivalent, $\langle E_x E_x^\star \rangle = \langle E_y E_y^\star \rangle$, and the E_x and E_y components are uncorrelated, $\langle E_x E_y^\star \rangle = \langle E_y E_x^\star \rangle = 0$. Correspondingly, a fully unpolarized wave is characterized by zero values of the three Stokes vector components $S_1 = S_2 = S_3 = 0$. Any partially polarized wave can be decomposed into completely unpolarized and polarized portions. As they are statistically independent, the 4-component Stokes vector of the mixture is a sum of the respective vectors of the separate waves. Defining the unpolarized and polarized parts as $\mathbf{S}^{(\mathrm{unpol})} = (S_0 - \sqrt{S_1^2 + S_2^2 + S_3^2},\ 0,\ 0,\ 0)$ and $\mathbf{S}^{(\mathrm{pol})} = (\sqrt{S_1^2 + S_2^2 + S_3^2},\ S_1,\ S_2,\ S_3)$ yields the degrees of polarization and depolarization of the total wave field of intensity $I_{\mathrm{tot}} = S_0$. The degree of polarization is determined by the relative intensity I_{pol} of the polarized component

$$P = \frac{I_{\mathrm{pol}}}{I_{\mathrm{tot}}} = \frac{\sqrt{S_1^2 + S_2^2 + S_3^2}}{S_0}, \quad D = 1 - P, \quad (3)$$

where $D = I_{\mathrm{un}}/I_{\mathrm{tot}}$ is the degree of depolarization defined as the relative intensity of the unpolarized component [23].

The degree of polarization P varies from the value $P = 0$ for unpolarized to $P = 1$ for fully polarized light. The fact that $P \leqslant 1$ for any arbitrary polarization is equivalent to the inequality $\det\ |\hat{\mathbf{J}}| \geqslant 0$. To prove this general property, consider the complex quantity $\mathcal{A}$ defined in [24] by

$$\mathcal{A} = E_y(t)\langle E_x(t)E_x^\star(t)\rangle - E_x(t)\langle E_y(t)E_x^\star(t)\rangle. \quad (4)$$

For the average value of its square modulus we obtain

$$\langle|\mathcal{A}|^2\rangle = \langle E_x(t)E_x^\star(t)\rangle(\langle E_x(t)E_x^\star(t)\rangle\langle E_y(t)E_y^\star(t)\rangle - \langle E_x(t)E_y^\star(t)\rangle\langle E_y(t)E_x^\star(t)\rangle) = \langle E_x(t)E_x^\star(t)\rangle \det|\mathbf{J}| \geqslant 0. \quad (5)$$

It is clear that $\det\ |\hat{\mathbf{J}}| = (S_0^2 - S_1^2 - S_2^2 - S_3^2)/4$ is non-negative, i.e., $P \leqslant 1$ in equation (3).

The Stokes vector components and, correspondingly, the degree of polarization or depolarization can be measured by several different techniques. The usual measurement method is illustrated in figure 2 which shows a monochromatic wave (A6) incident on a polarization element called a retarder. The retarder has the property that the phase of the E_x component is advanced by $\phi/2$ and the phase of the E_y component is retarded by $\phi/2$. Then, the electric field components E_x and E_y emerging from

the retarder are modified as $E_x' = E_x \exp(\mathrm{i}\phi/2)$, $E_y' = E_y \exp(-\mathrm{i}\phi/2)$. The modified electromagnetic wave is incident on a polarizer which has a transmission axis that forms an angle α with the x-direction. Only the component of the electric field $\mathbf{E}'$ aligned with the α-direction is transmitted perfectly while there is a complete suppression of all other components. Thus, the total electric field transmitted along the α-direction is the sum of the two contributions $E_\alpha = E_x' \cos\alpha + E_y' \sin\alpha$. Taking the complex conjugate of E_α and forming the product $I(\alpha, \phi) = E_\alpha E_\alpha^\star$ yields the intensity of the passing light in terms of the Stokes vector components (1)

$$I(\alpha, \phi) = \frac{1}{2}(S_0 + S_1 \cos(2\alpha) + S_2 \cos\phi \sin(2\alpha) - S_3 \sin\phi \sin(2\alpha)). \quad (6)$$

The first three components can be measured without the retarder by rotating the transmission axis of the polarizer to the angles $\alpha = 0°,\ 45°$ and $90°$. The last component is measured with the use of the quarter-wave retarder with $\phi = 90°$ and the polarizer placed at $\alpha = 45°$. Solving four equations obtained from (6) by specifying different angles in arguments of $I(\alpha, \phi)$ yields all Stokes vector components

$$\begin{aligned} S_0 &= I(0°, 0°) + I(90°, 0°), \\ S_1 &= I(0°, 0°) - I(90°, 0°), \\ S_2 &= -I(0°, 0°) - I(90°, 0°) + 2I(45°, 0°), \\ S_3 &= I(0°, 0°) + I(90°, 0°) - 2I(45°, 90°). \end{aligned} \quad (7)$$

Detailed information about other measurement techniques is presented in [25, 26].

For any superposition of uncorrelated oscillations the polarization matrices add up. The inverse expansion into a sum of uncorrelated oscillations is not unique. As pointed out in [27] the inverse expansion can be made unique with the addition of some constraints. An important example of this type of constraint is the representation of a given vector field as a sum of two uncorrelated oscillations: completely unpolarized and completely polarized, such that

$$\hat{\mathbf{J}} = \hat{\mathbf{J}}^{(\mathrm{un})} + \hat{\mathbf{J}}^{(\mathrm{pol})},\ \hat{\mathbf{J}}^{(\mathrm{un})} = \begin{pmatrix} A & 0 \\ 0 & A \end{pmatrix},\ \hat{\mathbf{J}}^{(\mathrm{pol})} = \begin{pmatrix} B & D \\ D^\star & C \end{pmatrix}, \quad (8)$$

where A, B and C are nonnegative and the determinant of the fully polarized part, $\hat{\mathbf{J}}^{(\mathrm{pol})}$, is required to be zero, $BC - DD^\star = 0$. This relationship together with four components of the matrix equation leads to five equations for five unknown coefficients in equation (8). Of the two roots of the quadratic equation for A (both of them are real and nonnegative) there is only one root for which B and C are nonnegative. This yields a unique decomposition of an arbitrary field as a superposition of the completely unpolarized and polarized fractions.

The factors B, C and D in the polarized part $\hat{\mathbf{J}}^{(\mathrm{pol})}$ are functions of the elements of the matrix $\hat{\mathbf{J}}$ or, equivalently, of the Stokes vector components of the total field. They are given in explicit form by equation (A5). This alternative derivation confirms the validity of expression (3) for P. The second product of the derivation is the characteristics of the polarization ellipse associated with the completely polarized part $\hat{\mathbf{J}}^{(\mathrm{pol})}$. They are expressed in terms of the Stokes parameters of the total radiation field as follows

$$\sin(2\chi) = \frac{S_3}{\sqrt{S_1^2 + S_2^2 + S_3^2}},\quad \tan(2\psi) = \frac{S_2}{S_1}. \quad (9)$$

When applied to the fully polarized incident radiation (11), these solutions are reduced to identities confirming consistency of the approach but they give non-trivial information for partially polarized TS radiation.

This brief review illustrates the main ideas and computational steps needed for decomposing arbitrary electromagnetic radiation to fully unpolarized and completely polarized components. In practical terms, it gives expressions for the degree of polarization and characteristics of the polarization ellipse associated with the fully polarized fraction. In the case of Thomson scattering, the Stokes vector of the scattered radiation depends on the geometry of the experiment, plasma parameters and polarization of the incident laser light. We consider now how the Stokes parameters of the scattered field $\mathbf{S}^{(s)}$ are connected with the properties of the incident light. The most general method for the calculations $\mathbf{S}^{(s)}$ is based on the 4×4 Mueller matrix that expresses the Stokes vector of the scattered radiation in terms of the Stokes vector $\mathbf{S}^{(i)}$ of fully polarized incident laser light. Following [14], we will discuss the key elements of the method and review the results obtained within the scope of classical electrodynamics, where the scattering of the waves is treated as a re-emission of electromagnetic radiation by free electrons oscillating in the electric and magnetic fields of the incident laser light.

3. Thomson scattering from a single electron

3.1. Electric field from a single electron

Using the Lienard–Wiechert potentials, the scattered electric field in the far-zone $\mathbf{E}_s(\mathbf{r}, t)$ is expressed by a 2×2 matrix $\hat{\mathbf{\Pi}}$ transforming the incident field components (E_{ix}, E_{it}) to the scattered field components (E_{sx}, E_{st}) in the process of interaction with a single electron moving with velocity $\mathbf{v}$ (see appendix A.4). The electric fields are projected, respectively, on the unit vectors $(\mathbf{e}_x,\ \mathbf{t}_i)$ and $(\mathbf{e}_x, \mathbf{t}_s)$ which are orthogonal to the wave propagation directions $\mathbf{i} = \mathbf{k}_i/|\mathbf{k}_i|$ and $\mathbf{s} = \mathbf{k}_s/|\mathbf{k}_s|$

$$\begin{aligned} &\mathbf{E}_i = E_{ix}\mathbf{e}_x + E_{it}\mathbf{t}_i,\quad \mathbf{E}_s = E_{sx}\mathbf{e}_x + E_{st}\mathbf{t}_s, \\ &\mathbf{t}_i = \mathbf{i} \times \mathbf{e}_x = \frac{\mathbf{i}\cos\theta - \mathbf{s}}{\sin\theta},\quad \mathbf{t}_s = \mathbf{s} \times \mathbf{e}_x = \frac{\mathbf{i} - \mathbf{s}\cos\theta}{\sin\theta}, \end{aligned} \quad (10)$$

where θ is the scattering angle in the scattering plane determined by the vectors $\mathbf{i}$ and $\mathbf{s}$ while the unit vector $\mathbf{e}_x = [\mathbf{i} \times \mathbf{s}]/\sin\theta$ is normal to the scattering plane. The Stokes vector of the incident wave is calculated in the incident wave reference frame $(\mathbf{e}_x, \mathbf{t}_i, \mathbf{i})$ while the Stokes vector of the scattered wave is defined by equation (A1) in the scattering wave reference frame $(\mathbf{e}_x, \mathbf{t}_s, \mathbf{s})$. A schematic illustration showing orientation of the vectors $\mathbf{s}$, $\mathbf{i}$, $\mathbf{t}_s$ and $\mathbf{t}_i$ in the scattering plane and vector $\mathbf{e}_x$ perpendicular to the scattering plane is presented in figure 3.

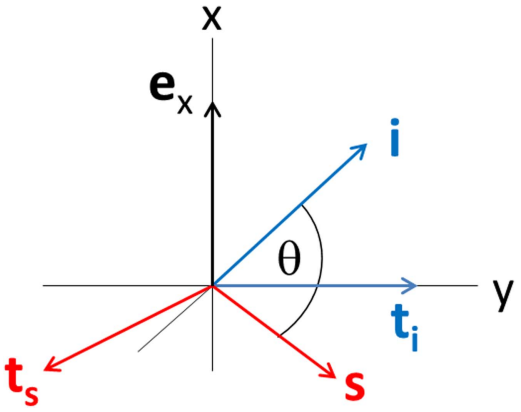

Figure 3. Basic unit vectors used for electric field projection and Stokes component calculation of the incident ($\mathbf{e}_x$, $\mathbf{t}_i$, $\mathbf{i}$) and scattered ($\mathbf{e}_x$, $\mathbf{t}_s$, $\mathbf{s}$) waves.

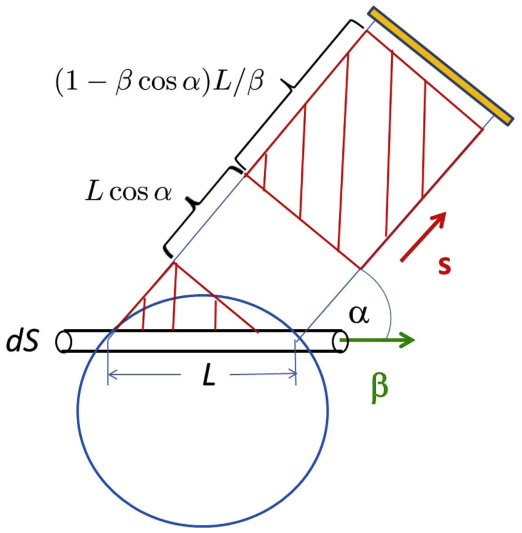

Figure 4. Snapshot of the area occupied by radiation (red) emitted in the direction $\mathbf{s}$ toward the remote detector (yellow) during one passage through the scattering volume (blue) of a single electron moving with velocity $\boldsymbol{\beta} = \mathbf{v}/c$ such that $\cos\alpha = \boldsymbol{\beta}\cdot\mathbf{s}/\beta > 0$. L is the length between the entrance and the exit points of the scattering volume (suggested by Stupakov [28]).

The fully polarized incident monochromatic wave is assumed to have an arbitrary elliptical polarization, with semi-major axis b_1 and semi-minor axis b_2, and complex amplitude $\mathbf{E}_i$

$$\mathcal{E}_i(\mathbf{r}', t') = \mathbf{E}_i \exp(\mathrm{i}\mathbf{k}_i\cdot\mathbf{r}' - \mathrm{i}\omega_i t'),$$
$$\mathbf{E}_i = E_0(b_1\mathbf{e}'_x + \mathrm{i}b_2\mathbf{e}'_y)\Big/\sqrt{b_1^2+b_2^2}, \qquad (11)$$

where E_0 is the magnitude of the incident wave. The two mutually perpendicular unit vectors $\mathbf{e}'_x$ and $\mathbf{e}'_y$ are orthogonal to $\mathbf{i}$ and aligned with the semi-axes of the polarization ellipse. Their position with respect to the scattering plane is characterized by the azimuth ψ (orientation angle) between $\mathbf{e}_x$ and $\mathbf{e}'_x$ ($\cos\psi = \mathbf{e}_x\cdot\mathbf{e}'_x$).

The prime symbol for variables t' and $\mathbf{r}'$ indicates the retarded time and electron position inside the scattering volume while the variables t and $\mathbf{r}$ are related to the time at the remote detector (observer) localized at the position $\mathbf{r}$. The radius vector $\mathbf{r}$ connects the origin of the coordinate system chosen somewhere in the center of the scattering volume with the point of observation. At large r one can approximate the distance R between an individual electron at the position $\mathbf{r}'(t')$ and the point of observation as $R(t') \simeq r - \mathbf{r}'(t')\cdot\mathbf{s}$. The fields at the point of observation are determined by the position of the electron at the earlier time t' such that $t = t' + R(t')/c$. Differentiating this relation over t and t' yields the relationship for the time interval Δt between arrival at the observer of signals which were emitted by the electron over an interval $\Delta t'$ in the scattering volume

$$\Delta t = (1-\beta_s)\Delta t', \qquad (12)$$

where $\beta_s = \mathbf{v}\cdot\mathbf{s}/c$. The change of the interval is caused by both the effect of retardation and electron thermal motion toward or away from the observer. This leads to different powers emitted by the electron and received by the observer. If the scattered power at the observer is $P^{(\mathrm{observer})}$ then the energy received by the observer during the time interval Δt is $P^{(\mathrm{observer})}\Delta t$. Since the same energy is emitted by the electron during the *time-at-particle* interval $\Delta t'$, the *time-at-particle* power introduced in [2] is different from the *time-at-observer* power

$$P^{(\mathrm{particle})} = P^{(\mathrm{observer})}(1-\beta_s). \qquad (13)$$

Consider, for example, a single electron moving from left to right through the scattering volume. The scattering volume is defined by the intersection of the region occupied by the laser beam in the direction perpendicular to the beam and the region of observation determined by the collection optics. Each electron re-emits the wave when it enters the section of the length L inside the scattering volume. The duration of the re-emission equals the transit time L/v which corresponds to the *time-at-particle* interval $\Delta t'$. The mechanism of the pulse length change on the detector is illustrated graphically in figure 4 for the case $\beta_s > 0$, from which it follows that the duration at the detector, $\Delta t = (1-\beta_s)L/v$, is shorter than L/v. Indeed, far from the scattering volume, the leading and the trailing edges are almost perpendicular to the propagation direction. The rectangular area occupied by the emitted radiation is shown by red color in figure 4. Subtracting coordinates of the leading ($Lc/v + ct$) and trailing ($L\cos\alpha + ct$) edges yields the length of the rectangular $cL(1-\beta_s)/v$ and the time $\Delta t = L(1-\beta_s)/v$ during which the radiation passes through the detector. This time is consistent with the general relationship (12).

During time interval Δt, the detector receives the instantaneous power denoted as $P^{(\mathrm{observer})}$ in equation (13). When the first electron leaves the scattering volume a second one enters this area and starts emitting radiation shown by the red triangle in figure 4. The replacement of the electrons forms a gap of the length $L\cos\alpha$ between the propagating pulses. As a result, the radiation is not continuous on the detector but has the form of discrete pulses. During the gap, the detector receives no power so that the mean power

$\overline{P}^{(\mathrm{observer})}$ for the whole cycle is

$$\overline{P}^{(\mathrm{observer})} = \frac{P^{(\mathrm{observer})}\Delta t}{\Delta t + L\cos\alpha/c} = P^{(\mathrm{observer})}(1-\beta_s) = P^{(\mathrm{particle})}. \quad (14)$$

Note that the electrons moving in the opposite direction with the velocity $-\boldsymbol{\beta}$ such that $\beta_s = \boldsymbol{\beta}\cdot\mathbf{s} < 0$ result in partial overlap of the pulses with $\overline{P}^{(\mathrm{observer})} > P^{(\mathrm{observer})}$.

The modification of the mean power on the detector compared to its instantaneous value $P^{(\mathrm{observer})}$ is caused by the finite size of the scattering volume and referred as to the finite transit time effect (FTT). The FTT effect and a physical explanation similar to figure 4 were described in [15]. Following [14] we first discuss the scattering on a single electron moving in unbounded space filled with an incident homogeneous plane electromagnetic wave of infinite extent. The correction factor $1-\beta_s$ due to the FTT effect is incorporated into the calculations at the stage of averaging over electron distribution function.

An infinitely long wave packet of incident monochromatic radiation (11) is characterized by non-zero incident and scattered electric fields at $-\infty \leqslant t \leqslant \infty$. Instead of using the time-dependent scattered field $\mathbf{E}_s(\mathbf{r}, t)$, we operate with the Fourier transformed truncated electric field $\mathbf{E}_s^{(T)}(\mathbf{r}, \omega)$. The Fourier expansion is formally applicable only for functions decaying sufficiently fast at infinity (square integrable). In order to apply the Fourier transform to our case, the method of truncated functions [23] is used. It is performed by defining a new function $\mathbf{E}_s^{(T)}(t)$ that is equal to $\mathbf{E}_s(t)$ for $|t| \leqslant T$, but zero otherwise

$$\mathbf{E}_s^{(T)}(t) = \begin{cases} \mathbf{E}_s(t) & |t| \leqslant T, \\ 0 & |t| \geqslant T, \end{cases} \quad (15)$$

where t is the time at the remote detector (*time-at-observer*). The superscript T indicates parametric dependence on the width T of the truncation interval. Instead of the superscript, the dependence on T is sometimes shown in the arguments of the function.

The use of the truncation method is a substantial element of this approach. The truncated signals are square integrable with a well defined Fourier transform

$$\mathbf{E}_s^{(T)}(\omega) = \frac{1}{\sqrt{2\pi}}\int_{-T}^{T}\mathbf{E}_s(t)\exp(\mathrm{i}\omega t)\mathrm{d}t. \quad (16)$$

Consider, for example, a monochromatic dependence $\mathbf{E}_s(t) = \mathbf{E}_0\exp(-\mathrm{i}\omega_d t)$ with Doppler shifted frequency $\omega_d = \omega_i(1-\beta_i/(1-\beta_s))$ caused by Thomson scattering. The Fourier image of the truncated field

$$\mathbf{E}_s^{(T)}(\omega) = \mathbf{E}_0\sqrt{\frac{2}{\pi}}\frac{\sin[(\omega-\omega_d)T]}{\omega-\omega_d} \quad (17)$$

depends on ω and the truncation variable T. This is a smooth analytical function of ω at finite T and a singular δ-function at $T\to\infty$

$$\lim_{T\to\infty}\mathbf{E}_s^{(T)}(\omega) = \mathbf{E}_s(\omega) = \mathbf{E}_0\sqrt{2\pi}\,\delta(\omega-\omega_d). \quad (18)$$

Thus, the truncation method resolves the δ-function singularity in the Fourier transformed electric field of the radiation scattered by a single electron and characterized by a monochromatic wave with a Doppler shifted frequency. This allows for calculating quadratic field combinations without the uncertainty caused by the treatment of the square of a δ-function. We perform intermediate quadratic transformations at finite T with the limiting transition in the final expressions.

For the general case of arbitrary time dependence, the truncated field is expressed by the inverse Fourier integral

$$\mathbf{E}_s^{(T)}(t) = \frac{1}{\sqrt{2\pi}}\int_{-\infty}^{\infty}\mathbf{E}_s^{(T)}(\omega)\exp(-\mathrm{i}\omega t)\mathrm{d}\omega. \quad (19)$$

The time averaged quadratic combinations (A1) are expressed by double integrals over the frequencies ω_1 and ω_2. Consider, for example, the $S_0^{(s)}$ component

$$S_0^{(s)} = \lim_{T\to\infty}\frac{1}{2T}\int_{-T}^{T}(E_{sx}(t)E_{sx}^{\star}(t) + E_{st}(t)E_{st}^{\star}(t))\mathrm{d}t = \lim_{T\to\infty}\frac{1}{2\pi T}\times\int_{-\infty}^{+\infty}\mathrm{d}\omega_1\int_{-\infty}^{+\infty}\mathrm{d}\omega_2(E_{sx}^{(T)}(\omega_1)E_{sx}^{(T)\star}(\omega_2) + E_{st}^{(T)}(\omega_1)E_{st}^{(T)\star}(\omega_2))\frac{\sin[(\omega_2-\omega_1)T]}{\omega_2-\omega_1}. \quad (20)$$

At sufficiently large T the integral kernel is approximated by the δ-function

$$\frac{\sin[(\omega_2-\omega_1)T]}{\omega_2-\omega_1} \underset{T\to\infty}{\to} \pi\delta(\omega_2-\omega_1). \quad (21)$$

Performing integration over ω_1 or ω_2, the time averaged quadratic combinations take the form of an integral over the spectrum

$$S_0^{(s)} = \int_{-\infty}^{+\infty}\mathrm{d}\omega S_0(\omega), \quad S_0(\omega) = \lim_{T\to\infty}\frac{S_0^{(s)}(\omega,T)}{2T}, \quad S_0^{(s)}(\omega,T) = E_{sx}^{(T)}(\omega)E_{sx}^{(T)\star}(\omega) + E_{st}^{(T)}(\omega)E_{st}^{(T)\star}(\omega). \quad (22)$$

These transformations are equivalent to Parseval's theorem for spectral intensities.

Specifying the dependence on T in the quadratic combinations (22) the expression for $S_0^{(s)}(\omega)$ takes the form

$$S_0^{(s)}(\omega) = \lim_{T\to\infty}\frac{|\mathbf{E}_0|^2}{\pi T}\frac{\sin^2[(\omega-\omega_d)T]}{(\omega-\omega_d)^2}. \quad (23)$$

This function tends to zero at $\omega \neq \omega_d$ and to infinity at $\omega = \omega_d$, exhibiting properties of a delta-function of ω. Exact integration over ω yields

$$\int_{-\infty}^{+\infty}S_0(\omega)\mathrm{d}\omega = |\mathbf{E}_0|^2 \quad (24)$$

indicating that

$$S_0^{(s)}(\omega) = |\mathbf{E}_0|^2\delta(\omega-\omega_d). \quad (25)$$

Thus, the truncation method allows us to perform the limiting transition $T\to\infty$ without uncertainties caused by the treatment of the square of a δ-function (see appendix A.3).

The above example with a given amplitude $\mathbf{E}_0$ illustrates derivation of the spectral dependencies. The amplitude of the scattered signal is determined by the linear relationship between the Fourier image of the truncated scattered field and the amplitude $\mathbf{E}_i$ of the incident field. It is described by the matrix $\hat{\mathbf{\Pi}}$ and amplitude factor $f^{(T)}(\omega, \boldsymbol{\beta})$ derived in detail in [14] and briefly reviewed in appendix A.4

$$\mathbf{E}_s^{(T)}(\omega) = f^{(T)}(\omega, \boldsymbol{\beta})\hat{\mathbf{\Pi}} \cdot \mathbf{E}_i. \tag{26}$$

The spectral characteristics ω and T and spatial dependence on r are included in $f^{(T)}(\omega, \boldsymbol{\beta})$ defined by (A18) while the matrix $\hat{\mathbf{\Pi}}$ is given in its general vector form by (A17). The explicit form of $\hat{\mathbf{\Pi}}$ is obtained by substituting the electric field projections (10) in (A17)

$$\begin{pmatrix} E_{sx}^{(T)}(\omega) \\ E_{st}^{(T)}(\omega) \end{pmatrix} = f^{(T)}(\omega, \boldsymbol{\beta}) \begin{pmatrix} a & b \\ -b & c \end{pmatrix} \begin{pmatrix} E_{ix} \\ E_{it} \end{pmatrix},$$
$$c = \beta_i + \beta_s + \beta_i\beta_s - \cos\theta - \frac{(\beta_i + \beta_s)^2}{1 + \cos\theta},$$
$$a = -(1 - \beta_i)(1 - \beta_s) + \beta_x^2(1 - \cos\theta),$$
$$b = \beta_x(1 + \cos\theta - \beta_i - \beta_s)\tan\frac{\theta}{2}. \tag{27}$$

The matrix (27) consists of three elements a, b and c which are functions of the velocity components $\beta_i = \boldsymbol{\beta} \cdot \mathbf{i}$, $\beta_s = \boldsymbol{\beta} \cdot \mathbf{s}$, and $\beta_x = \boldsymbol{\beta} \cdot \mathbf{e}_x$ and the scattering angle θ where $\boldsymbol{\beta} = \mathbf{v}/c$.

3.2. Mueller matrix formalism

The matrix $\hat{\mathbf{\Pi}}$ allows us to present quadratic combinations of the scattered field components included in definition (A1) of the Stokes vector $\mathbf{S}^{(s)}$ in terms of the incident electric fields. As a first step, the products of the time-dependent scattered fields are expressed in terms of quadratic combinations of their Fourier images $E_{sx}^{(T)}(\omega)$ and $E_{st}^{(T)}(\omega)$. This is illustrated by equations (20)–(22) for the particular case of the zero-component $S_0^{(s)}$ but generalization to all other components is straightforward. The integration over t associated with the time averaging is converted to integration over ω. The integrand of this expression is defined as a spectral density of the auxiliary Stokes vector $\mathbf{S}^{(s)}(\omega, T)$. The $t \to \omega$ transformation and transition to the spectral density of the Stokes vector is an important element of the Thomson scattering polarization formalism [14]. It forms a unified basis for consideration of the frequency-integrated and frequency-resolved cases and shows the relationship between them.

The spectral density of the Stokes vector $\mathbf{S}^{(s)}(\omega)$ is defined by the limiting transition $T \to \infty$

$$\mathbf{S}^{(s)}(\omega) = \lim_{T\to\infty} \frac{\mathbf{S}^{(s)}(\omega, T)}{2T}. \tag{28}$$

The full frequency integrated Stokes vector $\mathbf{S}^{(s)}$ is obtained by integrating the spectral density $\mathbf{S}^{(s)}(\omega)$ over the spectrum of the scattered radiation

$$\mathbf{S}^{(s)} = \int_{-\infty}^{+\infty} \mathbf{S}^{(s)}(\omega)\mathrm{d}\omega. \tag{29}$$

We do not use additional indices to distinguish between frequency-integrated quantities such as $\mathbf{S}^{(s)}$ and frequency-dependent spectral density functions such as $\mathbf{S}^{(s)}(\omega)$, except for explicit indication of ω as an argument of all functions of the second type.

Using the matrix $\hat{\mathbf{\Pi}}$, the auxiliary vector $\mathbf{S}^{(s)}(\omega, T)$ can be expressed in terms of quadratic combinations of the incident electric fields. The rhs of the resulting expressions contains the square of the absolute value of $f^{(T)}(\omega, \boldsymbol{\beta})$, quadratic combinations of the factors a, b, and c, and different quadratic combinations of the $\mathbf{E}_i$ components. Expressing the products of the $\mathbf{E}_i$ components in terms of the components of $\mathbf{S}^{(i)}$ from (1) allows us to obtain the 4×4 auxiliary Mueller matrix $\hat{\mathbf{M}}^{(\mathrm{single})}(\omega, T)$ caused by scattering on a single electron moving with velocity $\boldsymbol{\beta}$. This matrix connects the auxiliary Stokes vector of the scattered radiation with the Stokes vector of the incident wave

$$\mathbf{S}^{(s)}(\omega, T) = \hat{\mathbf{M}}^{(\mathrm{single})}(\omega, T) \cdot \mathbf{S}^{(i)} \tag{30}$$

and can be conveniently expressed as a product $\hat{\mathbf{M}}^{(\mathrm{single})}(\omega, T) = C^{(T)}(\omega)\hat{\mathbf{W}}(\boldsymbol{\beta})$, where the scalar function $C^{(T)}(\omega)$ is proportional to the square of the absolute value of the function $f^{(T)}(\omega, \boldsymbol{\beta})$ (A18)

$$C^{(T)}(\omega) = \frac{r_0^2(1 - \beta^2)E_0^2}{2r^2(1 - \beta_s)^6}\left[\frac{2}{\pi}\frac{\sin^2(\omega - \omega_d)T}{(\omega - \omega_d)^2}\right]. \tag{31}$$

$$\hat{\mathbf{W}}(\boldsymbol{\beta}) = \begin{pmatrix} a^2 + 2b^2 + c^2 & a^2 - c^2 & 2b(a - c) & 0 \\ a^2 - c^2 & a^2 - 2b^2 + c^2 & 2b(a + c) & 0 \\ 2b(c - a) & -2b(a + c) & 2(ac - b^2) & 0 \\ 0 & 0 & 0 & 2(b^2 + ac) \end{pmatrix}. \tag{32}$$

The 4×4 matrix $\hat{\mathbf{W}}(\boldsymbol{\beta})$ is a function of quadratic combinations of the coefficients a, b and c

The amplitude E_0^2 is taken from expression (2) for $\mathbf{S}^{(i)}$ and included in (31). Correspondingly, the modified Stokes vector of the incident wave $\mathbf{S}^{(i)}$ is treated as a dimensionless normalized vector (2) without the E_0^2 factor ($\mathbf{S}^{(i)} \to \mathbf{S}^{(i)}/E_0^2$).

The renormalized vector $\mathbf{S}^{(i)}$ describes the dependence on the polarization characteristics of the incident light such as the orientation ψ and ellipticity χ angles. The factor $1/2$ in (31) originates from the similar factor in the rhs of (1).

Performing the limiting transition $T \to \infty$ in (30) yields the spectral density of the Stokes vector $\mathbf{S}^{(s)}(\omega)$ as a product of the spectral Mueller matrix $\hat{\mathbf{M}}^{(\mathrm{single})}(\omega)$ and $\mathbf{S}^{(i)}$

$$\mathbf{S}^{(s)}(\omega) = \hat{\mathbf{M}}^{(\mathrm{single})}(\omega) \cdot \mathbf{S}^{(i)}. \tag{33}$$

The limiting transition modifies the scalar function (31) but does not affect $\hat{\mathbf{W}}$ so that the spectral Mueller matrix takes a form

$$\hat{\mathbf{M}}^{(\mathrm{single})}(\omega) = C(\omega)\hat{\mathbf{W}}(\boldsymbol{\beta}),$$
$$C(\omega) = \frac{r_0^2(1-\beta^2)E_0^2}{2r^2(1-\beta_s)^6}\delta(\omega-\omega_d). \tag{34}$$

The form of the δ-function in (34) and the negative six power of the factor $1-\beta_s$ are rigorously determined by the limiting transition $T \to \infty$ without the uncertainty associated with the phenomenological 'recipe' for treatment of the square of a δ-function.

The full frequency integrated Stokes vector (29) is determined by integrating $\mathbf{S}^{(s)}(\omega)$ over the entire frequency spectrum. This yields $\mathbf{S}^{(s)}$ as a product of the frequency integrated Mueller matrix $\hat{\mathbf{M}}^{(\mathrm{single})}$ and $\mathbf{S}^{(i)}$

$$\mathbf{S}^{(s)} = \hat{\mathbf{M}}^{(\mathrm{single})} \cdot \mathbf{S}^{(i)}. \tag{35}$$

Explicit integration over ω in (34) removes the δ-function dependence in $C(\omega)$ and yields the frequency integrated Mueller matrix

$$\hat{\mathbf{M}}^{(\mathrm{single})} = C\hat{\mathbf{W}}(\boldsymbol{\beta}), \quad C = \frac{r_0^2(1-\beta^2)E_0^2}{2r^2(1-\beta_s)^6} \tag{36}$$

that describes the transformation of the Stokes vector caused by scattering on a single electron moving with velocity $\boldsymbol{\beta}$. All three Mueller matrices describe linear connections of the corresponding Stokes vectors of the scattered radiation with the incident Stokes vector $\mathbf{S}^{(i)}$. They are identical in structure with different amplitude factors $C^{(T)}(\omega)$, $C(\omega)$ or C while the fundamental matrix $\hat{\mathbf{W}}(\boldsymbol{\beta})$ is the same in all cases.

The velocity $\boldsymbol{\beta}$ as well as the polarization parameters ψ, χ are arbitrary in equations (35) and (36). The single electron Mueller matrix $\hat{\mathbf{M}}^{(\mathrm{single})}$ is tested in [14] by comparing with the solution to problem 6 in section 78 in [17]. It represents the angular distribution of the scattering power for a linearly polarized incident wave scattered by a charge moving with velocity $\boldsymbol{\beta}$ in the direction of the incident wave. In this particular case, the fully relativistic acceleration is perpendicular to the velocity yielding an expression for the scattering cross-section

$$\mathrm{d}\sigma = \left(\frac{e^2}{m_e c^2}\right)^2 \frac{(1-\beta^2)(1-\beta)^2}{(1-\beta\sin\Theta\cos\Phi)^6} \times [(1-\beta\sin\Theta\cos\Phi)^2 - (1-\beta^2)\cos^2\Theta]\mathrm{d}\Omega, \tag{37}$$

where $\mathrm{d}\sigma$ is the ratio of the power scattered into the solid angle $\mathrm{d}\Omega$ to the energy flux density of the incident radiation. The scattering direction $\mathbf{s}$ is characterized in [17] by the polar and azimuthal angles Θ, Φ relative to a spherical coordinate system with z-axis along $\mathbf{E}_i$ and x-axis along $\boldsymbol{\beta}$. Putting $\chi = 0$ for a linear polarized incident wave allows us to express the variables θ and ψ in terms of Θ, Φ (see (A2) and (A4))

$$\cos\theta = \sin\Theta\cos\Phi, \quad \cos^2\psi = \frac{\sin^2\Theta\sin^2\Phi}{1-\sin^2\Theta\cos^2\Phi} \tag{38}$$

and to obtain the total scattering power $S_0^{(s)}$ given by (35) and (36) in terms of the variables Θ and Φ. Calculating a, b, and c factors in $\hat{\mathbf{W}}$ by putting $\beta_i = \beta$, $\beta_s = \beta\cos\theta$, $\beta_x = 0$ yields $S_0^{(s)}$ and the corresponding cross-section which is identical to the solution (37) increasing confidence in the correctness of the Mueller matrix calculations.

All three variants of the Mueller matrix correspond to scattering on a single electron moving with velocity $\mathbf{v}$. Scattering from a single electron changes the frequency and polarization but the scattered wave continues to be monochromatic and fully polarized. Indeed, all three Mueller matrices conserve polarization and transfer fully polarized incident light to fully polarized scattered radiation for an arbitrary electron velocity. This property is proved by the remarkable identity [14]

$$S_0^{(s)2} - S_1^{(s)2} - S_2^{(s)2} - S_3^{(s)2} = (b^2+ac)^2C^2 \times (S_0^{(i)2} - S_1^{(i)2} - S_2^{(i)2} - S_3^{(i)2}) = 0 \tag{39}$$

which is a direct consequence of equations (11), (32), (35) and (36).

3.3. Comments on the 'square of a δ-function'

The zero-component of the spectral Stokes vector represents the power spectrum at the remote detector

$$P^{(\mathrm{single})}(\omega) = \frac{r_0^2(1-\beta^2)E_0^2}{2r^2(1-\beta_s)^6}(\hat{\mathbf{W}}(\boldsymbol{\beta})\cdot\mathbf{S}^{(i)})_0\delta(\omega-\omega_d). \tag{40}$$

The result (40) is consistent with the expression used for averaging over the electron distribution function in the first part of [15] dealing with the infinite scattering volume (infinite transit time, ITT) case. The key dependencies on ω and β_s, $P^{(\mathrm{single})}(\omega) \propto \delta(\omega-\omega_d)/(1-\beta_s)^6$, are identical to equation (7.2.19) in [2] and equation (4.35) in [16]. According to the terminology [2] $P^{(\mathrm{single})}(\omega)$ represents the *time-at-observer* power $P^{(\mathrm{observer})}$ given by (13).

The expression $P^{(\mathrm{single})}(\omega)$ used in the ITT part of [15] was declared in [18] to be in error due to improper handling of the square of a δ-function in the derivation of the spectral power. The arguments of [18] have been recently reviewed in a detailed tutorial article [16]. The argument in [18] has been repeated in many other TS publications including, at least, five more papers during the 1984–2011 period, and appears in section 3.5 in [1, p 53] as a comment about an error made in the original monograph [29]. In other publications (see, for example, [2]), the derivation [15] is accepted and used as a starting point for calculation without discussion of the issue claimed in [18]. As a result of these uncertainties, the controversy caused by the square of

a δ-function issue has created long-standing confusion in the literature.

A resolution of the problem is suggested in [14]. It was found that the square of a δ-function was properly treated in mathematical transformations in the first ITT part of [15]. The inconsistency between [18] and [15] originates not from a mathematical mistake in [15] but from the erroneous comparison of the *time-at-particle* power treated in [18] with the *time-at-observer* power analyzed in [2, 14, 15].

Indeed, the mean spectral power $P^{(\mathrm{single})}(\omega)$ is obtained by taking the total energy collected by the detector during the time interval of truncation and dividing it by the length of the interval T. Here, the interval T represents the time on the detector associated with the variable t. Contrary to this *time-at-observer* power, the mean power in [18] is defined by dividing the total emitted energy by the laser pulse length T. Thus, the same symbol T is used to define physically different *time-on-particle* interval associated with the variable t'. This is the time during which the electron is exposed to the incident laser light and re-emits the radiation in the scattering volume. As a result, the mean spectral intensity scattered by a single electron in [18] represents not the *time-at-observer* but the *time-at-particle* power. As expected they differ by the factor $(1-\beta_s)$ according to (13). The difference was explained in [18] as a mathematical mistake made in [15]. The corresponding mathematical transformations are not well specified in [18]. Following this general line we compare the results for two cases and suggest a possible resolution of the issue in appendix A.3. To the best of our knowledge this mathematical analysis of the 'square of a δ-function' problem has never been discussed in the TS literature.

4. Combined effect of many electrons

Equations (34) and (36) describe the elementary process of scattering on an individual electron moving in unbounded space filled with an incident homogeneous plane electromagnetic wave of infinite extent. They are used now to account for scattering from many electrons, illustrated by calculations for the zero-component of the Stokes vector.

Although the cross section for Thomson scattering is small (proportional to r_0^2) the intensity of the scattered radiation is measurable due to the large number of electrons $N \gg 1$ participating in scattering. The total electric field of the scattered radiation is a sum of the electric fields emitted by the individual electrons. The coherency matrix is constructed from time-averaged quadratic combinations of their components. The products of the field components are subdivided into two groups. There is a large number $\propto N(N-1)$ of cross-terms originating from the electrons characterized by different positions $\mathbf{R}_0^{(i)}$ and $\mathbf{R}_0^{(j)}$ with $i \neq j$ where the vectors $\mathbf{R}_0^{(i)}$ $(i = 1, 2, ...N)$ are introduced in (A15) and serve as labels of the unperturbed electron trajectories. Summing over many electrons, we assume the condition of incoherent Thomson scattering $\lambda_D k_i \sin\theta/2 \gg 1$, where the Debye length $\lambda_D = \sqrt{T_e/4\pi e^2 n_e}$ represents the mean spatial electron correlation length. As an example, the regime of incoherent scattering is relevant to the ITER plasma with a conventional TS diagnostic where laser wavelength $\lambda = 1.06\,\mu$m, $\theta \simeq 130^\circ$ and typical value of $\lambda_D \simeq 150\,\mu$m. Collective TS regimes with large wavelengths or small scattering angles are used for measurements of the bulk and fast ion characteristics (see, for example, [30] and detailed review [31]). Some interesting aspects of collective scattering related to momentum conservation are considered in [32]. This work is based on comparative analysis of wave-particle momentum redistribution in the process of Thomson scattering on electrons and ions. The role of scattering on ions is emphasized in the paper as an important mechanism needed for correct accounting for the momentum balance.

In the incoherent regime, the cross-terms are proportional to rapidly oscillating factors $\exp[-i\mathbf{q}\cdot(\mathbf{R}_0^{(i)} - \mathbf{R}_0^{(j)})]$ with $\mathbf{q} = \mathbf{k}_s - \mathbf{k}_i$ and, therefore, vanish after summation. Then, the products of the sum of the electric fields are reduced to the sum of the products characterized by equal indices $i = j$. Even in a case where radiation scattered at finite angles $\theta \simeq 90^\circ$ is strongly incoherent $(\lambda_D k_i \sin\theta/2 \gg 1)$, the radiation scattered at forward angles $\theta \to 0$ will be coherent, with all the electrons radiating coherently. This leads to the summation of the electric fields scattered by the individual electrons so that the resulting scattered field amplitude is proportional to $n_e e^2 E_0/m_e$ where n_e is the electron density and E_0 is the primary wave amplitude. Rigorous summation of the fields is performed in [33]. It takes into account different phases of the radiation coming from individual electrons. The sum of the scattered and primary electric field obtained from this microscopic approach is shown to be identical to the primary wave modified according to macroscopic theory based on the concepts of dielectric tensor and refractive index. Thus, the coherent solution localized at small θ represents an incident wave passing through a plasma. Within the scope of the microscopic model the effect of the plasma dispersion is self-consistently explained by the superposition of the far zone electric fields emitted by the individual electrons. The small deviation of the incident wave phase velocity from the speed of light can be ignored at high frequency of the incident radiation.

For scattering at larger angles θ, coherent solution drops quickly to zero when the scattering angles lie outside the narrow cone $\theta \leqslant \lambda/L$ where L is a linear dimension of the scattering volume. The rate of the coherent solution decay with θ is evaluated, for example, in exercise 4.9.7 in [34]. Outside the cone, the contribution from the coherent solution vanishes. In this zone, the incoherent solution for the scattered wave is dominant in the regime that is used for Thomson scattering diagnostic purposes.

In the incoherent solution, the Stokes vector of the scattered radiation is the sum of the Stokes vectors of the radiation scattered by the individual electrons. The summation of these $\boldsymbol{\beta}$-dependent quantities is equivalent to integration over $d\mathbf{r}'$ and $d\boldsymbol{\beta}$ in coordinate and velocity space. The equilibrium electron distribution function is defined as the

number of electrons $dN = n_e f_M(\boldsymbol{\beta})\, d\boldsymbol{\beta}\, d\mathbf{r}$ with velocities in the interval $\boldsymbol{\beta}, \boldsymbol{\beta} + d\boldsymbol{\beta}$ contained in a volume element $d\mathbf{r}$, where $f_M(\boldsymbol{\beta})$ is the relativistic Maxwellian distribution function normalized to unity

$$f_M(\boldsymbol{\beta}) = \frac{\mu \exp(-\mu/\sqrt{1-\beta^2})}{4\pi K_2(\mu)(1-\beta^2)^{5/2}}, \quad \mu = m_e c^2/T_e \tag{41}$$

and $K_2(\mu)$ is the modified Bessel function of the second kind [35]. We first select a group of electrons having equal velocities $\boldsymbol{\beta}$ in the velocity element $d\boldsymbol{\beta}$ but different initial positions $\mathbf{R}_0$ in coordinate space. The spectral powers (40) registered by the detector from each of these electrons are the same (do not depend on $\mathbf{R}_0$). The intuitive way of accounting for the effect of many electrons is to multiply the power from a single electron $P^{(\mathrm{single})}(\omega)$ by the total number of electrons $n_e V f_M d\boldsymbol{\beta}$ in the scattering volume V. The resulting total spectral power

$$P_{\mathrm{ITT}}(\omega) = \frac{r_0^2 n_e V (1-\beta^2) E_0^2 f_M\, d\boldsymbol{\beta}}{2r^2(1-\beta_s)^6} \times (\hat{\mathbf{W}}(\boldsymbol{\beta}) \cdot \mathbf{S}^{(i)})_0 \delta(\omega - \omega_d) \tag{42}$$

is equivalent to equation (10) derived in section II.C of [15] devoted to the infinite scattering volume or ITT case.

This intuitive approach can fail to accurately characterize the scattered power. As was pointed out by Stupakov [28], a more consistent approach is not a summation of the instantaneous powers but a summation of energies emitted by the electrons and accumulated by the detector during time interval long compared to the particle transit time through the scattering volume. The problem was formally treated in section II.D of [15] devoted to the finite scattering volume or, equivalently, to the FTT case, by applying the Fourier transform in coordinate space leading to the result

$$P_{\mathrm{FTT}}(\omega) = \frac{r_0^2 n_e V (1-\beta^2) E_0^2 f_M\, d\boldsymbol{\beta}}{2r^2(1-\beta_s)^5} \times (\hat{\mathbf{W}}(\boldsymbol{\beta}) \cdot \mathbf{S}^{(i)})_0 \delta(\omega - \omega_d). \tag{43}$$

The only difference between the ITT power spectrum (42) and the FTT case (43) is an additional factor $(1-\beta_s)$ in the numerator of the FTT intensity spectrum. The FTT weighting factor is generally accepted in all present-day relativistic treatments of TS radiation. A qualitative physical explanation of the FTT effect similar to the picture shown in figure 4 is suggested in section III of [15] based on a single-bounded particle model. The distortion of the signal caused by the finite size of the scattering volume has a twofold effect. First, since an electron spends a finite time L/v_{Te} within the scattering volume it broadens the spectrum (40) to the finite width $\delta\omega/\omega \simeq 2\pi v_{Te}/(\omega L)$. The transit time broadening is much less than the Doppler thermal broadening $\Delta\omega/\omega \simeq v_{Te}/c$ at $\lambda \ll L$ and, therefore, can be ignored in the case of practical interest with $\lambda \ll L$ [1, 15, 16]. The second effect is less obvious and impacts the amplitude of the spectrum rather than its shape such that there appears an additional factor $(1-\beta_s)$ in the numerator of the FTT intensity spectrum (43) compared to the ITT power spectrum (42). This result is consistent with equation (14).

An alternative geometrical interpretation of the FTT effect was suggested in [14]. The area of $d\mathbf{r}'$-integration corresponds to the summation over those electrons whose pulses of scattered radiation pass through the detector at a given time t (the time-averaging variable in (A1)) on the detector. Consider the electrons passing through the narrow stream tube of length L and cross-section dS shown in figure 4. Visualization of the positions and distances between the successive electromagnetic pulses emitted by the individual electrons and counting the number of pulses passing through the remote detector at a given moment of time t on the detector shows that it corresponds not to the number of electrons $n_e L dS$ inside the stream tube, but to the modified number $(1-\beta_s) n_e L dS$. This justifies the use of the fifth power weighting factor for averaging of the Stokes vector components.

To sum up, if the radiating particles are in a bounded volume the radiation intensity at the remote detector is determined not by the single particle *time-at-observer* power $P^{(\mathrm{observer})} = P^{(\mathrm{single})}$ but by the *time-at-particle* power $P^{(\mathrm{particle})} = (1-\beta_s) P^{(\mathrm{single})}$ multiplied by the number of emitters inside the scattering volume. For synchrotron radiation, this conclusion was, for the first time, obtained and extended from the intensity to all the components of the Stokes vector in [36]. A similar, but more succinct analysis of synchrotron radiation was presented, approximately at the same time, in [37]. The analogy with synchrotron radiation was used in [2] to explain the need for the additional factor $(1-\beta_s)$ to account for the combined effect of many electrons.

5. Frequency-integrated Mueller matrix

The procedure of integration over the spectrum corresponds to a transition from spectrum-based characterization of Thomson scattering to polarization analysis based on the total frequency-integrated Stokes vector spectral intensities. Integrating over all frequencies results in an increased number of detected photons with better statistics and accuracy of measurement. This is a key element of the polarization-based TS diagnostic compared to the traditional spectrum-based TS method. Since the purpose of these studies is to investigate the optimal capabilities of depolarization diagnostics, we will, first, focus on the characteristics of the frequency-integrated radiation and then consider the frequency-resolved case.

5.1. Averaging over β with the FTT weighting factor

Averaging over velocity space is equivalent to integration of the Mueller matrix (36) over the relativistic Maxwellian distribution function (41). The combined effect of many electrons and finite size of the scattering volume are taken into account by adding the total number of electrons in the scattering volume $N = n_e V$ and the factor $(1-\beta_s)$ to the scattering operator. Both these factors are missing in [9]. The final

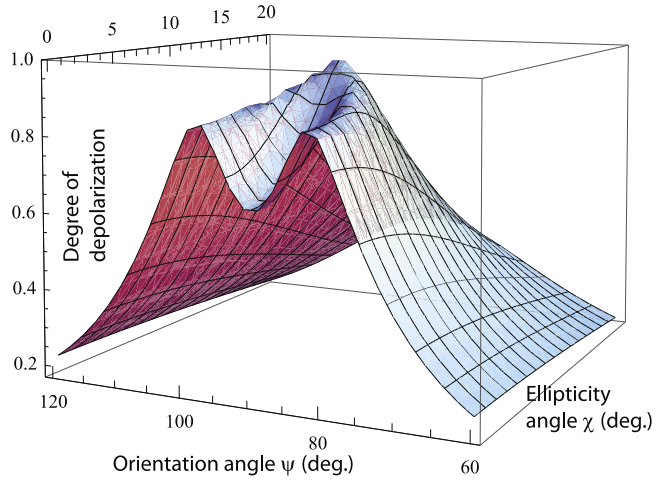

Figure 5. Degree of depolarization versus orientation and ellipticity angles ψ and χ at $\theta = 90°$, $T_e = 10$ keV. There is a local maximum of D at $\psi \simeq 82°$ and $\chi = 0$ (linear polarization), but the absolute maximum is reached at $\psi = 90°$ and $\chi \simeq 9°$ (elliptical polarization) (D is an even function of $\cos\psi$). Reproduced from [12], with the permission of AIP Publishing.

expression has the form

$$\hat{\mathbf{M}}(\mu, \theta) = \frac{r_0^2 N E_0^2}{2r^2} \int \frac{(1 - \beta^2) f_M(\boldsymbol{\beta}) \mathrm{d}\boldsymbol{\beta}}{(1 - \beta_s)^5} \hat{\mathbf{W}}(\boldsymbol{\beta}). \quad (44)$$

For compact notation, we present the results of integration for the normalized dimensionless matrix $\hat{\mathbf{m}}(\mu, \theta)$

$$\hat{\mathbf{m}}(\mu, \theta) = \hat{\mathbf{M}}(\mu, \theta)/C_0, \quad (45)$$

where the dimensionless factor $C_0 = r_0^2 E_0^2 N/2r^2$.

The integration (44) is performed in spherical coordinates with the v_z and v_x axes directed along $\mathbf{s}$ and $\mathbf{e}_x$, respectively, such that $\boldsymbol{\beta} = (\beta \sin\alpha \cos\phi,\ \beta \sin\alpha \sin\phi,\ \beta \cos\alpha)$, where α is the polar angle and ϕ is the azimuthal angle measured from $\mathbf{e}_x$ in the orthogonal plane. The factors a, b and c in $\hat{\mathbf{W}}(\boldsymbol{\beta})$ depend on three components of the electron velocity: $\beta_i = \boldsymbol{\beta} \cdot \mathbf{i}$, $\beta_s = \boldsymbol{\beta} \cdot \mathbf{s}$ and $\beta_x = \boldsymbol{\beta} \cdot \mathbf{e}_x$, where $\boldsymbol{\beta} = \mathbf{v}/c$. They are expressed as functions of the polar angle α and azimuthal angle ϕ. Averaging over the relativistic Maxwellian distribution function (44) consists of three successive integrations

$$\hat{\mathbf{m}}(\mu, \theta) = \frac{\mu}{4\pi K_2(\mu)} \int_0^1 \frac{\beta^2 \exp(-\mu/\sqrt{1 - \beta^2})\mathrm{d}\beta}{(1 - \beta^2)^{3/2}} \times \int_0^\pi \frac{\sin\alpha \mathrm{d}\alpha}{(1 - \beta\cos\alpha)^5} \int_0^{2\pi} \mathrm{d}\phi \hat{\mathbf{W}}(\beta, \alpha, \phi). \quad (46)$$

Four elements of the matrix $\hat{\mathbf{W}}$ are proportional to $b \propto \beta_x$. Indeed, from (27) it follows that factor c does not depend on β_x while factor a is even and factor b is odd in β_x. Since the Maxwellian distribution function as well as all other weighting factors are even functions of β_x, these four elements average to zero after integration over the velocity space. The remaining five elements are integrated in analytical form according to (46) yielding functions of the scattering angle, $u = \cos\theta$, and electron temperature via the factor μ^2 and function $G(\mu) = K_1(\mu)/(\mu K_2(\mu))$, where K_1 and K_2 are modified Bessel functions of the second kind (see [35])

$$\begin{aligned} m_{00} &= 1 + u^2 - 2G(\mu)(u^2 + 4u - 3) + (16/\mu^2)(1 - u)^2, \\ m_{01} &= m_{10} = 1 - u^2, \\ m_{11} &= 1 + u^2 + 2G(\mu)(u^2 - 4u + 1) + (12/\mu^2)(1 - u)^2, \\ m_{22} &= 2u - 4G(\mu)(u^2 - u + 1) - (12/\mu^2)(1 - u)^2, \\ m_{33} &= 2u - 4G(\mu)u(2u - 1) - (8/\mu^2)(1 - u)^2. \end{aligned} \quad (47)$$

The details of this calculation are described in [14].

The matrix elements (47) present an exact analytical solution for the state of polarization of incoherent Thomson scattering radiation. In contrast to [9] where only the lowest order linear in T_e analytical results were obtained, expressions (47) are valid for the full range of scattering angles and electron thermal motion from non-relativistic to ultra-relativistic. The first terms in (47) describe the change of polarization in cold plasma ($\mu \to \infty$), the second terms yield first order corrections in the weakly relativistic limit at $\mu \gg 1$, and the third terms dominate at ultra-relativistic temperatures $\mu \ll 1$.

The Mueller matrix $\hat{\mathbf{m}}(\mu, \theta)$ does not conserve polarization and transfers fully polarized incident light to partially polarized scattered radiation. This property is intrinsically connected with the broadening of the scattered spectrum, which by definition is no longer fully polarized. The degree of depolarization D is defined by equation (3) as a ratio of power flux in the unpolarized component to the total power flux. Since D is a ratio of two fluxes, the normalization factor C_0 cancels in the final expression for D. Thus, the degree of polarization/depolarization is completely determined by the elements of the matrix $\hat{\mathbf{m}}(\mu, \theta)$ and the components $\mathbf{S}^{(i)}(\psi, \chi)$. Detailed information about the properties of this function of four variables is presented in [12] and reviewed in section 5.2.

5.2. Degree of depolarization for frequency integrated Mueller matrix

The degree of depolarization (3) depends on T_e, scattering angle θ, and polarization characteristics of the incident light ψ and χ. In spite of the large number of variables and complexity of the dependencies, the exact analytical results allow us to describe in a compact form the general properties of the degree of polarization [12]. One particular example illustrating a maxima of D as a function of ψ and χ is shown in figure 5 for $T_e = 10$ keV and $\theta = 90°$. There is a peak of D at $\psi \simeq 82°$ for linear incident polarization but the absolute maximum is reached at $\psi = 90°$ for elliptically polarized light. This extreme regime with the absolute maximum of D close to unity corresponds to small scattered power S_0 and results in large error bars for polarization-based T_e measurements. The smallness of S_0 is caused by the incident wave electric field vector being almost parallel to the scattering plane at $\psi = 90°$. This electric field direction is in turn almost parallel to the propagation direction $\theta = 90°$ of the scattered wave. Since the scattered wave must be transverse, the

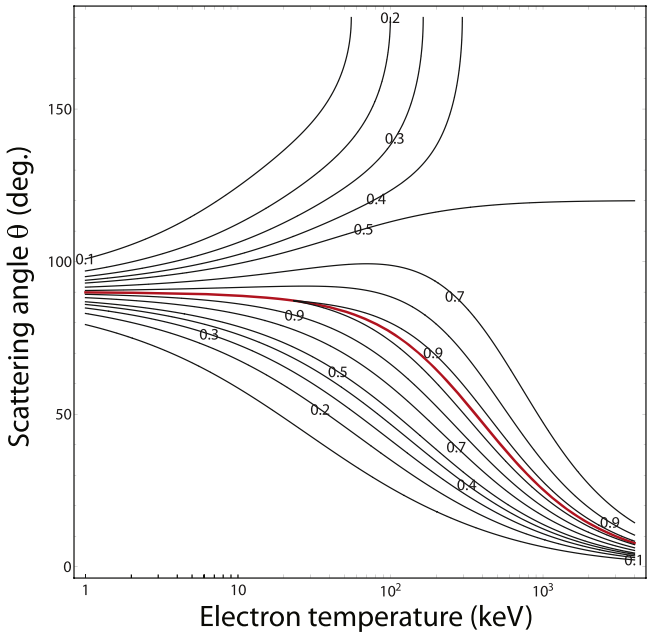

Figure 6. Contour lines of the maximum value of the degree of depolarization $D_{\max}(T_e, \theta)$ (maximized with respect to all possible polarization states of the incident light). The red curve is a boundary in (T_e, θ) space that determines which of the two maxima shown in figure 5 provides the absolute maximum. Reproduced from [12], with the permission of AIP Publishing.

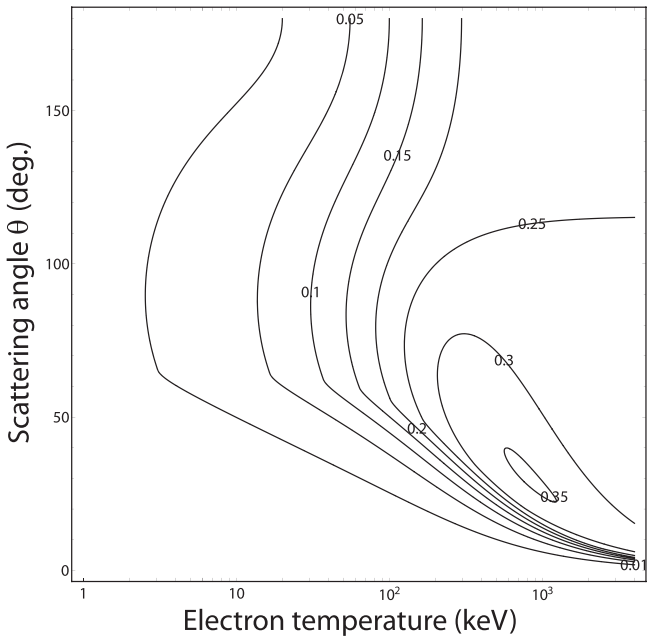

Figure 7. Contour lines of the minimum value of the degree of depolarization $D_{\min}(T_e, \theta)$ (minimized with respect to all possible polarization states of the incident laser light). Reproduced from [12], with the permission of AIP Publishing.

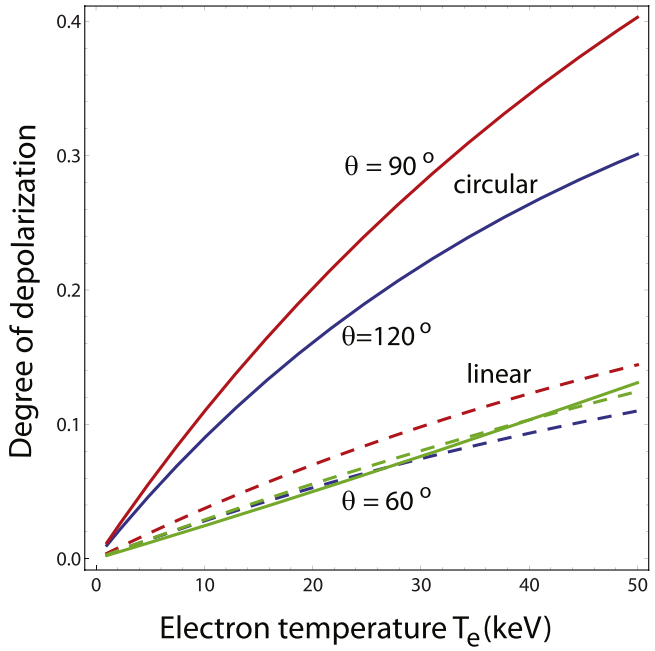

Figure 8. Degree of depolarization versus T_e for three scattering angles: 60° (green), 90° (red) and 120° (blue) (solid lines: circular polarization at $\chi = 45°$; dashed lines: linear polarization at $\psi = \chi = 0$). Reproduced from [12], with the permission of AIP Publishing.

efficiency of the scattering and intensity of the re-emitted radiation are small. Correspondingly, the weakness of the signals in this regime leads to their poor measurability.

At $T_e \to 0$, the peak of $D(\psi, \chi)$ profile is strongly localized in the vicinity of $\psi = 90°$ and $\chi = 0$. The absolute maximum of $D(\psi, \chi)$ tends to unity forming almost singular profile quickly decaying outward. Away from this irregularity the degree of depolarization is of order $T_e/m_e c^2$, which is consistent with the similar result (C17) for the frequency-resolved degree of depolarization. In some cases, a combination of the numerical factors amplifies the degree of depolarization up to 25%–30%.

At any given θ and T_e, extrema of D as a function of ψ and χ are reached at the boundaries of the rectangular area $0 \leqslant \psi \leqslant \pi/2$, $0 \leqslant \chi \leqslant \pi/4$. This allows us to finding the absolute maximum $D_{\max}(T_e, \theta)$, and minimum $D_{\min}(T_e, \theta)$, with respect to all possible polarization states of the incident radiation, and to set upper and lower limits on D at given θ and T_e. Quantitative picture of the dependencies of these two functions on T_e and θ is shown in figures 6 and 7, respectively. The red curve in figure 6 illustrates a boundary in (T_e, θ) space that determines which of the two maxima shown in figure 5 provides the absolute maximum. The area above the curve corresponds to the absolute maximum realized at elliptic incident polarization with $\psi = 90°$. The absolute maximum of D for forward scattering ($\theta < 90°$) takes place at linear incident polarization with $0 \leqslant \psi \leqslant 90°$. A good test of correctness of the matrix elements $\hat{\mathbf{m}}$ is that for all values of the variables $0 \leqslant D < 1$.

The ITER LIDAR TS system was planned to detect backscattered radiation at $\theta \sim 180°$ [38, 39]. For such backscattered light, the degree of depolarization is quadratic in $T_e/m_e c^2 \ll 1$ and, therefore, small (~3%–5%) at the temperatures expected in ITER. The effect is about five times smaller than for perpendicular scattering and is, therefore, difficult to exploit for T_e determination in LIDAR. Under LIDAR conditions the degree of depolarization is almost

insensitive to the orientation angle ψ and reaches its maximum for a circularly polarized incident laser beam.

For a conventional TS system with $\theta \simeq 90^\circ$, the situation is much more favorable with average $D \sim 20\%$–25%. The cases of practical interest of circular and linear incident polarizations are illustrated in figure 8 at three scattering angles. Although circular incident polarization yields stronger depolarization of scattered radiation, rigorous minimization of the error bars shows that linear incident polarization is preferential for polarization-based diagnostics [12].

5.3. Mueller matrix averaged over β with the ITT weighting factor

The technique of analytical integration over $\boldsymbol{\beta}$ can also be applied to the ITT weighting factor $\propto (1 - \beta^2)/(1 - \beta_s)^6$ that was used in [9]. This also yields Mueller matrix elements valid at all temperatures. Although the sixth power scaling is irrelevant for TS applications, it is useful for the purpose of comparison to illustrate the importance of the specific form of the weighting factor. The corresponding Mueller matrices $\hat{\mathbf{H}}$ and $\hat{\mathbf{h}}$ are introduced as

$$\hat{\mathbf{H}}(\mu, \theta) = C_0 \hat{\mathbf{h}}(\mu, \theta), \tag{48}$$

where $\hat{\mathbf{H}}$ is defined by the integral (44) with the factor $(1 - \beta_s)^6$ in the denominator. The result of exact calculation of the matrix $\hat{\mathbf{h}}$ is presented by equation (B1) in appendix B. Comparison of the two Mueller matrices $\hat{\mathbf{m}}$ and $\hat{\mathbf{h}}$ shows that they differ in essentials. For example, the off-diagonal elements $m_{01} = m_{10}$ do not depend on electron temperature while the same elements of the matrix $\hat{\mathbf{h}}$ are substantial functions of T_e. The temperature independence of the off-diagonal elements $m_{01} = m_{10}$ is a unique consequence of the fifth power weighting factor. The same integration performed for any other weighting factor would result in temperature-dependent off-diagonal elements.

A good test of the exact analytical calculations is comparison with the first-order expansions in T_e presented by equation (44) in [9]. Ignoring small terms proportional to μ^{-2} and μ^{-4} and taking into account that $G(\mu) \to 1/\mu = T_e/m_e c^2$ yields the first order correction in T_e to the cold plasma Mueller matrix. Comparing this correction with expressions (44) in [9] at $\overline{\beta^2} = 3T_e/m_e c^2$ shows that they are identical. This verifies the first-order expansions in T_e obtained in [9] for the ITT model, and increases confidence in the correctness of the exact analytical calculations.

6. Frequency-resolved Mueller matrix

Realistic experimental constraints require detecting scattered photons within a limited wavelength range. This necessitates understanding the frequency-resolved degree of polarization first discussed in [9]. From the theory side, significant differences arise because the time averaging included in the definition of the polarization matrix and the Stokes vectors assumes existence of a broad frequency spectrum. From the experimental side, the finite wavelength response band of optical instrumentation reduces the accuracy of polarization-based measurements if the TS spectrum is wide. Rigorous analysis of polarization characteristics in a finite spectral band does not seem to be present in polarization literature (see, for example, [40–42]). As suggested in [14], some quantitative steps in this direction can be made on the basis of equation (29).

Consider a partial contribution $\Delta\mathbf{S}^{(s)}$ to the spectrum integrated Stokes vector (29) from a narrow frequency interval $\Delta\omega$, such that $\Delta\mathbf{S}^{(s)} = \mathbf{S}^{(s)}(\omega)\Delta\omega$. Formal substitution of $\Delta\mathbf{S}^{(s)}$ to the equation for the degree of polarization (3) yields $P(\omega)$ which is determined by the spectral density $\mathbf{S}^{(s)}(\omega)$ and does not depended on $\Delta\omega$

$$P(\omega) = \frac{\sqrt{S_1^{(s)2}(\omega) + S_2^{(s)2}(\omega) + S_3^{(s)2}(\omega)}}{S_0^{(s)}(\omega)}. \tag{49}$$

The Stokes vector components $\mathbf{S}^{(s)}(\omega)$ are determined by the single electron spectral Mueller matrix (34) averaged over the relativistic Maxwellian distribution function with the weighting factor (44) and δ-function spectral dependence

$$\hat{\mathbf{M}}(\omega, \mu, \theta) = \frac{r_0^2 n_e V E_0^2}{2r^2} \int \frac{(1 - \beta^2) f_M(\boldsymbol{\beta}) \mathrm{d}\boldsymbol{\beta}}{(1 - \beta_s)^5} \times \hat{\mathbf{W}}(\boldsymbol{\beta}) \delta(\omega - \omega_d). \tag{50}$$

To evaluate the feasibility of frequency-resolved TS polarimetry, an expression similar to (50) but with incorrect sixth power weighting factor was suggested in [9]. Two angular variables $\cos\theta_s$ and $\cos\theta_i$ and $\beta = |\boldsymbol{\beta}|$ were used for integration where θ_s and θ_i are the angles between $\boldsymbol{\beta}$ and the propagation directions $\mathbf{s}$ and $\mathbf{i}$. The result in its final form is presented by the integral over two variables. This allows the authors to obtain the lowest order linear in T_e analytical expressions at $\omega = \omega_i$. Using numerical methods yields more information about dependencies of the resolved degree of polarization $P(\omega)$ on ω at some specific values of T_e and ψ shown in [9].

The original idea [9] and the method of integration suggested in this paper were further developed computationally with the use of the correct fifth power weighting factor. Numerical codes for the frequency-resolved polarization and analysis of the experimental technique were recently developed by Giudicotti *et al* [21]. They benchmarked their numerical results by computing the frequency-resolved Mueller matrix elements, integrating them over the spectrum and comparing with the frequency integrated analytical results (47). Thus, the exact relativistic expressions (47) were used for benchmarking and verification of numerical codes for frequency-resolved TS polarization. The results of this code verification show good agreement with the analytical expressions.

The spectral Stokes vector components, $\mathbf{S}^{(s)}(\omega) = \hat{\mathbf{M}}(\omega, \mu, \theta) \cdot \mathbf{S}^{(i)}(\psi, \chi)$, are functions of five variables. In view of the difficulties caused by the multidimensional parameter space of the problem it is highly desirable to have analytical expressions for $\hat{\mathbf{M}}(\omega, \mu, \theta)$. We show in this section that the frequency-resolved Muller matrix elements can be calculated analytically and expressed as a combination

of four simple 1D integrals which are the only functions that require numerical integration at the final stage of calculation. To the best of our knowledge the exact analytical solution for the frequency-resolved Mueller matrix has not been obtained yet. We describe the main steps of the derivation and the final results while the technical details are given in appendix C and supplementary material.

6.1. Exact relativistic expressions for $\widehat{m}(\omega)$

Contrary to the previous section devoted to the frequency-integrated Mueller matrix, the integration over $\boldsymbol{\beta}$ is performed in (50) in a different coordinate system $(\mathbf{e}_x, \mathbf{e}_y, \mathbf{e}_z)$ with the z-axis directed along $\mathbf{k}_s - \mathbf{k}_i$ such that $\mathbf{e}_z = (\mathbf{k}_s - \mathbf{k}_i)/|\mathbf{k}_s - \mathbf{k}_i| = (\mathbf{s}(X+1) - \mathbf{i})/k$, $\mathbf{e}_y = \mathbf{e}_z \times \mathbf{e}_x$ where $\mathbf{e}_x = [\mathbf{i} \times \mathbf{s}]/\sin\theta$ is the unit vector normal to the scattering plane. The dimensionless wave vector k and frequency shift X relative to the incident wave frequency are defined as

$$k = \frac{c|\mathbf{k}_s - \mathbf{k}_i|}{\omega_i} = \sqrt{X^2 + 2(X+1)(1-u)}, \quad X = \frac{\omega}{\omega_i} - 1. \tag{51}$$

In this coordinate system, the argument of the δ-function in (50) takes a form which allows for immediate integration over β_z: $\delta(\omega - \omega_i(1-\beta_i)/(1-\beta_s)) = (1-\beta_s)\delta[\omega - \omega_i - \boldsymbol{\beta}\cdot(\mathbf{k}_s - \mathbf{k}_i)c] = (1-\beta_s)\delta(\beta_\omega - \beta_z)/(\omega_i k)$, where $\beta_\omega = X/k$. Performing β_z-integration yields a double integral of a function of two variables β_x and β_y over a circular area $\beta_x^2 + \beta_y^2 \leqslant 1 - \beta_\omega^2$ while the β_z component is fixed in the integrand, $\beta_z = \beta_\omega$. Four elements of the matrix $\hat{\mathbf{W}}$ are proportional to $b \propto \beta_x$. They average to zero after integration over β_x using the same arguments as in section 5.1. The remaining five elements are integrated in the polar coordinate system $(\beta_\perp, \phi)$ such that $\beta_x = \beta_\perp\cos\phi$ and $\beta_y = \beta_\perp\sin\phi$ where $0 \leqslant \beta_\perp^2 \leqslant 1 - \beta_\omega^2$ and $0 \leqslant \phi \leqslant 2\pi$. We briefly comment here on the integration over ϕ and $\beta_\perp$ for the dimensionless matrix $\hat{\mathbf{m}}(\omega, \mu, \theta)$ which is the same as the original matrix (50) after integration over β_z and normalization similar to (45) but with the different normalization constant C_0/ω_i. The details of the derivation are given in appendix C.

The result of integration over ϕ is defined by the matrix $\hat{\mathbf{m}}^{(\phi)}(\omega, \beta_\perp)$

$$\hat{\mathbf{m}}^{(\phi)}(\omega, \beta_\perp) = \int_0^{2\pi} \frac{\hat{\mathbf{W}}(\beta_\perp, \phi)\mathrm{d}\phi}{(1-\beta_s)^4}. \tag{52}$$

Explicit dependencies on ϕ are presented in (52) by four different combinations which are integrated exactly in analytical form. Indeed, the ϕ-dependencies enter Mueller matrix $\hat{\mathbf{W}}(\beta_\perp, \phi)$ through the factors β_i, β_s and β_x in a, b and c functions given by (27). Expressing β_i and β_x^2 in terms of the whole combination $(1-\beta_s)$ and substituting in $\hat{\mathbf{W}}(\beta_\perp, \phi)$ gives fourth order polynomial functions of $(1-\beta_s)$. Dividing by the factor $(1-\beta_s)^4$ in the denominator of (52) leads to fourth order polynomials of the inverse ratio $1/(1-\beta_s)$ with the coefficients depending on X, u and $\beta_\perp$. Thus, all dependencies on ϕ in (52) are reduced to four certain combinations of the form $\propto(1-\beta_s)^{-n}$ where $n = 1, \ldots 4$. In the coordinate system $(\mathbf{e}_x, \mathbf{e}_y, \mathbf{e}_z)$, the expression for $(1-\beta_s)$ takes the form, $1 - \beta_s = \beta_\perp s_y(H - \sin\phi)$, where $H = (1 - \beta_\omega s_z)/\beta_\perp s_y$ while $s_z = (\mathbf{s}\cdot\mathbf{e}_z) = (X + 1 - u)/k$ and $s_y = (\mathbf{s}\cdot\mathbf{e}_y) = \sqrt{1-u^2}/k$. Integrating the fourth order polynomial function of $1/(1-\beta_s)$ over ϕ leads to the integrals of the form

$$\int_0^{2\pi} \frac{\mathrm{d}\phi}{[H - \sin\phi]^n} = \frac{G_{n-1}}{(H^2-1)^{(2n-1)/2}}, \quad n = 1, \ldots 4, \tag{53}$$

where G_{n-1} are $n-1$ order polynomials of H.

The next step of calculation is the integration over the 'radial' variable $\beta_\perp$ according to

$$\hat{\mathbf{m}}(\omega, \mu, u) = \frac{1}{k}\int_0^{\sqrt{1-\beta_\omega^2}} \beta_\perp \mathrm{d}\beta_\perp (1 - \beta_\omega^2 - \beta_\perp^2) \times f_M(\beta_\perp)\hat{\mathbf{m}}^{(\phi)}(\omega, \beta_\perp). \tag{54}$$

It is useful to introduce a new variable of integration t such that $\beta_\perp^2 = (1-\beta_\omega^2)(1 - 1/t^2)$ where $1 \leqslant t \leqslant \infty$. This variable represents the relativistic factor $\gamma = (1-\beta^2)^{-1/2}$ normalized to $1/\sqrt{1-\beta_\omega^2}$. After corresponding transformations the argument of the fractional exponents in equation (53) takes a form $(H^2-1)^{(2n-1)/2} \propto (r^2 + t^2)^{(2n-1)/2}$, where $r^2 = 2(X+1)(1+u)/k^2$. Then, the final result of integration over t yields five non-zero elements of the frequency-resolved Mueller matrix. They are presented in a compact form of a superposition of four well converged integrals with 25 coefficients, 13 of which are different rational functions of X and u given by equation (C12) in appendix C

$$\hat{\mathbf{m}}_{ij}(X, \mu, u) = \sum_{n=0}^{n=4} C_{ij}^{(n)}(X, u)E^{(n)}(p, r). \tag{55}$$

The coefficients $C_{ij}^{(n)}$ were calculated in analytic form both manually following the steps described in appendix C (see also the supplementary material) and with the use of analytic capabilities of Mathematica software [43]. At $n = 1, \ldots 4$, the integrals $E^{(n)}(p, r)$ are defined as follows

$$E^{(n)}(p, r) = \int_1^\infty \frac{\mathrm{d}t\exp(-pt)}{(r^2 + t^2)^{(2n+1)/2}}, \quad p = \mu\sqrt{\frac{X^2}{2(X+1)(1-u)} + 1}, \quad r^2 = \frac{2(X+1)(1+u)}{k^2} \tag{56}$$

while at $n = 0$ the corresponding function $E^{(0)}(p, r)$ is a function of only the first argument p, $E^{(0)}(p) = \exp(-p)$. For backscattered radiation with $u = -1$ the argument $r = 0$. In this particular case, the integrals $E^{(n)}(p, r)$ coincide at $n = 1, \ldots 4$ with the exponential integral functions $E^{(n)}(p, 0) = E_{2n+1}(p)$ described in the literature (see [35]).

At low temperatures, the factor $\mu = m_e c^2/T_e$ and the corresponding value of the variable p are large. In this case, the main contribution to $E^{(n)}(p, r)$ comes from the narrow interval $t - 1 \leqslant 1/p$ in the vicinity of the low limit of integration. This provides smallness ($\propto 1/p$) of the integral terms with $n = 1, \ldots 4$ compared to the first non-integral terms $\hat{\mathbf{m}}_{ij}^{(0)} = C_{ij}^{(0)}E^{(0)}(p)$ related to $n = 0$. The dominant at $\mu \gg 1$

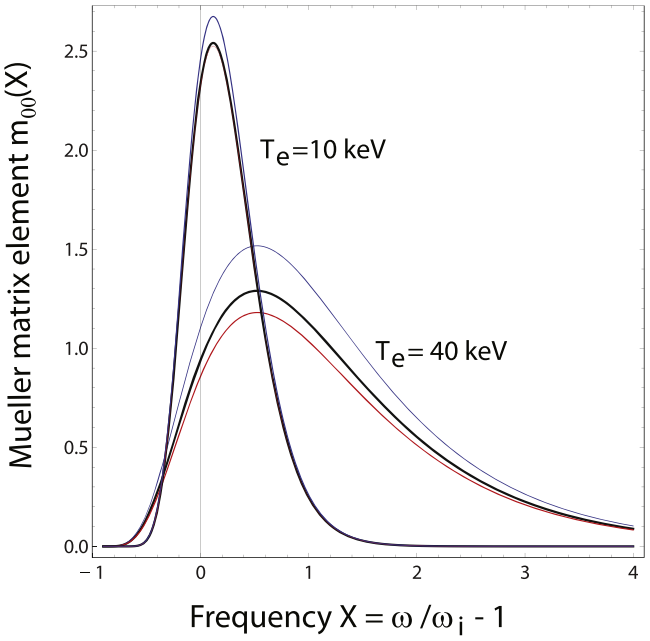

Figure 9. Frequency resolved Mueller matrix element m_{00} given by (55) versus frequency $X = \omega/\omega_i - 1$ at $T_e = 10$ keV (narrow black curve) and $T_e = 40$ keV (broad black curve) while $\theta = 150°$. The thin blue lines illustrate the contribution to m_{00} from the first $n = 0$ term $m_{00}^{(0)}$ dominant at low temperature. The approximation $\hat{\mathbf{m}}_{ij}^{(1)}(X)$ given by (59) with the T_e/m_ec^2 linear correction is shown by a thin red line.

first part $\hat{\mathbf{m}}_{ij}^{(0)}$ is proportional to the ratio $E^{(0)}(p)/K_2(\mu)$. The limiting value of this μ-dependent ratio tends at $\mu \to \infty$ to the δ-function of X

$$\lim_{\mu\to\infty} \frac{\exp(-\mu/\sqrt{1-\beta_\omega^2})}{K_2(\mu)} = 2\sqrt{2(1-u)}\,\delta(X). \quad (57)$$

Taking into account the δ-function properties by putting $X = 0$ in $C_{ij}^{(0)}$ and ignoring small (proportional to T_e/m_ec^2) integral terms with $n = 1,...4$ yields the asymptotic expression for the frequency-resolved Mueller matrix in cold plasma

$$\lim_{T_e\to 0} \hat{\mathbf{m}}_{ij}(X, u) = \begin{pmatrix} 1+u^2 & 1-u^2 & 0 & 0 \\ 1-u^2 & 1+u^2 & 0 & 0 \\ 0 & 0 & 2u & 0 \\ 0 & 0 & 0 & 2u \end{pmatrix} \delta(X). \quad (58)$$

Integrating (58) over the spectrum removes the δ-function. The resulting expression is identical to the cold plasma limit of the frequency integrated Mueller matrix (47). This is a good test of consistency of the analytical expression (55) for the frequency-resolved Mueller matrix. More systematic verification of (55) is performed numerically by integrating $\hat{\mathbf{m}}_{ij}(X, \mu, u)$ over the entire frequency interval $-1 \leqslant X \leqslant \infty$. The differences between the numerical values and corresponding exact results (47) do not exceed $(10^{-2}$–$10^{-3})\%$ in a broad range of T_e and u variations.

At finite temperatures, the spectral profiles (58) are broadened and shifted to blue part of the spectrum. As an example, the profile of the $m_{00}(X)$ element is illustrated by black lines in figure 9 at $T_e = 10$ keV and $T_e = 40$ keV while $\theta = 150°$ in both cases. Blue lines describe contribution $\hat{\mathbf{m}}_{ij}^{(0)}(X)$ from the first $n = 0$ term while red lines illustrate more accurate approximation (59) with the next order correction in $T_e/m_ec^2 \ll 1$. The spectral profiles of all other elements of $\hat{\mathbf{m}}_{ij}(X)$ are similar to $m_{00}(X)$ but have different amplitudes and signs. Their frequency integrated values are in a good agreement with the elements of the cold plasma matrix (58). For example, at $T_e = 40$ keV and $u = \cos 150° = -0.87$ the elements m_{22} and m_{33} are negative with peak values $\simeq -1.2$ while m_{01} is positive with a peak value $\simeq 0.12$. A more accurate approximation $\hat{\mathbf{m}}_{ij}^{(1)}$ is obtained by integrating by parts in (56) with the use of the identity $\mathrm{d}t\exp(-pt) = -\mathrm{d}(\exp(-pt))/p$ and ignoring the integral terms left after this operation

$$\hat{\mathbf{m}}_{ij}^{(1)}(X, \mu, u) = \left(C_{ij}^{(0)} + \frac{\sqrt{2(X+1)(1-u)}}{\mu} \times \sum_{n=1}^{n=4} \frac{C_{ij}^{(n)} k^{2n}}{(X+2)^{2n+1}} \right) E^{(0)}(p). \quad (59)$$

Performing integration by parts in (56) many times leads to the analytical presentation for $\hat{\mathbf{m}}_{ij}(X, \mu, u)$ in the form of the series expansion in powers of T_e/m_ec^2. Another method of expansion is described in appendix C.

6.2. Spectral power and depolarization factor

The fully relativistic frequency-resolved Mueller matrix (55) gives a general description of the polarization and spectral properties of the scattered radiation at arbitrary polarization of the incident light. To illustrate the connection of this formalism with previously developed approaches we will consider the power spectrum of the scattered TS radiation. Power spectrum characteristics are the key element of the standard spectral TS method of electron temperature measurement. There are a large number of publications devoted to different approximate treatments of the relativistic effects in the scattering operator [3, 4, 44–50]. An exact analytic formula for fully relativistic Thomson scattering spectrum was first derived in [3] including a term called the depolarization term (which differs from the degree of depolarization). As in most previous publications, it was assumed that the incident polarization is linear and perpendicular to the scattering plane, and only this component of the scattered wave electric field is measured. In this particular case, the scattered power is described by the well-known expression (see equation (5) in [44])

$$\mathrm{d}P_x/\mathrm{d}\omega \propto \frac{\omega^2}{\omega_i^2} \int \mathrm{d}\boldsymbol{\beta} f_M(\boldsymbol{\beta})(1-\beta^2) \times \left(1 - \frac{\beta_x^2(1-u)}{(1-\beta_s)(1-\beta_i)} \right)^2 \delta(\Delta\omega - \mathbf{k}\cdot\mathbf{v}), \quad (60)$$

where $\Delta\omega = \omega - \omega_i$ (note a misprint in (4.1.5) and (4.1.6) of [1] for this expression). If the detector measures all the components of the scattered electric field, then expression (60) is modified according to equation (4) of [44] with

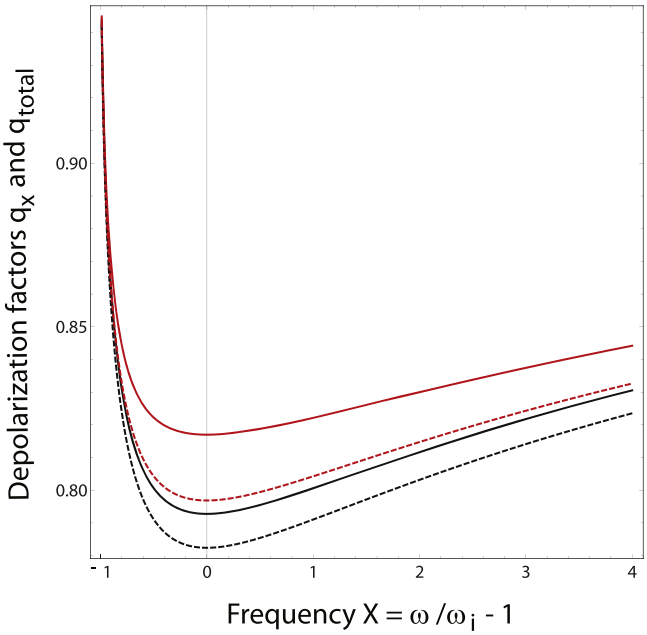

Figure 10. Depolarization factors $q_{\text{total}}(X)$ (red) and $q_x(X)$ (black) versus frequency $X = \omega/\omega_i - 1$ at $T_e = 40$ keV and two values $\theta = 150°$ (solid lines) and $\theta = 180°$ (dashed lines).

$$\Theta = \pi/2$$

$$dP_{\text{total}}/d\omega \propto \frac{\omega^2}{\omega_i^2}\int d\boldsymbol{\beta} f_M(\boldsymbol{\beta})(1-\beta^2) \times\left(1-\frac{\beta_x^2(1-\beta^2)(1-u)^2}{(1-\beta_s)^2(1-\beta_i)^2}\right)\delta(\Delta\omega - \mathbf{k}\cdot\mathbf{v}). \quad (61)$$

This situation is realized, for example, in Thomson scattering diagnostic system used for Madison symmetric torus reversed field pinch experiments. The spectral density $dP_{\text{total}}/d\omega$ includes all polarizations and is, therefore, larger than $dP_x/d\omega$ related to one selected direction. The difference between them is proportional to the factor b^2 in equation (27) integrated over the velocity space. This makes the difference of the powers relatively small ($\propto T_e/m_e c^2$).

The common feature of both expressions (60) and (61) is that the terms in the large brackets reduce the scattered power due to relativistic factors $\propto\beta_x^2$. Evaluation of their integral effect on the spectral powers requires full integration over $\boldsymbol{\beta}$ and is characterized in the literature by the depolarization factor $q(\omega, u, \mu) < 1$. Using this notation, the final result of exact calculations performed in [3] is presented in the form $dP_x/dX \propto S_Z(X, u, \mu)q_x(X, u, \mu)$. The spectral power density $S_Z(X, u, \mu)$ refers to the function derived previously in [45] and related to $E^{(0)}(p)$ as $S_Z = (X+1)^2E^{(0)}/kK_2(\mu)$.

In [45], the factor q_x was assumed constant, i.e., unity. A variety of other approximations for q_x have been suggested. For example, the relativistic corrections to first order in $\beta \ll 1$ were calculated in explicit form in [46]. The effect of the relativistic factors on blue line shift error analysis was performed in [47]. The relativistic corrections were extended to second order in [48]. The values of q_x were found with better precision in [49] for several electron temperatures and $u = 0$. The exact result for $q_x(X, u, \mu)$ is presented in [3] as a superposition of the two integrals similar to $E^{(1)}(p, r)$ and $E^{(2)}(p, r)$. These calculations were reproduced and the correctness of the results [3] was confirmed in [4] devoted to the special case $\theta = 180°$ for LIDAR scattering system. This work has been recently extended in [50] to a fully relativistic calculations valid for all scattering angles and both coherent and non-coherent regimes. The results are derived in a general form so further transformations are needed to present them in the explicit form relevant to the incoherent regime for comparison with already known cases. We will show now how both aforementioned spectral densities can be obtained from a general approach based on the frequency-resolved Mueller matrix (55).

Within the scope of the Mueller matrix formalism, the spectral density dP_x/dX measured by the detector in the x-direction is determined by a sum of the Stokes vector components $(S_0^{(s)} + S_1^{(s)})/2$ (see equation (1)). Assuming that the incident wave is linearly polarized in the same direction, $\mathbf{S}^{(i)} = (1,\ 1,\ 0,\ 0)$, gives the spectral power in terms of the Mueller matrix elements $dP_x/dX \propto (m_{01} + (m_{00} + m_{11})/2)$. Substituting (55) in this combination shows that the integrals $E^{(3)}$ and $E^{(4)}$ cancel out in the final expression for $dP_x/dX \propto S_z q_x$. The depolarization factor q_x is presented in a compact form by $E^{(1)}$ and $E^{(2)}$ integrals only

$$q_x = 1 + \frac{2\exp(p)(2+X)}{k}\left(E^{(1)}(p, r) - \frac{3(2+X)^2}{k^2}E^{(2)}(p, r)\right). \quad (62)$$

The spectral power density $dP_{\text{total}}/dX \propto S_z q_{\text{total}}$ is determined by a different combination $dP_{\text{total}}/dX \propto (m_{00} + m_{01})$. In this case, the matrix elements (55) lead to the expression containing three integrals

$$q_{\text{total}} = 1 + \frac{4\exp(p)(2+X)}{k}\left(E^{(1)}(p, r) - \frac{2(X+2)^2 + 3(1+u)(X+1)}{k^2}E^{(2)}(p, r) + \frac{5(1+u)(2+X)^2(1+X)}{k^4}E^{(3)}(p, r)\right). \quad (63)$$

Comparing (62) with equation (5) in [3] shows that after matching the variable of integration in $E^{(1)}(p, r)$ and $E^{(2)}(p, r)$ with the one used in [3] the results are identical. Together with the numerical verification, this gives an additional argument for the correctness of the exact relativistic solution (55).

The dependencies of the depolarization factors $q_x \leqslant 1$ and $q_{\text{total}} \leqslant 1$ on X are shown in figure 10 at $T_e = 40$ keV and two values $\theta = 150°$ and $\theta = 180°$ confirming, as expected, that $q_{\text{total}} > q_x$. Both q-factors reduce with θ and are smallest for the backscattered radiation with $\theta = 180°$, indicating that suppression of the spectral powers caused by the relativistic terms is the largest in this direction. This is a straightforward consequence of the $(1-u)$ dependencies in (60) and (61).

At a given T_e and θ the minima of both factors as functions of X is reached in the vicinity of $X = 0$. This is different from the spectral powers dP_x/dX and dP_{total}/dX

shown in figure 11 at $T_e = 40$ keV and $\theta = 150°$ where both extrema are blue shifted to $X \simeq 0.5$. In figure 11, the blue line illustrates the contributions from the dominant part $\hat{\mathbf{m}}_{ij}^{(0)}(X, \mu, u)$ of the Mueller matrix. They are the same for both spectral densities and coincide with the function $S_z(X)$. At $T_e = 40$ keV and $\theta = 150°$ the depolarization factors q_{total} and q_x result in (18–20)% reduction of the peak values of the spectral power.

To illustrate the effectiveness of the Mueller matrix we consider now the more general problem of optimization (maximization) of the spectral power densities $\mathrm{d}P_x/\mathrm{d}X$ and $\mathrm{d}P_{\text{total}}/\mathrm{d}X$ with respect to all possible polarizations of the incident light and directions of measurement of the scattered light. The universal character of the Mueller matrix method allows us to avoid kinetic calculations similar to (60) for each specific case of the incident or measured polarizations. After being calculated once, the five Mueller matrix elements (55) contain full information about the kinetic part of the problem. Then, the properties of the scattered radiation are fully described by simple algebraic products of five functions of X, μ and u already known, and trigonometric combinations of the polarization angles ψ and χ. This separation of variables is a key element of the method allowing performance of different optimizations in a general form without kinetic calculations.

The optimization (maximization) of the spectral densities can be done at some specific frequency, or for the entire frequency-integrated power, or for the spectral density integrated over a finite frequency band. To illustrate the approach, we show the results of optimization of the total frequency-integrated powers P_x and P_{total} described by (47). The same procedure, but based on consideration of the peak values, gives similar results. Analyzing the power P_x, we abandon the assumption that it is measured with a polarizer that selects the scattered wave electric field component in only one x-direction perpendicular to the scattering plane. Instead, the more general case is considered of an arbitrary orientation of the polarizer that selects the scattered wave electric field in the $\mathbf{e}_\alpha$-direction perpendicular to $\mathbf{s}$ but having some angle $0 \leqslant \alpha \leqslant \pi$ between $\mathbf{e}_x$ and $\mathbf{e}_\alpha$. In the new reference frame, the power P_α is proportional to the product of the components $\langle E_\alpha E_\alpha^\star \rangle = (S_0^{(s)\prime} + S_1^{(s)\prime})/2$ (see equation (1)). The total power consists of this term and similar products of the components orthogonal to $\mathbf{e}_\alpha$, $P_{\text{total}} \propto S_0^{(s)\prime}$. The prime symbol for the scattered Stokes vector $\mathbf{S}^{(s)\prime}$ indicates that it is calculated in the reference frame obtained by a rotation of the axes through the angle α over the scattered direction $\mathbf{s}$ (different from the reference frame (11) with the unit vectors orthogonal to the incident direction $\mathbf{i}$ and characterized by the azimuth ψ).

The rules of transformation of the Stokes vector components for a rotation of the axes through the angle α are given by the formulas

$$S_0^{(s)\prime} = S_0^{(s)},\ S_1^{(s)\prime} = S_1^{(s)}\cos 2\alpha - S_2^{(s)}\sin 2\alpha,\ S_2^{(s)\prime} = S_1^{(s)}\sin 2\alpha + S_2^{(s)}\cos 2\alpha,\ S_3^{(s)\prime} = S_3^{(s)}. \tag{64}$$

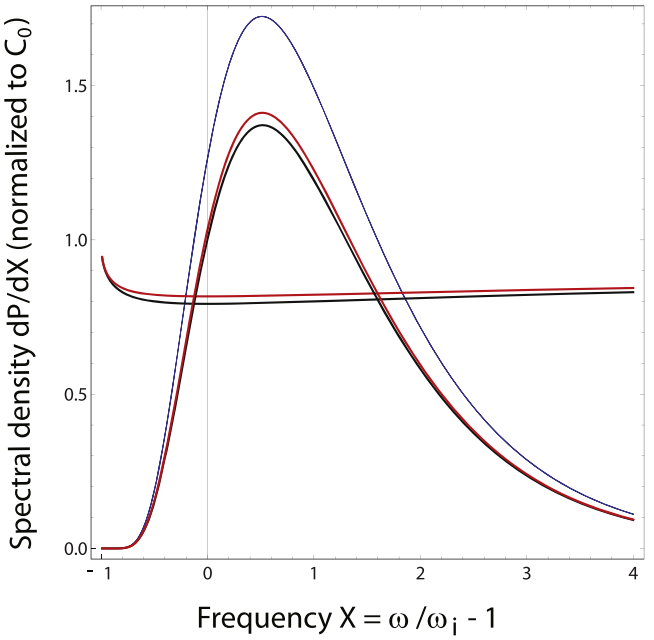

Figure 11. Normalized to C_0 spectral densities $\mathrm{d}P_{\text{total}}/\mathrm{d}X$ (red) and $\mathrm{d}P_x/\mathrm{d}X$ (black) versus frequency $X = \omega/\omega_i - 1$ at $T_e = 40$ keV and $\theta = 150°$. Blue line is the contributions from the dominant part $\hat{\mathbf{m}}_{ij}^{(0)}(X, \mu, u)$ (coincides with the function $S_z(X)$). Black and red horizontal lines illustrate that the depolarization factors shown in figure 10 are almost constant on this scale.

By making use of (64), the function P_α is expressed in terms of the original Stokes vector $\mathbf{S}^{(s)}$. It is linked, in turn, with the Stokes vector of the incident radiation (2) by equation $\mathbf{S}^{(s)} \propto \hat{\mathbf{m}} \cdot \mathbf{S}^{(i)}$ such that $S_0^{(s)} \propto m_{00} + m_{01}\cos 2\psi \cos 2\chi$, $S_1^{(s)} \propto m_{01} + m_{11}\cos 2\psi \cos 2\chi$, $S_2^{(s)} \propto m_{22}\sin 2\psi \cos 2\chi$. This yields the power P_α as a function of ψ, χ and α measured in the component of the scattered wave electric field along the arbitrary $\mathbf{e}_\alpha$-direction

$$\begin{aligned} P_\alpha &\propto m_{00} + m_{01}\cos 2\psi \cos 2\chi + (m_{01} \\ &\quad + m_{11}\cos 2\psi \cos 2\chi)\cos 2\alpha \\ &\quad + m_{22}\sin 2\psi \cos 2\chi \sin 2\alpha, \\ P_{\text{total}} &\propto m_{00} + m_{01}\cos 2\psi \cos 2\chi. \end{aligned} \tag{65}$$

In equation (65), the reference direction for α is opposite to equation (64) ($\alpha \to -\alpha$).

At given T_e, u and α the maxima of P_α and P_{total} as functions of ψ and χ are reached at the boundaries of the polarization region $0 \leqslant \psi \leqslant \pi/2, 0 \leqslant \chi \leqslant \pi/4$. They can be analyzed by plotting P_α and P_{total} along four boundaries of the polarization region. The results are shown in figure 12 as functions of a parameter $0 \leqslant \xi \leqslant 4$. The variable ξ is introduced to express the changes of the polarization characteristics $\cos 2\psi$ and $\cos 2\chi$ along the four boundaries as some linear functions of ξ. The functions are scaled in such a way that each of four boundaries corresponds to equal interval of ξ variation $\Delta\xi = 1$ (see appendix A.1). The upper curve consists of four straight lines of different colors. Each of them illustrates variation of P_{total} along the corresponding boundary of the polarization angles. The variations of P_{total} are relatively weak

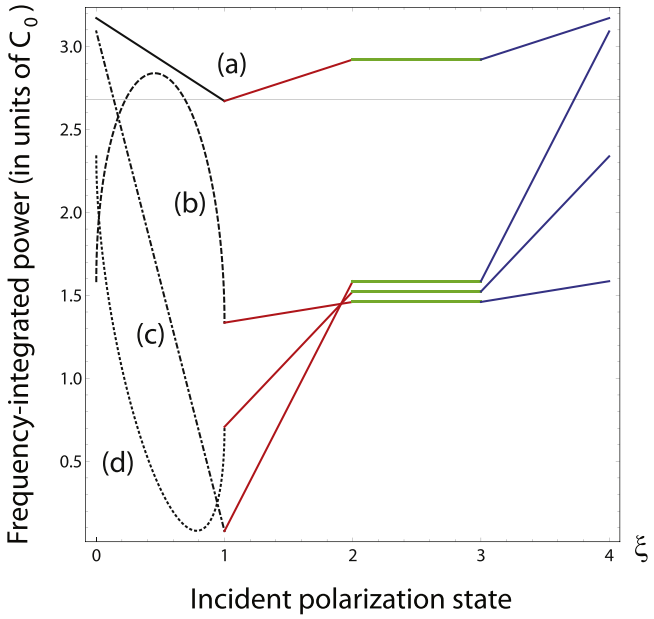

Figure 12. Plots of normalized to C_0 frequency-integrated powers P_{total} (upper curve (a)) and P_α (three lower curves (b), (c), (d)) along the boundaries of the polarization angles ψ and χ at $T_e = 40$ keV and $\theta = 150°$. The solid black line shows variation of P_{total} while three other black lines show variation of P_α as a function of ψ along the first boundary ($0 \leqslant \psi \leqslant \pi/2,\ \chi = 0$) at $\alpha = 0$ (dotted–dashed line (c)), $\alpha = -35°$ (dotted line (d)) and $\alpha = 40°$ (dashed line (b)). The red, green and blue curves describe power variations along three other boundaries: ($\psi = \pi/2,\ 0 \leqslant \chi \leqslant \pi/4$), ($\pi/2 \geqslant \psi \geqslant 0,\ \chi = \pi/2$) and ($\psi = 0,\ \pi/4 \geqslant \chi \geqslant 0$), respectively.

and its absolute maximum is reached at $\xi = 0$ (linear incident polarization perpendicular to the scattering plane).

Three lower curves describe the dependence of P_α on the incident polarization state. They are plotted for three different angles $\alpha = -35°,\ 0°$ and $40°$. When the power P_α is measured at $\alpha = 40°$, there appears a local maximum of P_α as a function of ψ that corresponds to linear incident polarization with the orientation angle $\psi \simeq \alpha$. The value of P_α at this local maximum is smaller than the absolute maximum of P_α reached at $\alpha = 0°$ and linear incident polarization perpendicular to the scattering plane. Thus, the optimization of the spectral power with respect to all possible incident polarizations and directions of the scattered wave electric field shows that the combination $\psi = \chi = \alpha = 0$ provides an absolute maximum of the scattered signal.

6.3. Frequency-resolved degree of depolarization

The frequency-resolved degree of depolarization is defined as $D(\omega) = 1 - P(\omega)$ where $P(\omega)$ is given by (49). The spectral Stokes vector of the scattered radiation, $\mathbf{S}^{(s)}(\omega) = \hat{\mathbf{M}}(\omega, \mu, \theta) \cdot \mathbf{S}^{(i)}(\psi, \chi)$, is determined by the frequency-resolved Mueller matrix (50) and the Stokes vector of the incident wave. Since $P(\omega)$ is a ratio of the two $\mathbf{S}^{(s)}$-dependent terms, the normalization factor C_0 cancels out in the final expression. Thus, the degree of polarization/depolarization is completely determined by the elements of the matrix $\hat{\mathbf{m}}_{ij}(X, \mu, u)$ (55) and the Stokes vector of the incident wave (2). It depends on the angles of the incident polarization ψ and χ, electron temperature, the scattering angle and the frequency of the scattered radiation X.

If the frequency-resolved Mueller matrix is approximated by the first dominant term $\hat{\mathbf{m}}^{(0)}(X, \mu, u)$ with $n = 0$, then the corresponding degree of depolarization in identically equal to zero. In spite of the complicated dependencies of $C_{ij}^{(0)}$ on X and u, the degree of depolarization is zero for all incident polarizations, electron temperatures, scattering angles and the frequency of the scattered radiation. This indicates that finite values of the degree of depolarization are caused by the integral terms in equation (55) (see also equation (C17)).

At given X, the properties of $D(X)$ dependencies on T_e and θ are similar to those presented in figures 6 and 7 for the frequency-integrated Mueller matrix. The spectral dependence of $D(X)$ characterizes the sensitivity of the degree of depolarization to the frequency of the scattered radiation. In figure 13, typical examples of the spectral profiles $D(X)$ are shown at $T_e = 40$ keV and three scattering angles $\theta = 130°,\ 150°$ and $180°$. At all scattering angles, the functions $D(X)$ have maxima at the frequency approximately equal to the frequency of the incident wave ($X \simeq 0$). The peak values are about 15% higher than the degrees of depolarization shown by dashed lines and calculated at the same T_e and θ with the use of the frequency-integrated Mueller matrix. The right panel illustrates the dependence of the peak values $D(0)$ on incident polarization by plotting them along four boundaries of the polarization angles at $\theta = 130°$ (solid lines). The values of D determined from the frequency-integrated Mueller matrix are shown by dashed lines. Both solid and dashed curves demonstrate similar behavior but with different amplitudes.

Comparing profiles $D(X)$ at different scattering angles in figure 13 shows that the degree of depolarization is strongest near perpendicular scattering and drops off rapidly far away from this direction. As pointed out seemingly by Sheffield [51], this behavior of the rigorously-defined degree of depolarization $D(X)$ contradicts behavior of the depolarization if we measure it in terms of deviation from unity of the depolarization factors q discussed in section 6.2. Considering the quantity $1 - q$ as an intuitive measure of depolarization shows that this characteristic increases with θ and reaches its maximum for backscattered radiation at $\theta = 180°$ (see figure 10). This tendency is the opposite of $D(X)$ behavior and reflects deep physical difference between D and q.

Indeed, as seen from (60) and (61), the reduction of the intensity caused by the relativistic terms in the q-factors takes place even for scattering on a single moving electron ($1 - q > 0$). In the same case of a single moving electron, the scattered radiation remains monochromatic and, therefore, completely polarized with $D = 0$ (see equation (39)). Partially polarized TS radiation with $D > 0$ is caused by the superposition effect of randomly moving electrons.

Consider, for example, a linearly polarized incident wave with the Stokes vector (1, 1, 0, 0). After scattering on a single moving electron the matrix $\hat{\mathbf{W}}$ yields the scattered radiation

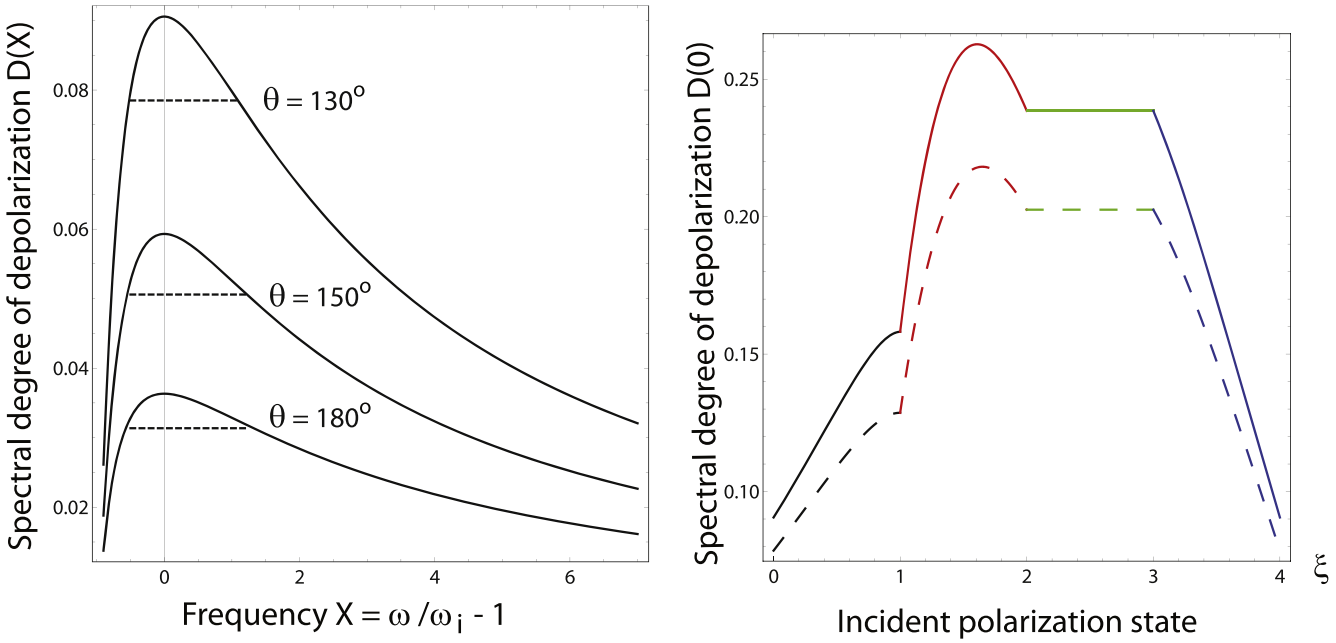

Figure 13. Left panel: spectral dependence of the degree of depolarization $D(X)$ for linear incident polarization with $\psi = 0$ at $\theta = 130°$, $150°$ and $180°$ (solid lines); the degree of depolarization at the same angles from the frequency-integrated Mueller matrix (dashed lines). The right panel: dependence of the peak values $D(0)$ on incident polarization along four boundaries of the polarization angles at $\theta = 130°$ (solid lines). The values of D for the frequency-integrated Mueller matrix are shown by dashed lines (all curves correspond to $T_e = 40$ keV).

with $S_0^{(s)} \propto 2(a^2 + b^2)$, $S_1^{(s)} \propto 2(a^2 - b^2)$, $S_2^{(s)} = -4ab$, $S_3^{(s)} = 0$ that provides $D = 1 - \sqrt{S_1^{(s)2} + S_2^{(s)2}}\ /S_0^{(s)2} = 0$. Averaging over randomly moving electrons modifies the Mueller matrix in such a way that $S_2^{(s)} = -4\overline{ab} = 0$. This results in non-zero degree of depolarization $D = 2\overline{b^2}/(\overline{a^2} + \overline{b^2})$.

The simplest example of linear incident polarization perpendicular to the scattering plane allows us to express the degree of depolarization in terms of the depolarization factors q_x and q_{total} and analyze the relationship between them

$$D = (S_0^{(s)} - S_1^{(s)})/S_0^{(s)} = 2(P_{\text{total}} - P_x)/P_{\text{total}} = 2(q_{\text{total}} - q_x)/q_{\text{total}} \simeq 2(q_{\text{total}} - q_x). \quad (66)$$

Thus, the degree of depolarization is linked not to the depolarization factors q_{total} or q_x but to the difference between them. Using the expressions in large brackets in (60) and (61) yields an estimate for this difference to a leading order approximation in $\beta_x^2 \ll 1$

$$q_{\text{total}} - q_x \simeq [2(1-u) - (1-u)^2]\overline{\beta_x^2} = (1-u^2)\overline{\beta_x^2}. \quad (67)$$

These arguments explain why large depolarization of the backscattered radiation ($\theta = 180°$, $u = -1$) measured in terms of $1 - q_x \propto 2(1-u)$ and $1 - q_{\text{total}} \propto (1-u)^2$ is accompanied by small depolarization measured in terms of the degree of depolarization $D \propto (1-u^2)\overline{\beta_x^2}$.

More general analysis of the $D(X)$ dependence is performed in appendix C for the case of arbitrary incident polarization. The strongly peaked at small T_e Gaussian part of the spectral profile $E^{(0)}(p)/K_2(\mu)$ cancel out in the expression (C17) for $D(X)$. Residual terms are proportional to $\delta\hat{\mathbf{m}}$. They determine the spectral degree of depolarization $D(X)$ which varies with X on temperature-independent scale of order unity with the amplitude proportional to $T_e/m_e c^2$.

6.4. Polarization over a finite frequency band

The aforementioned theoretical analysis is performed for two limiting cases of the frequency-resolved and frequency-integrated degree of depolarization. Realistic experimental constraints require accepting only scattered photons within a limited wavelength range. To evaluate the feasibility of a polarimeter under these conditions, we will use the spectral results (55) to calculate the quantitative effect of the finite frequency response band of optical instrumentation on the accuracy of polarization-based measurements.

Consider a partial contribution $\Delta\mathbf{S}^{(s)}$ to the spectrum integrated Stokes vector from a finite frequency interval $\Delta\omega$. It was evaluated previously in this section at small $\Delta\omega$ as $\Delta\mathbf{S}^{(s)} = \mathbf{S}^{(s)}(\omega)\Delta\omega$ and used as a basis for the frequency-resolved polarization formalism. We treat now the partial contribution in its precise form

$$\Delta\mathbf{S}^{(s)} = \int_{\omega-\Delta\omega/2}^{\omega+\Delta\omega/2} \mathbf{S}^{(s)}(\omega)\mathrm{d}\omega. \quad (68)$$

In the limit $\Delta\omega \to \infty$, the integral (68) reproduces the value of D shown by the dashed lines while in the opposite limit, $\Delta\omega \to 0$, it corresponds to the profile $D(X)$ shown by the solid lines in figure 13. Integrating Mueller matrix (55) over the finite frequency interval according to (68) and comparing the degree of depolarization $\overline{D}(\omega)$ resulting from this operation with the two limiting cases yields important information about characteristic values of $\Delta\omega$ at which the

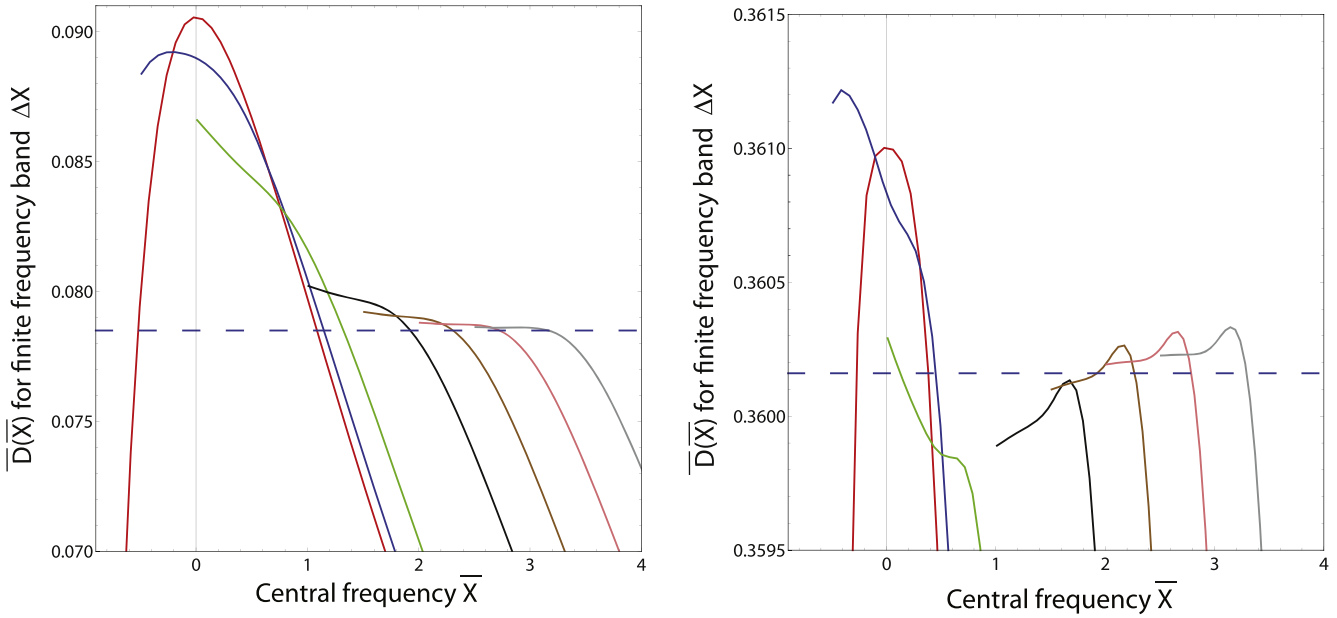

Figure 14. Degree of depolarization caused by the partial contribution $\Delta\mathbf{S}^{(s)}$ from finite frequency interval ΔX versus position of the center of the interval $\overline{X}$ ($\Delta X/2 - 1 \leqslant \overline{X} \leqslant 4$): $\Delta X = 0$ (red), 1 (blue), 2 (green), 4 (black), 5 (brown), 6(pink), 7 (gray), degree of depolarization for frequency-integrated Mueller matrix (dashed line). Plasma scattering and incident polarization parameters are $T_e = 40$ keV, $\theta = 130^\circ$, $\psi = \chi = 0$ (linear polarization perpendicular to the scattering plane,left panel); $\theta = 95^\circ$, $\chi = \pi/4$ (circular polarization, right panel).

transition between frequency-integrated and frequency-resolved limiting case takes place. Averaging of the Mueller matrix elements (55) needed for this analysis is performed numerically by integrating over the interval $\overline{X} - \Delta X/2$, $\overline{X} + \Delta X/2$. This yields the partial contributions to the Stokes vector (68) and corresponding degree of depolarization as a function of the central frequency $\overline{X}$ and the interval of integration ΔX.

The results are presented in figure 14 as functions of $\overline{X}$ at $T_e = 40$ keV and $\theta = 130^\circ$ for a few values of ΔX. At $\Delta X = 0$, the spectral profiles correspond to the frequency-resolved curves illustrated in figure 13. When the X-integration is performed over a finite interval ΔX, possible coordinates $\overline{X}$ of the center of this window of integration are limited from the left by the inequality $\overline{X} \geqslant \Delta X/2 - 1$. For this reason, the left boundaries of the curves shown in figure 14 for increasing values of ΔX are monotonically shifted to the right. At $\theta = 130^\circ$, the integration over the relatively large interval $\Delta X = 1$ ($\Delta\omega = \omega_i$, blue curve) does not lead to significant deviation of $D(X)$ from its frequency-resolved profile (red curve). Only if the frequency band of the optical detectors is wide ($\geqslant(3 - 4)\omega_i$) then the measured degree of depolarization approaches its asymptotic value predicted by the frequency-integrated Mueller matrix theory. Otherwise, a difference of order of 15% is expected to be observed in the vicinity of the incident frequency ω_i.

This conclusion is made for $\theta = 130^\circ$ and valid for the broad range of incident polarizations. The results are sensitive to the scattering angles. Another example with $\theta = 95^\circ$ and circular incident polarization shown in the right panel of figure 14 illustrates an opposite situation. In this case, the peak value of the frequency-resolved degree of depolarization is very close to its frequency-integrated analog. Averaging over different intervals ΔX gives slightly irregular curves but all values of $\overline{D}\,(\overline{X})$ turn out to be in the vicinity ($\leqslant 0.1\%$) of the degree of depolarization calculated from the frequency-integrated model.

7. Experimental implementation of a polarization diagnostic for T_e

The suggestion that T_e might be measured by observing the depolarization of TS light appears at least as early as 1968 [6]. The first assessment of the practical possibility of this technique was made by Orsitto and Tartoni in 1999 [7]. They performed a numerical calculation using the scattering cross section derived in [52], for the case in which the incident and scattered wave vectors are at 90°. The incident light was linearly polarized, with a polarization plane at 45° to the plane defined by the incident and scattered wave vectors. The depolarization of the scattered light was found to be almost independent of wavelength, and increased nearly linearly with T_e up to a temperature of 20 keV. The conclusion about independence from the wavelength was made on the basis of quantum electrodynamics cross section analysis in [52]. This is consistent with the results obtained from the classical field theory in section 6 that predict relatively flat frequency profile of the degree of depolarization for scattering at $\theta = 95^\circ$ of the incident circularly polarized light (figure 14 (right panel)).

To exploit these polarization characteristics for T_e measurement, the simple apparatus illustrated in figure 15 was proposed. This device measures the number of photons

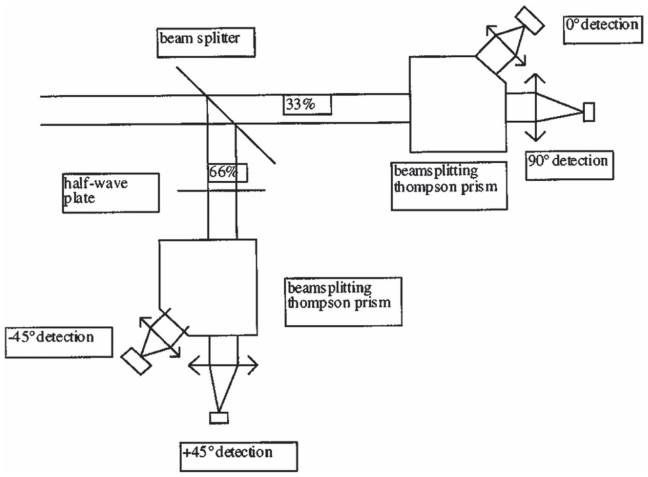

Figure 15. Schematic of a simple polarimeter proposed for measurement of Thomson scattered signal at angles of $+45°$, $-45°$, and $90°$ from the scattering plane. Reproduced from [7], with the permission of AIP Publishing.

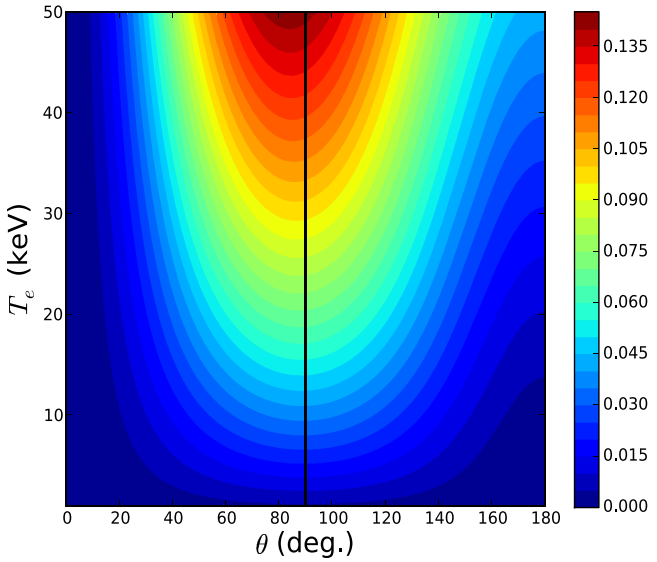

Figure 16. The degree of depolarization for linearly polarized incident light with $\psi = 0$, across the full range of scattering angles and fusion-relevant temperatures. Reproduced from [13]. © IOP Publishing Ltd. All rights reserved.

through polarizers at angles of $+45°$, $-45°$, and $90°$ with respect to the plane defined by the incident and scattered wave vectors. Using incident laser light at 1064 nm and collecting scattered light in the range 660–1050 nm, and with the assumptions of Poisson statistics for uncertainties, bremsstrahlung for background light from the plasma, and no losses in the detection apparatus, the uncertainty for a measured T_e of 20 keV was estimated to be competitive with the usual spectral method of Thomson scattering measurement. This calculation demonstrated that a Thomson scattering diagnostic based on polarization measurement is a realistic possibility for high-temperature plasmas.

A more complete optimization of this type of diagnostic scheme was done using an analytic description of the Thomson scattering process valid for all incident polarization states, scattering angles, and electron temperatures [13]. Expressed in Stokes vector form, the scattered field, $\mathbf{S}^{(s)}$, and the incident field, $\mathbf{S}^{(i)}$, have four components $\mathbf{S} = (S_0, S_1, S_2, S_3)$. For fully polarized incident light, scattered light from a single electron remains completely polarized, but due to the nature of the electron distribution function, light scattered from many electrons will include photons of many different polarization states. This is described by the degree of polarization, P, which can range from 0 to 1, and the degree of depolarization, $D = 1 - P$, given by equation (3).

Figure 16 shows the degree of depolarization across the full range of scattering angles and fusion-relevant temperatures for linearly polarized light with the orientation angle, ψ, between the major axis of the polarization ellipse and the normal vector to the scattering plane equal to zero (light polarized perpendicular to the scattering plane). Depolarization is strongest near perpendicular scattering, although not exactly at a scattering angle $\theta = \pi/2$, a result that is consistent with earlier calculations [8, 9]. For both forward (θ near zero) and backward (θ near π) scattering, the degree of depolarization is only a few percent at expected fusion reactor temperatures. This means that backward scattering LIDAR systems of the type initially proposed for the ITER experiment [38, 39] would be unsuitable for polarization-based measurement of T_e.

Diagnostic simulations using this analytic description for 2-, 3-, and 4-component polarization selection apparatus indicated good performance for all schemes above about 10 keV. The laser source was at 1064 nm and scattered radiation integrated over the range 200–2000 nm. For optimization, the diagnostic error bars are calculated and minimized with respect to polarization characteristics of the incident light ψ and χ and scattering angle θ. In the general case of elliptically polarized incident light, four Stokes vector components of the scattered light should be measured. Modifying the standard scheme of six measurable intensities [23], four independent intensities I_α given by (7) were selected in [12, 13] to determine $\mathbf{S}^{(s)}$. Three of them are measured after the light is separated by beamsplitters and transmitted by three polarizers that select linear polarization at the azimuth angles $0°$, $45°$ and $90°$ with respect to the perpendicular to the scattering plane. The fourth channel contains a quarter-wave plate to create $\pi/2$ retardation of the in-plane component before the light is transmitted by the $45°$ polarizer. The degree of depolarization measurement error, σ_D, is related to the error on each of the statistically independent intensity measurements σ_{I_α}

$$\sigma_D^2 = \sum_\alpha \left(\frac{\partial D}{\partial I_\alpha}\right)^2 \sigma_{I_\alpha}^2,$$

where the intensity measurement errors are determined by Poisson statistics such that $\sigma_{I_\alpha}^2 \propto I_\alpha$.

The relative error in the electron temperature measurement, $\sigma_{T_e}/T_e = \sigma_D (T_e \partial D/\partial T_e)^{-1} = W/(\sqrt{Q}\, T_e \partial D/\partial T_e)$, is presented by a product of two universal functions $W(\psi, \chi, \theta, T_e)$ and $(\partial D/\partial T_e)^{-1}(\psi, \chi, \theta, T_e)$ with a scaling factor $1/\sqrt{Q}$ which does not depend on the polarization variables (Q is effectively proportional to the total number of scattered photons). The factorization allows us to perform

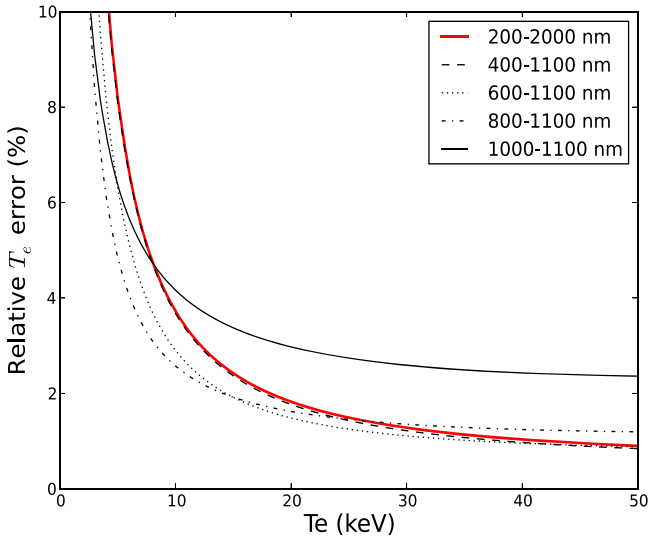

Figure 17. Comparison of predicted uncertainty in temperature measurement using a 2-component polarimeter, integrating over several different wavelength ranges. Reproduced from [13]. © IOP Publishing Ltd. All rights reserved.

minimization of σ_{T_e} analytically for the full range of incident polarizations, scattering angles, and electron temperatures. Although figure 8 shows that at $\theta = 90°$ and $\theta = 120°$ the derivative $\partial D/\partial T_e$ is the largest for circular polarization, fast growth of W in this parameter range determines the overall minimum of the error bars at linear incident polarization with $\chi = \psi = 0$. This proves that the regime of linear polarization with $\psi = 0$ is optimal not only because of the convenience of two-channel measurements but due to intrinsic polarization properties of TS radiation.

A more detailed description of the optimization scheme is presented in [13]. In particular, the simple 2-component polarimeter (selecting angles of 0° and 90° relative to the electric field with $\psi = 0$) performed best across the full range of temperatures up to 50 keV. Further simulations using the 2-component polarimeter and restricting the range over which the scattered radiation was integrated are illustrated in figure 17. Predicted uncertainty in measured T_e is relatively small even for an integration window of only 800–1100 nm. Such a window rejects a significant number of scattered photons, but it rejects an even greater fraction of the bremsstrahlung background, thus preserving measurement capability. This capability to make a measurement with a limited wavelength window may be of substantial advantage in a reactor environment where radiation darkening of optical fibers may limit scattered light collection to wavelengths above 500 nm [53].

A conceptual design for a polarimetric Thomson scattering diagnostic for ITER has recently been proposed by Giudicotti *et al* [21]. The ITER core Thomson scattering system has a backward scattering geometry with the scattering angle covering the approximate range $130° \leqslant \theta \leqslant 160°$, with the largest angles for the central measurement locations in the highest temperature region of the plasma [54]. Layout of the laser beam inside the plasma and the collection optics of the core TS system of ITER are illustrated in figure 18. All seven rays of the scattered radiation lie in one vertical poloidal plane. Position (1) corresponds to a scattering angle $\theta = 160°$ and radial location $r = R - R_0 = -0.1a$. Edge plasma position (7) has $\theta = 130°$ and $r = 0.84a$. The plasma center ($r/a = 0$) is between positions (1) and (2). Position (4) ($\theta = 145°$) is a representative of a typical measurement. It corresponds to the center of the measurement chord that has a radial location $r = 0.5a$. This area is in the middle between the plasma center and the outer wall and, therefore, the temperature will likely be less than 40 keV at that location.

With these large scattering angles, the TS spectrum spreads over a wavelength region spanning 200–1500 nm, with a peak intensity around 550 nm at 40 keV due to the relativistic blue shift of the scattered light (see figure 19 and equivalent spectral density profile as a function of frequency in figure 11). This presents a difficult challenge for spectral measurement of T_e, as optical fiber darkening sets a lower wavelength limit of about 500 nm, and the responsivity of Si avalanche photodetectors sets an upper limit around 1100 nm. This limited detection range causes the uncertainty in T_e to rise dramatically above 20 keV for a spectral measurement system. This limitation of the spectral measurement approach is illustrated in figure 20 at the representative scattering angle $\theta = 145°$. The rise in relative uncertainty in T_e and electron density n_e is plotted for three different choices of short wavelength cutoff by the scattered light collection system. By way of contrast, polarimetric measurement of T_e improves for increasing temperature and is almost independent of wavelength cutoff. Simulation of polarimetric measurement was performed using an input laser beam with circular polarization, as this maximizes the depolarization of scattered radiation in a backward-scattering geometry. The detection system was assumed a simple two-channel polarimeter measuring the left- and right-circularly polarized light. Since these correspond to two orthogonal polarization states, all scattered light is detected in one channel or the other.

Perhaps the best choice for core Thomson scattering measurement in ITER is a combination of spectral and polarimetric methods [22]. As proposed, the polychromator has a standard set of six spectral channels with a short wavelength cutoff of 600 nm. The scattered light collection system is arranged to split the light into two mutually orthogonal polarization states, with the light reflecting the polarization state of the input laser beam transported to the polychromator, and the depolarized light sent to a single polarimetric channel. While this hybrid scheme works well for linear horizontal (toroidal) input laser beam polarization, the lowest T_e uncertainty is predicted for a circularly polarized input beam (figure 21). Application of this scheme to the ITER core Thomson scattering diagnostic would require the installation of a second set of optical fibers, as the polarization splitting of the scattered light must be done before the light enters fibers for transport to the detection systems. Calibration of a polarimetric Thomson scattering measurement system would also be required, but this may be possible using the polarization properties of rotational Raman scattering of laser

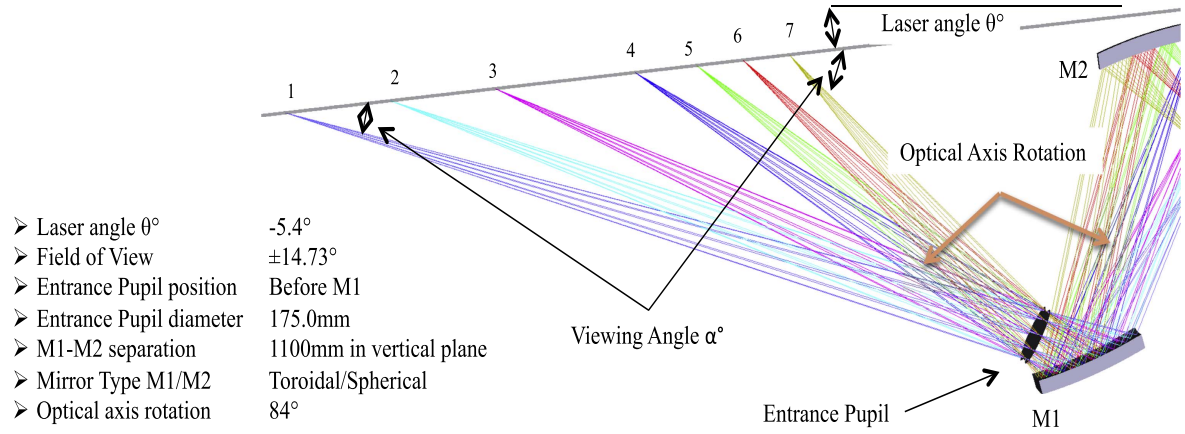

Figure 18. Layout of the plasma facing part of the collection optics of the core TS system of ITER. Reproduced from [21]. © IOP Publishing Ltd. All rights reserved.

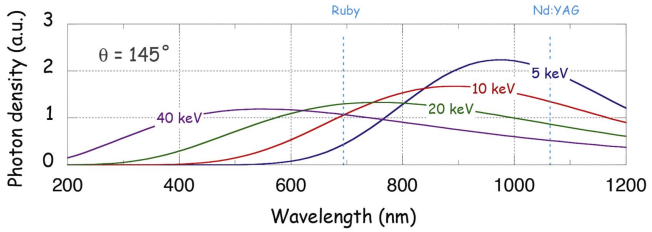

Figure 19. Predicted Thomson scattered photon spectra for temperatures and scattering angle $\theta = 145°$ relevant to ITER, using incident laser light at 1064 nm. Reproduced from [21]. © IOP Publishing Ltd. All rights reserved.

light from diatomic gases [19, 20]. Note that even a spectral measurement Thomson scattering system may require polarimetric calibration, as a severe plasma environment (such as in ITER) will change the polarization characteristics of the plasma-exposed first mirror.

In sum, for measurement of T_e in fusion-relevant plasma conditions, polarimetric techniques are competitive with the standard spectral measurement technique. The main advantages of polarimetry in this situation spring from two factors: (1) scattered light collected in a limited spectral region can be effectively analyzed because of the depolarization effect is largely wavelength independent (versus the need to cover a large wavelength range for effective spectral measurement), and (2) a basic implementation requires only a simple two-channel polarimeter (versus a multi-channel polychromator). As of this writing, no experimental tests of a polarimetric Thomson scattering diagnostic technique have been performed, although the JET tokamak has been suggested as a possible testbed [21], and temperatures in the W7-X stellarator are also likely to reach relevant levels.

8. Summary

When a Mueller matrix representation of Thomson scattering is averaged over electron thermal motion, it does not conserve polarization and transforms fully polarized incident light to partially polarized scattered radiation. This property is intrinsically connected with the broadening of the scattered spectrum, which, by definition, is no longer fully polarized. If the dependence of the degree of polarization on electron temperature is accurately known from theory, the accuracy of such a diagnostic could potentially exceed that of the conventional spectrum-based TS diagnostic method. Indeed, when the scattered spectra are broad, as in fusion-grade plasmas, and the optical instrumentation for scattered light analysis accepts a broad range of wavelengths, then the degree of depolarization is determined by the frequency-integrated components of the Stokes vector $\mathbf{S}^{(s)}$. These are linked to the polarization of the incident wave via the frequency-integrated Mueller matrix $\hat{\mathbf{M}}$ derived in section 5. The capability of a polarization-based TS diagnostic to integrate over a broad range of the scattered spectrum results in an increased number of detected photons and improved measurement accuracy. This is a key potential advantage of a polarization-based TS diagnostic compared to the traditional spectrum-based TS method.

An additional advantage of a diagnostic method based on the degree of depolarization arises from the fact that this quantity is defined as a ratio of the intensity in the unpolarized component to the total intensity of the scattered radiation. Both of them are proportional to plasma density and, therefore, the degree of depolarization is not sensitive to electron density, enabling direct measurement of electron temperature in a broad range of plasma conditions.

If the wavelength range of the instrumentation used to detect polarization is narrow, calculation of the spectrum-resolved degree of depolarization is relevant to the analysis. This is calculated from the frequency-resolved components of the Stokes vector $\mathbf{S}^{(s)}(\omega)$ which are linked to the incident wave through the frequency-resolved Mueller matrix $\hat{\mathbf{M}}(\omega)$. An exact relativistic solution for the frequency-resolved $\hat{\mathbf{M}}(\omega)$ and the spectral degree of depolarization is obtained and analyzed in section 6. In the parameter range relevant to the conventional TS system of ITER, the peak of the spectral degree of depolarization is

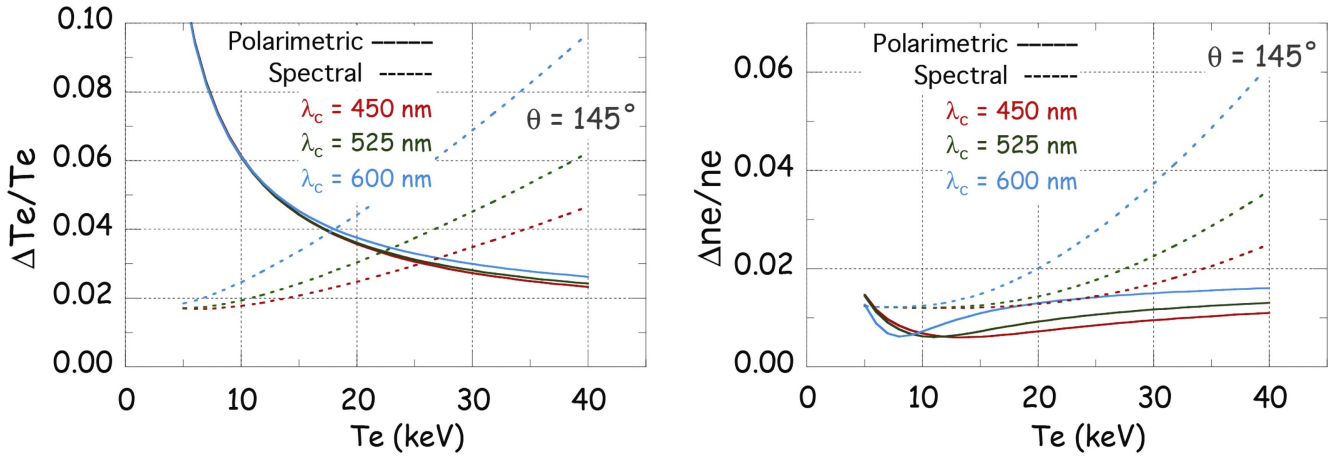

Figure 20. Comparison of the predicted relative error on T_e and n_e measured by polarimetric and spectral Thomson scattering as functions of T_e and for three different choices of the short wavelength detection cut-off. Reproduced from [21]. © IOP Publishing Ltd. All rights reserved.

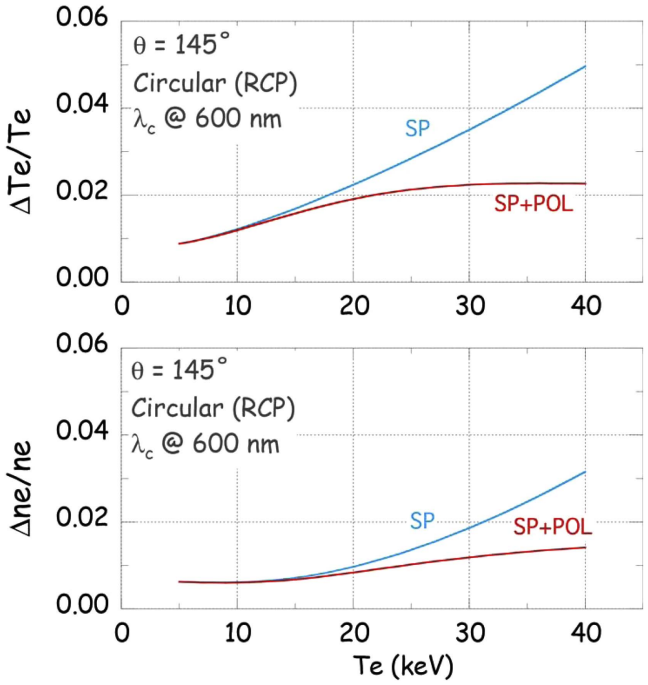

Figure 21. Predicted relative uncertainty of T_e and n_e with spectral Thomson scattering only (SP), and with an additional polarimetric channel (SP+POL) for incident laser beam with circular polarization. Reproduced with permission from [22].

achieved at a wavelength close to the wavelength of the incident laser light. The peak value is about 15% larger than the equivalent constant value of the degree of depolarization obtained from the frequency-integrated model. Both models are consistent with each other and both are useful for the approximate calculations usually required in diagnostic design scoping exercises. For more precise analysis, the intermediate case must be considered and serves as a bridge between these two limiting regimes. The intermediate case corresponds to a situation in which polarization measurements are made with optical instrumentation having a finite wavelength acceptance band. Example calculations for one particular case of $T_e = 40$ keV and two scattering angles $\theta = 130°$, $95°$ are examined in section 6.4 and illustrate the transition between the two limiting results as the wavelength bandwidth of the detection apparatus increases. This general analytical approach that explicitly includes the finite wavelength bandwidth of optical instrumentation, and treats it as an input parameter, is highly desirable for precise optimization of polarization-based TS diagnostic systems.

Global analysis of the degree of depolarization in terms of its dependence on T_e and θ shows that at high T_e forward scattering at $\theta < 90°$ is more favorable for polarization-based TS diagnosis than backscattering at the supplementary angle $180° - \theta$. In this sense, the planned ITER core TS system with predominantly backward scattered collection optics is not optimal for implementation of polarization-based diagnosis. This geometrical constraint in ITER reduces the advantages of a TS diagnostic based solely on polarization analysis, but opens the attractive possibility of using a hybrid scheme based on the combination of spectral and polarimetric methods for Thomson scattering measurement. The hybrid scheme is most effective for the ITER core TS system, where the combination of a wide spectrum (due to high T_e and a backward scattering geometry) and spectral cut-off at $\lambda \simeq 550$–600 nm (due to poor trasmission of refractive elements and neutron irradiated fiber optics) is expected to limit the performance at $T_e > 25$ keV. Under these conditions, polarimetric TS may effectively improve the performance of the ITER core TS system.

In addition to the ITER core TS application there are a number of other opportunities for implementing polarization-based Thomson scattering diagnostics. As of this writing, an attempt to measure the depolarization effect on TS radiation has recently been performed on JET which was used as an experimental testbed of a polarimetric Thomson scattering diagnostic technique. During a recent campaign, one of the filter polychromators of the JET HRTS system was modified in order to detect the TS signal polarized perpendicularly to

the direction of the incident laser beam. Data has been collected in plasmas with $T_e \simeq 8$ keV, the analysis of the data is currently under way [55].

Experimental test of a polarimetric Thomson scattering diagnostic technique could be realized in high T_e regimes on the W7-X stellarator. According to [56], electron temperatures up to 10 keV have already been measured at relatively low density in the core region during initial plasma operation phase OP1.1 with the ECR heating system consisting of six gyrotrons and operating with about 4.3 MW of injected power. These results are consistent with transport simulations [57] predicting stationary values of $T_e \simeq 9$ keV at 5 MW of ECRH power. At present, the W7-X machine is under preparation for the next stage of operation OP1.2 with the test divertor unit. The ECRH system will be complemented by another 4 gyrotrons, increasing the heating power from 5 to 9 MW. In this later operation phase, one can expect a further increase of electron temperature up to 12–15 keV for low-density (10^{19} m^{-3} range) discharges [58]. These high T_e regimes could be effectively used for verification of the TS polarization concept on W7-X.

In addition to JET, an experiment to measure the depolarization of the TS radiation on the FTU has been proposed [59]. This project is presently in the design phase. In the FTU machine, plasma with T_e as high as 11 keV was obtained by central electron cyclotron heating [60]. Important features of the proposed experiments include a scattering angle $\theta \simeq 90°$ and F/2.7 collection optics [61]. The intensity of the unpolarized radiation is intended to be optimized by selecting a suitable polarization of the input laser beam.

Acknowledgments

The authors would like to acknowledge D D Ryutov for his interest to the work and useful suggestions, L Giudicotti for valuable comments and contributions, G V Stupakov for helpful advices and important insights and E Parke for his assistance and support.

This material is based on work supported by the US Department of Energy office of Science, Office of Fusion Energy Sciences under Award Nos. DE-FG02-85ER53212, DE-FC02-05ER54814, the US NSF Cooperative Agreement PHY-0821899 Center for Magnetic Self-Organization in Laboratory and Astrophysical Plasmas and the US ITER Project Office.

Appendix A. Scattering by single electron

A.1. Stokes vector components

The Stokes parameters of the incident and scattered radiation are defined by time-averaged electric field components (1)

$$\begin{aligned} S_0 &= \lim_{T\to\infty}\frac{1}{2T}\int_{-T}^{T}(E_x(t)E_x^*(t) + E_t(t)E_t^*(t))\mathrm{d}t,\\ S_1 &= \lim_{T\to\infty}\frac{1}{2T}\int_{-T}^{T}(E_x(t)E_x^*(t) - E_t(t)E_t^*(t))\mathrm{d}t,\\ S_2 &= \lim_{T\to\infty}\frac{1}{2T}\int_{-T}^{T}(E_x(t)E_t^*(t) + E_t(t)E_x^*(t))\mathrm{d}t,\\ S_3 &= \lim_{T\to\infty}\frac{i}{2T}\int_{-T}^{T}(E_x(t)E_t^*(t) - E_t(t)E_x^*(t))\mathrm{d}t. \end{aligned} \tag{A1}$$

They are determined by the projections of $\mathbf{E}(t)$ onto the $(\mathbf{e}_x, \mathbf{t}_i)$ and $(\mathbf{e}_x, \mathbf{t}_s)$ axes for incident and scattered waves, respectively. Consider, for example, the Stokes vector $\mathbf{S}^{(i)}$ of the incident monochromatic wave (11)

$$\mathbf{E}_i = E_{ix}\mathbf{e}_x + E_{it}\mathbf{t}_i = E_0(\mathbf{e}'_x\cos\chi + \mathrm{i}\mathbf{e}'_y\sin\chi), \tag{A2}$$

where the ellipticity angle $\chi = \pm\arctan(b_2/b_1)$. Projecting (A2) onto the $\mathbf{e}_x$ and $\mathbf{t}_i$ axes gives the E_{ix} and E_{it} components

$$\begin{aligned} E_{ix} &= \cos\chi\cos\psi - \mathrm{i}\sin\chi\sin\psi,\\ E_{it} &= \cos\chi\sin\psi + \mathrm{i}\sin\chi\cos\psi. \end{aligned} \tag{A3}$$

Substituting (A3) in (A1) yields the Stokes vector of the fully polarized incident wave (2).

The dependencies of all quantities on the polarization state of the incident light are analyzed by plotting them along four boundaries of the polarization region $0 \leqslant \psi \leqslant \pi/2$, $0 \leqslant \chi \leqslant \pi/4$. The scattered field characteristics are expressed as functions of a parameter $0 \leqslant \xi \leqslant 4$. It describes the changes of the polarization angles $\cos 2\psi$ and $\cos 2\chi$ as some linear functions of ξ: $\cos 2\psi = \alpha\xi + \beta$, $\cos 2\chi = \gamma\xi + \delta$. The coefficients are selected in such a way that each of four boundaries corresponds to equal interval of ξ variation $\Delta\xi = 1$: $0 \leqslant \xi \leqslant 1 \rightarrow$ $(0 \leqslant \psi \leqslant \pi/2,\ \chi = 0)$; $1 \leqslant \xi \leqslant 2 \rightarrow (\psi = \pi/2,\ 0 \leqslant \chi \leqslant \pi/4)$; $2 \leqslant \xi \leqslant 3 \rightarrow (\pi/2 \geqslant \psi \geqslant 0,\ \chi = \pi/4)$; $3 \leqslant \xi \leqslant 4 \rightarrow (\psi = 0,\ \pi/4 \geqslant \chi \geqslant 0)$.

The particular case of a linearly polarized incident wave with $\chi = 0$ is considered in solution (37). The corresponding electric field amplitude $\mathbf{E}_i \| \mathbf{e}'_x$. The scattered wave propagation direction $\mathbf{s}$ is characterized by the polar and azimuth angles Θ and Φ which are defined with respect to the spherical system of coordinates determined by the unit vectors $\hat{\mathbf{x}} = \mathbf{i}$, $\hat{\mathbf{y}} = \mathbf{e}'_x \times \mathbf{i}$, $\hat{\mathbf{z}} = \mathbf{e}'_x$. The relationships between the variables θ and ψ and the angles Θ and Φ are as follows

$$\begin{aligned} \cos\theta &= \mathbf{s}\cdot\mathbf{i} = \mathbf{s}\cdot\hat{\mathbf{x}} = \sin\Theta\cos\Phi,\\ \cos\psi &= \mathbf{e}'_x\cdot\mathbf{e}_x = \hat{\mathbf{z}}\cdot[\mathbf{i}\times\mathbf{s}]/\sin\theta\\ &= (\mathbf{s}\cdot\hat{\mathbf{y}})/\sin\theta = \sin\Theta\sin\Phi/\sin\theta. \end{aligned} \tag{A4}$$

A.2. Unpolarized and polarized parts of the coherency matrix

The principle of decomposition is specified by equation (8). Expressing four unknown coefficients B, C, D, $D^\star$ in terms of A and four elements of the matrix $\hat{\mathbf{J}}$ and substituting in equation $BC - DD^\star = 0$ yields quadratic equation for A. It

has a unique solution for nonnegative A, B and C

$$\begin{aligned}
A &= \frac{1}{2}(J_{xx} + J_{yy} - \sqrt{(J_{xx} + J_{yy})^2 - 4\det|\hat{\mathbf{J}}|}) \\
&= \frac{1}{2}(S_0 - \sqrt{S_1^2 + S_2^2 + S_3^2}), \\
B &= \frac{1}{2}(J_{xx} - J_{yy} + \sqrt{(J_{xx} - J_{yy})^2 + 4J_{xy}Jyx}) \\
&= \frac{1}{2}(S_1 + \sqrt{S_1^2 + S_2^2 + S_3^2}), \\
C &= \frac{1}{2}(J_{yy} - J_{xx} + \sqrt{(J_{xx} - J_{yy})^2 + 4J_{xy}Jyx}) \\
&= \frac{1}{2}(\sqrt{S_1^2 + S_2^2 + S_3^2} - S_1), \\
D &= J_{xy} = (S_2 + \mathrm{i}S_3)/2, \quad D^\star = J_{yx} = (S_2 - \mathrm{i}S_3)/2. \qquad \text{(A5)}
\end{aligned}$$

The intensities of the unpolarized ($2A$) and polarized ($B + C$) components are consistent with the degree of polarization/depolarization defined by equation (3).

Consider the state of polarization described by the fully polarized part $\hat{\mathbf{J}}^{(\mathrm{pol})}$. The corresponding electric field can be treated as monochromatic with constant real amplitudes and phases

$$\begin{aligned}
E_x &= \mathrm{Re}\{E_{0x}\exp(-\mathrm{i}\omega t - \mathrm{i}\phi_x)\}, \\
E_y &= \mathrm{Re}\{E_{0y}\exp(-\mathrm{i}\omega t - \mathrm{i}\phi_y)\}. \qquad \text{(A6)}
\end{aligned}$$

The size (semi-axes ratio $b_2/b_1 = \tan\chi$) and the angle of inclination ψ of the polarization ellipse are expressed in terms of the parameters of equation (A6)

$$\begin{aligned}
\sin(2\chi) &= \frac{2E_{0x}E_{0y}\sin(\phi_x - \phi_y)}{E_{0x}^2 + E_{0y}^2}, \\
\tan(2\psi) &= \frac{2E_{0x}E_{0y}\cos(\phi_x - \phi_y)}{E_{0x}^2 - E_{0y}^2}. \qquad \text{(A7)}
\end{aligned}$$

Taking electric field components (A6) in a complex form and substituting into the polarization matrix (1) yields

$$\hat{\mathbf{J}}^{(\mathrm{pol})} = \begin{pmatrix} E_{0x}E_{0x}^\star & E_{0x}E_{0y}^\star\exp(\mathrm{i}\phi_x - \mathrm{i}\phi_y) \\ E_{0y}E_{0x}^\star\exp(\mathrm{i}\phi_y - \mathrm{i}\phi_x) & E_{0y}E_{0y}^\star \end{pmatrix}. \qquad \text{(A8)}$$

Comparing (A8) and (A7) shows that characteristics of the polarization ellipse associated with the fully polarized part are expressed in terms of the elements of $\hat{\mathbf{J}}^{(\mathrm{pol})}$ as follows

$$\begin{aligned}
\sin(2\chi) &= -\mathrm{i}\frac{J_{xy}^{(\mathrm{pol})} - J_{yx}^{(\mathrm{pol})}}{J_{xx}^{(\mathrm{pol})} + J_{yy}^{(\mathrm{pol})}}, \\
\tan(2\psi) &= \frac{J_{xy}^{(\mathrm{pol})} + J_{yx}^{(\mathrm{pol})}}{J_{xx}^{(\mathrm{pol})} - J_{yy}^{(\mathrm{pol})}}. \qquad \text{(A9)}
\end{aligned}$$

Rewriting these elements in terms of A, B, C and D results in equation (9).

A.3. Treatment of the square of a δ-function

If the limiting transition $T \to \infty$ was performed for linear quantities such as the electric field vector (18), then the singular δ-function would lead to a problematic square of a δ-function for quadratic combinations which must be correctly resolved. The problem has been treated by applying a phenomenological 'recipe' (see, for example, equation (10) in [15]) where one δ-function in the product is left as is while the second one is presented in the integral form

$$\begin{aligned}
S_0(\omega) &= |\mathbf{E}_0|^2 \lim_{T\to\infty} \frac{\delta(\omega - \omega_d)}{2T}\int_{-T}^{T} \mathrm{d}t\,\exp[\mathrm{i}(\omega - \omega_d)t] \\
&\to |\mathbf{E}_0|^2\delta(\omega - \omega_d). \qquad \text{(A10)}
\end{aligned}$$

Due to the first δ-function one should put $\omega = \omega_d$ in the integral kernel. This yields the desired limiting transition after integration over t.

In spite of its seeming effectiveness, formal use of this recipe does not provide a unique answer. The uncertainty originates from freedom in choosing the limits of integration in the integral presentation for the second δ-function. The integral presentation for any δ-function is still valid if, instead of $\pm T$, the limits of integration are chosen as $\pm\lambda T$ where λ is some constant. This invariance does not hold for the quadratic combination. Indeed, putting $\omega = \omega_d$ in the integral kernel yields, after integration over t, the result $\lambda|\mathbf{E}_0|^2\delta(\omega - \omega_d)$ which depends on λ and, therefore, is not a unique function of ω. It becomes a well-defined quantity when the limits of integration are not arbitrary but determined by the specific problem under consideration. Consider, for illustration, two different forms of the problem analyzed in [15, 18].

The original equation (4) in [18] for the Fourier component $\mathbf{E}_s^{[18]}(\omega)$ scales with the factors of $(1 - \beta_s)$ and ω as follows

$$\begin{aligned}
\mathbf{E}_s^{[18]} &\propto \int_{-T_{\mathrm{laser}}/2}^{T_{\mathrm{laser}}/2} \frac{\mathrm{d}t'\exp[\mathrm{i}\omega(1 - \beta_s)t' - \omega_i(1 - \beta_i)t']}{(1 - \beta_s)^2} \\
&\underset{T\to\infty}{\to} \frac{\delta[\omega(1 - \beta_s) - \omega_i(1 - \beta_i)]}{(1 - \beta_s)^2}. \qquad \text{(A11)}
\end{aligned}$$

The variable T is renamed T_{laser} to emphasize that the laser pulse length is used as the interval of integration over t'. The same time interval $T = T_{\mathrm{laser}}$ is used in the denominator of equation (7) in [18] to determine the mean power which, by definition, is the spectral *time-at-particle* power. According to the 'recipe' (A10), the product of the function $\delta[\omega(1 - \beta_s) - \omega_i(1 - \beta_i)]$ and its integral form (A11) yields the spectral intensity which represents the spectral *time-at-particle* power (consistent with equation (14) in [18])

$$P_{[18]}^{(\mathrm{single})} \propto \frac{\delta[\omega(1 - \beta_s) - \omega_i(1 - \beta_i)]}{(1 - \beta_s)^4} = \frac{\delta(\omega - \omega_d)}{(1 - \beta_s)^5}. \qquad \text{(A12)}$$

In [15], the time interval T is the time at the detector. The original integral form with the T-dependent limits of integration is not shown explicitly in [15]. Instead, its limiting δ-function form is presented by equation (7) which is identical to the limiting expression in the rhs of (A11). The original integral form is also the same as (A11) but with the limits of integration expressed in terms of T from the substitution $T_{\rm laser} = T/(1-\beta_s)$ given by the retardation equation (12)

$$\mathbf{E}_s^{[15]} \propto \int_{-\frac{T}{2(1-\beta_s)}}^{\frac{T}{2(1-\beta_s)}} \frac{\mathrm{d}t' \exp[\mathrm{i}\omega(1-\beta_s)t' - \omega_i(1-\beta_i)t']}{(1-\beta_s)^2} \underset{T\to\infty}{\to} \frac{\delta[\omega(1-\beta_s)-\omega_i(1-\beta_i)]}{(1-\beta_s)^2}. \tag{A13}$$

This substitution is crucial for the mean spectral power calculation because the time interval at the detector T, rather than $T_{\rm laser}$, is in the corresponding denominator in [15].

The limits of integration in (A13) are rescaled compared to (A11). This situation is equivalent to the illustrative example (A10) with $\lambda = 1/(1-\beta_s)$. Using the phenomenological recipe for treatment of the square of a δ-function yields the scaling of the spectral *time-at-observer* power on the detector

$$P_{[15]}^{(\rm single)} \propto \frac{\delta[\omega(1-\beta_s)-\omega_i(1-\beta_i)]}{(1-\beta_s)^5} = \frac{\delta(\omega-\omega_d)}{(1-\beta_s)^6}. \tag{A14}$$

This result for $P_{[15]}^{(\rm single)}$ is different from $P_{[18]}^{(\rm single)}$. The difference was mistakenly interpreted in [18] as a result of the mathematical error in transforming the square of a δ-function in [15]. In point of fact, both expressions (A12) and (A14) are correct representations of the two different *time-at-particle* and *time-at-observer* powers which are in agreement with the general relationship (13). This justifies the set of transformations (7)–(10) in [15] performed by the extraction of a factor $(1-\beta_s)$ from within the δ-function.

A.4. Amplitude of the TS field

The starting point is the Lienard–Wiechert expression for the scattered electric field $\mathbf{E}_s$ emitted by an electron moving along the unperturbed trajectory

$$\mathbf{R}(t') = \mathbf{R}_0^{(\rm i)} + \mathbf{v}t' \tag{A15}$$

and oscillating in the field (11) of the incident monochromatic wave $\boldsymbol{\mathcal{E}}_i(\mathbf{r}', t')$

$$\mathbf{E}_s(\mathbf{r}, t) = \frac{r_0}{r}\frac{\sqrt{1-\beta^2}}{(1-\beta_s)^2}\int \mathrm{d}\mathbf{r}' \int \mathrm{d}t' \delta[t' - t + (r - \mathbf{s}\cdot\mathbf{r}')/c]\delta(\mathbf{r}' - \mathbf{R}(t'))\hat{\mathbf{\Pi}}\cdot\boldsymbol{\mathcal{E}}_i(\mathbf{r}', t'). \tag{A16}$$

We consider here an elementary process of scattering within the scope of the infinite scattering volume model treated in section II (A, B, C) of [15]. The tensor $\hat{\mathbf{\Pi}}$ describes the transformation of polarization in the process of scattering on a single electron

$$\hat{\mathbf{\Pi}}\cdot\boldsymbol{\mathcal{E}}_i = -(1-\beta_s)(1-\beta_i)\boldsymbol{\mathcal{E}}_i + [\beta_E(\cos\theta - \beta_s) + (1-\beta_i)(\mathbf{s}\cdot\boldsymbol{\mathcal{E}}_i)]\mathbf{s} + [\beta_E(1-\cos\theta) - (1-\beta_i)(\mathbf{s}\cdot\boldsymbol{\mathcal{E}}_i)]\boldsymbol{\beta} - \beta_E(1-\beta_s)\mathbf{i}, \tag{A17}$$

where $\beta_E = \boldsymbol{\beta}\cdot\boldsymbol{\mathcal{E}}_i$.

The electric field $\mathbf{E}_s(\mathbf{r}, t)$ represents the scattered field at the remote position $\mathbf{r}$ on the detector at time t. We truncate the field $\mathbf{E}_s(\mathbf{r}, t)$ within a time interval $|t| \leqslant T$ according to (15). The Fourier image of the truncated signal is obtained by integrating over t from $-T$ to T. Performing integration over t' as shown in [14] yields the final result in the form (26), where the scalar function $f^{(T)}(\omega, \boldsymbol{\beta})$ is

$$f^{(T)}(\omega, \boldsymbol{\beta}) = \exp(\mathrm{i}\omega_d r/c - \mathrm{i}(\mathbf{k}_s - \mathbf{k}_i)\cdot\mathbf{R}_0)\frac{r_0}{r}\frac{\sqrt{1-\beta^2}}{(1-\beta_s)^3} \times \sqrt{\frac{2}{\pi}}\frac{\sin(\Omega T)}{\Omega}, \quad \Omega = \omega - \omega_d. \tag{A18}$$

Appendix B. Mueller matrix for averaging with the ITT weighting factor

To illustrate the importance of the specific form of the weighting factor the technique of exact analytical integration is applied to the case of the weighting factor $\propto (1-\beta^2)/(1-\beta_s)^6$ that was used in [9] for calculations to the lowest linear order in $T_e/m_e c^2 \ll 1$. The analytical results for the sixth power weighting factor are represented by the Mueller matrix $\hat{\mathbf{h}}$ defined by equation (48)

$$\begin{aligned}
h_{00} &= 1 + u^2 + 2G(\mu)\left(5 - 6u + u^2 + \frac{84(1-u)^2}{\mu^2}\right) + \frac{4(17-9u)(1-u)}{\mu^2} + \frac{672(1-u)^2}{\mu^4},\\
h_{01} &= h_{10} = (1-u^2)\left(1 + 4G(\mu) + \frac{16}{\mu^2}\right),\\
h_{11} &= 1 + u^2 + 6\left(1 + \frac{24}{\mu^2}\right)(1-u)^2 G(\mu) + \frac{48(1-u)^2}{\mu^2} + \frac{576(1-u)^2}{\mu^4},\\
h_{22} &= -2u - 6\left(1 + \frac{24}{\mu^2}\right)(u-1)^2 G(\mu) - \frac{576(u-1)^2}{\mu^4} - \frac{48(u-1)^2}{\mu^2},\\
h_{33} &= 2u - 2G(\mu)\left(1 - 6u + 5u^2 + \frac{60(1-u)^2}{\mu^2}\right) + \frac{4(7-15u)(1-u)}{\mu^2} + \frac{480(1-u)^2}{\mu^4}.
\end{aligned} \tag{B1}$$

Comparing the two Mueller matrices $\hat{\mathbf{m}}$ and $\hat{\mathbf{h}}$ shows that they are sensitive to the specific form of the weighting factor. For example, the off-diagonal elements $m_{01} = m_{10} = \sin^2\theta$ are the same as in cold plasma while the equivalent elements of the matrix $\hat{\mathbf{h}}$ are substantial functions of T_e.

Appendix C. Frequency-resolved Mueller matrix

The integration over $\boldsymbol{\beta}$ is performed in (50) in a coordinate system $(\mathbf{e}_x, \mathbf{e}_y, \mathbf{e}_z)$ with the z-axis directed along $\mathbf{k}_s - \mathbf{k}_i$ such that $\mathbf{e}_z = (\mathbf{k}_s - \mathbf{k}_i)/|\mathbf{k}_s - \mathbf{k}_i| = (\mathbf{s}(X+1) - \mathbf{i})/k$, $\mathbf{e}_y = \mathbf{e}_z \times \mathbf{e}_x$ where $\mathbf{e}_x = [\mathbf{i} \times \mathbf{s}]/\sin\theta$ is the unit vector normal to the scattering plane while the dimensionless wave vector k and the frequency shift X are, respectively, $k = \sqrt{X^2 + 2(X+1)(1-u)}$, $X = \omega/\omega_i - 1$. In this reference frame, the argument of the δ-function in (50) takes a form which allows for direct integration over β_z: $\delta(\omega - \omega_i(1-\beta_i)/(1-\beta_s)) = (1-\beta_s)\delta[\omega - \omega_i - \boldsymbol{\beta}\cdot(\mathbf{k}_s - \mathbf{k}_i)c] = (1-\beta_s)\delta(\beta_\omega - \beta_z)/(\omega_i k)$, where $\beta_\omega = X/k$. This leads to a double integral of a function of two variables β_x and β_y over a circular area $\beta_x^2 + \beta_y^2 \leqslant 1 - \beta_\omega^2$ while the β_z component is fixed in the integrand, $\beta_z = \beta_\omega$. Four elements of the matrix $\hat{\mathbf{W}}$ are proportional to $b \propto \beta_x$. They average to zero after integration over β_x using the same arguments as in section 5.1. The remaining five elements are integrated in the polar coordinate system $(\beta_\perp, \phi)$ such that $\beta_x = \beta_\perp\cos\phi$ and $\beta_y = \beta_\perp\sin\phi$ where $0 \leqslant \beta_\perp^2 \leqslant 1 - \beta_\omega^2$ and $0 \leqslant \phi \leqslant 2\pi$.

Consider, first, integration over the polar angle ϕ in the dimensionless matrix $\hat{\mathbf{m}}(\omega, \mu, \theta)$ obtained after integration over β_z in the integral (50) and normalized similar to (45) but with the different normalization constant C_0/ω_i. The result of integration over ϕ is defined as the matrix $\hat{\mathbf{m}}^{(\phi)}(\omega, \beta_\perp)$

$$\hat{\mathbf{m}}^{(\phi)}(\omega, \beta_\perp) = \int_0^{2\pi} \frac{\hat{\mathbf{W}}(\beta_\perp, \phi)\mathrm{d}\phi}{(1-\beta_s)^4}. \tag{C1}$$

The five non-zero elements of the matrix $\hat{\mathbf{m}}^{(\phi)}(\omega, \beta_\perp)$ are determined by the corresponding elements of the matrix $\hat{\mathbf{W}}(\beta_\perp, \phi)$. The ϕ-dependencies enter these elements through the factors β_i, β_s and β_x^2 in a, b and c functions given by (27). Instead of expressing β_i, β_s and β_x in terms of ϕ we express β_i and β_x^2 in terms of the whole combination $(1-\beta_s)$ by making use of the two additional relationships. First, due to the δ-function in (50), the combination $(1-\beta_i)/(1-\beta_s)$ is equal to the ϕ-independent quantity $\omega/\omega_i = X + 1$ so that the factor β_i can be expressed in terms of $1 - \beta_s$

$$1 - \beta_i = \frac{\omega}{\omega_i}(1-\beta_s) \to \beta_i = 1 - (X+1)(1-\beta_s). \tag{C2}$$

Secondly, the vector $\boldsymbol{\beta}$ can be decomposed as $\boldsymbol{\beta} = \beta_x\mathbf{e}_x + \boldsymbol{\beta}_{sc}$, where $\boldsymbol{\beta}_{sc}$ is the projection of $\boldsymbol{\beta}$ on the scattering plane. This component is presented as a superposition of its non-orthogonal projections on $\mathbf{i}$ and $\mathbf{s}$ such that $\boldsymbol{\beta}_{sc} = r_s\mathbf{s} + r_i\mathbf{i}$. The non-orthogonal components are expressed in terms of the orthogonal components $\beta_s = (\boldsymbol{\beta}_{sc}\cdot\mathbf{s})$ and $\beta_i = (\boldsymbol{\beta}_{sc}\cdot\mathbf{i})$: $r_s = (\beta_s - \beta_i u)/(1-u^2)$, $r_i = (\beta_i - \beta_s u)/(1-u^2)$. Then, equation $\beta_x^2 = \beta^2 - \beta_{sc}^2 = \beta^2 - r_s^2 - r_i^2 - 2ur_ir_s$ yields an expression for β_x^2 in terms of β_i, β_s and $\beta_\perp$

$$\beta_x^2 = \beta_\perp^2 + \beta_\omega^2 - (\beta_i^2 + \beta_s^2 - 2\beta_i\beta_s u)/(1-u^2), \tag{C3}$$

where β^2 is written as $\beta^2 = \beta_\perp^2 + \beta_z^2$ in the coordinate system $(\mathbf{e}_x, \mathbf{e}_y, \mathbf{e}_x)$ while the δ-function is taken into account by putting $\beta_z = \beta_\omega$.

The factors a and c are quadratic, and b^2 is fourth order polynomial functions of the variables β_i and β_s. Because of these interrelations, expressing β_i and β_x^2 in terms of $(1-\beta_s)$ and substituting in $\hat{\mathbf{W}}(\beta_\perp, \phi)$ gives fourth order polynomial functions of $(1-\beta_s)$. Dividing by the factor $(1-\beta_s)^4$ in the denominator of (C1) and performing straightforward algebraic transformations gives fourth order polynomials of the inverse ratio $1/(1-\beta_s)$ with the coefficients $B_{ij}^{(n)}$ depending on X, u and $\beta_\perp^2$. Thus, all dependencies on ϕ in (52) are reduced to the form $\sum_{n=0}^{n=4} B_{ij}^{(n)}/(1-\beta_s)^n$ with four ϕ-dependent terms at $n = 1, \ldots 4$ and one ϕ-independent term related to $n = 0$. For illustration, typical values of the $B_{ij}^{(n)}$ coefficients related to the particular case of $\hat{\mathbf{m}}_{00}^{(\phi)}$ element are as follows

$$\begin{aligned} &B_{00}^{(0)} = 2(1+X)^2,\ B_{00}^{(1)} = B_{00}^{(3)} = 0,\\ &B_{00}^{(2)} = -2(1+X)(1-u)(1-\beta^2),\\ &B_{00}^{(4)} = (1-u)^2(1-\beta^2)^2. \end{aligned} \tag{C4}$$

In all other non-zero elements of the matrix $\hat{\mathbf{W}}(\beta_\perp, \phi)$, the coefficients $B_{ij}^{(n)}$ do not depend on $\beta^2 = \beta_\perp^2 + \beta_\omega^2$ at $n = 0, 1$, are linear functions of β^2 at $n = 2, 3$ and quadratic functions of β^2 at $n = 4$ (see supplementary material). These general properties of the $B_{ij}^{(n)}$ coefficients are important for further integration over $\beta_\perp$.

In the coordinate system $(\mathbf{e}_x, \mathbf{e}_y, \mathbf{e}_z)$, the expression for $1 - \beta_s$ takes the form, $1 - \beta_s = 1 - \beta_y s_y - \beta_z s_z = \beta_\perp s_y(H - \sin\phi)$, where $H = (1 - \beta_\omega s_z)/\beta_\perp s_y$ while $s_z = (\mathbf{s}\cdot\mathbf{e}_z) = (X + 1 - u)/k$ and $s_y = (\mathbf{s}\cdot\mathbf{e}_y) = \sqrt{1-u^2}/k$. Integrating the fourth order polynomial function of $1/(1-\beta_s)$ over ϕ leads to the integrals of the form

$$\begin{aligned} \int_0^{2\pi} \frac{B_{ij}^{(n)}\mathrm{d}\phi}{(1-\beta_s)^n} &= \int_0^{2\pi} \frac{B_{ij}^{(n)}\mathrm{d}\phi}{(\beta_\perp s_y)^n(H - \sin\phi)^n}\\ &= \frac{(\beta_\perp s_y)^{n-1}G_{n-1}B_{ij}^{(n)}}{[(1-\beta_\omega s_z)^2 - \beta_\perp^2 s_y^2]^{(2n-1)/2}},\ n = 1, \ldots 4, \end{aligned} \tag{C5}$$

where G_{n-1} are $n-1$ order polynomials of H. Explicit form of the polynomials and the structure of the rhs of (C5) are determined by the exact analytic integrals

$$\begin{aligned} &\int_0^{2\pi} \frac{\mathrm{d}\phi}{H - \sin\phi} = \frac{2\pi}{(H^2-1)^{1/2}},\\ &\int_0^{2\pi} \frac{\mathrm{d}\phi}{(H - \sin\phi)^2} = \frac{2\pi H}{(H^2-1)^{3/2}},\\ &\int_0^{2\pi} \frac{\mathrm{d}\phi}{(H - \sin\phi)^3} = \frac{\pi(2H^2+1)}{(H^2-1)^{5/2}},\\ &\int_0^{2\pi} \frac{\mathrm{d}\phi}{(H - \sin\phi)^4} = \frac{\pi H(2H^2+3)}{(H^2-1)^{7/2}} \end{aligned} \tag{C6}$$

from which follows that the products $(\beta_\perp s_y)^{n-1}G_{n-1}$ do not depend on $\beta_\perp$ at $n = 1,\ 2$ and are linear function of $\beta_\perp^2$ at $n = 3,\ 4$. Combining these dependencies with the $\beta_\perp^2$-dependent coefficients $B_{ij}^{(n)}$ shows that the resulting coefficients of the fractional exponents in equation (53), $A_{ij}^{(n)} = (\beta_\perp s_y)^{n-1}G_{n-1}B_{ij}^{(n)}$, do not depend on $\beta_\perp^2$ at $n = 1$, are linear functions of $\beta_\perp^2$ at $n = 2$, quadratic functions of $\beta_\perp^2$ at $n = 3$ and cubic functions at $n = 4$. Using example (C4) shows how these general properties are realized in the particular case of the $\hat{\mathbf{m}}_{00}^{(\phi)}$ element

$$\begin{aligned} A_{00}^{(0)} &= 4\pi(1+X)^2,\ A_{00}^{(1)} = A_{00}^{(3)} = 0,\ A_{00}^{(2)} \\ &= -4\pi(1-\beta_\omega s_z)(1+X)(1-u)(1-\beta_\omega^2-\beta_\perp^2), \\ A_{00}^{(4)} &= \pi(1-u)^2(1-\beta_\omega s_z)[2(1-\beta_\omega s_z)^2 \\ &\quad + 3\beta_\perp^2 s_y^2](1-\beta_\omega^2-\beta_\perp^2)^2, \end{aligned} \tag{C7}$$

where the factor $A_{00}^{(0)}$ is added to describe the contribution from the ϕ-independent term at $n = 0$.

The next step is the integration over the 'radial' variable $\beta_\perp$ according to

$$\begin{aligned} \hat{\mathbf{m}}(\omega,\mu,u) = \frac{1}{k}\int_0^{\sqrt{1-\beta_\omega^2}} &\beta_\perp \mathrm{d}\beta_\perp (1-\beta_\omega^2-\beta_\perp^2) \\ &\times f_M(\beta_\perp)\hat{\mathbf{m}}^{(\phi)}(\omega,\beta_\perp). \end{aligned} \tag{C8}$$

Instead of the integration over $\beta_\perp$ it is useful to introduce a new variable of integration t such that $\beta_\perp^2 = (1-\beta_\omega^2)(1-1/t^2)$ where $1 \leqslant t \leqslant \infty$. This variable represents the relativistic factor $\gamma = (1-\beta^2)^{-1/2}$ normalized to $1\big/\sqrt{1-\beta_\omega^2}$. With the new variable of integration the argument of the fractional exponents in (53) is transformed to a compact form (r^2+t^2)

$$\begin{aligned} &\frac{A_{ij}^{(n)}(\beta_\perp)}{[(1-\beta_\omega s_z)^2-\beta_\perp^2 s_y^2]^{(2n-1)/2}} \\ &\quad = \frac{(kt)^{2n-1}A_{ij}^{(n)}(t)}{(1-u)^{2n-1}(r^2+t^2)^{(2n-1)/2}},\ n = 1,\ldots 4 \end{aligned} \tag{C9}$$

where $r^2 = 2(X+1)(1+u)/k^2$. In the numerator of the rhs of (C9), the transformation to the variable t leads to a combination $Q_{ij}^{(n)} = t^{2n-1}A_{ij}^{(n)}(t)$. Due to the properties of the $A_{ij}^{(n)}(\beta_\perp)$ dependencies this combination can be expressed in the general case as a product of the linear function t and $n-1$ (or less) order polynomial function of t^2. As an example, the values of $Q_{00}^{(n)}$ are shown below at $n = 1,\ldots 4$ for the particular case of $\hat{\mathbf{m}}_{00}^{(\phi)}$ element considered in equation (C7).

$$\begin{aligned} Q_{00}^{(1)} &= Q_{00}^{(3)} = 0,\ Q_{00}^{(2)} = -4\pi t(1+X) \\ &\quad \times (1-u)(1-\beta_\omega s_z)(1-\beta_\omega^2), \\ Q_{00}^{(4)} &= \pi t(1-u)^2(1-\beta_\omega s_z)(1-\beta_\omega^2)^2 \\ &\quad \times [2(1-\beta_\omega s_z)^2 t^2 + 3(1-\beta_\omega^2)s_y^2(t^2-1)]. \end{aligned} \tag{C10}$$

Expressing t^2 in the polynomial functions as a combination $t^2 \to (t^2+r^2)-r^2$ allows us to eliminate the t^2-dependencies in the numerators by combining them with the fractional exponents $(r^2+t^2)^{(2n-1)/2}$ in the denominators. This determines the structure of the resulting integral over t

$$\begin{aligned} \hat{\mathbf{m}}(X,\mu,u) = \frac{\mu}{K_2(\mu)k}\int_1^\infty \mathrm{d}t\,\exp\left(-\mu t\Big/\sqrt{1-\beta_\omega^2}\right) \\ \times\left(\hat{\mathbf{w}}^{(0)}(X,u) + t\sum_{n=1}^{4}\frac{\hat{\mathbf{w}}^{(n)}(X,u)}{(r^2+t^2)^{(2n-1)/2}}\right), \end{aligned} \tag{C11}$$

where $\hat{\mathbf{w}}^{(n)}(X,u)$ are t-independent 4×4 matrices. The first term is integrated exactly while the second proportional to t term is integrated by parts with the use of the substitution $\mu\mathrm{d}t\exp(-\mu t\big/\sqrt{1-\beta_\omega^2}) = -\sqrt{1-\beta_\omega^2}\ \mathrm{d}\left[\exp(-\mu t/\sqrt{1-\beta_\omega^2})\right]$. The factors proportional to t^2 that appear after integration by parts are elimiated by combining them with the fractional exponents in the corresponding denominators. This yields five non-zero elements of the frequency-resolved Mueller matrix in a compact form (55) of a superposition of well converged integrals $E^{(n)}(p,r)$ with 25 coefficients, 13 of which are different rational functions of X and u

$$\begin{aligned} C_{00}^{(0)} &= C_{11}^{(0)} = \frac{(X+1)^2[(X+2)^4 - 4k^2(u+1)(X+1)]}{kK_2(\mu)(X+2)^4}, \\ C_{00}^{(1)} &= C_{33}^{(1)} = \frac{4(X+1)^2(X+2)}{k^2K_2(\mu)}, \\ C_{00}^{(2)} &= -\frac{4(X+1)^2(X+2)[9(u+1)(X+1)+2(X+2)^2]}{k^4K_2(\mu)}, \\ C_{00}^{(3)} &= \frac{20(u+1)(X+1)^3(X+2)[3(u+1)(X+1)+4(X+2)^2]}{k^6K_2(\mu)}, \\ C_{00}^{(4)} &= -C_{01}^{(4)} = C_{11}^{(4)} = -\frac{140(u+1)^2(X+1)^4(X+2)^3}{k^8K_2(\mu)}, \end{aligned}$$

$$C_{01}^{(0)} = \frac{4k\,(u+1)(X+1)^3}{K_2(\mu)(X+2)^4},$$
$$C_{01}^{(1)} = C_{11}^{(1)} = C_{22}^{(1)} = C_{22}^{(4)} = C_{33}^{(3)} = C_{33}^{(4)} = 0,$$
$$C_{01}^{(2)} = \frac{24(u+1)(X+1)^3(X+2)}{k^4K_2(\mu)},$$

$$C_{01}^{(3)} = -\frac{60(u+1)(X+1)^3(X+2)[(u+1)(X+1)+(X+2)^2]}{k^6K_2(\mu)},$$
$$C_{11}^{(2)} = -C_{22}^{(2)} = -\frac{4(X+1)^2(X+2)[3(u+1)(X+1)+(X+2)^2]}{k^4K_2(\mu)},$$
$$C_{11}^{(3)} = \frac{20(u+1)(X+1)^3(X+2)[3(u+1)(X+1)+2(X+2)^2]}{k^6K_2(\mu)},$$
$$C_{22}^{(0)} = C_{33}^{(0)} = \frac{(X+1)^2[4u(X+1)-X^2]}{kK_2(\mu)(X+2)^2},$$
$$C_{22}^{(3)} = -\frac{40(u+1)(X+1)^3(X+2)^3}{k^6K_2(\mu)},$$
$$C_{33}^{(2)} = -\frac{12(u+1)(X+1)^3(X+2)}{k^4K_2(\mu)}. \tag{C12}$$

Consider an alternative derivation of the approximate solution (59) by using a different method of expansion of (55) in powers of T_e/m_ec^2. Equation (55) can be rewritten as follows

$$\hat{\mathbf{m}}_{ij}(X,\mu,u) = \left(C_{ij}^{(0)} + \sum_{n=1}^{n=4} C_{ij}^{(n)}(X,u)E^{(n)}(p,r)\exp(p)\right)E^{(0)}(p). \tag{C13}$$

Introducing the new variable of integration $z = p(t-1)$, the combination $I^{(n)}(p,r) = \exp(p)E^{(n)}(p,r)$ takes the form

$$I^{(n)}(p,r) = \int_1^\infty \frac{\mathrm{d}t\exp[-p(t-1)]}{(r^2+t^2)^{(2n+1)/2}} = \frac{1}{p}\int_0^\infty \frac{\mathrm{d}z\exp(-z)}{(r^2+(z/p+1)^2)^{(2n+1)/2}}. \tag{C14}$$

Due to the exponential function, the main contribution to the integral comes from $z \leqslant 1$. Then, the factor $(r^2+(z/p+1)^2)^{-(2n+1)/2}$ can be expanded in the Taylor power series of z/p at large $p \propto \mu \gg 1$. The zero order term

$$I_0^{(n)}(p,r) = \frac{1}{p(r^2+1)^{(2n+1)/2}} \tag{C15}$$

corresponds to the linear in T_e/m_ec^2 term in large brackets in (C13) that reproduces the approximate solution (59). This solution is presented as a sum of the two terms, $\hat{\mathbf{m}}^{(1)}(X,\mu,u) = (\hat{\mathbf{m}}' + \delta\hat{\mathbf{m}})E_0(p)$, where

$$\hat{\mathbf{m}}'_{ij}(X,\mu,u) = C_{ij}^{(0)}, \quad \delta\hat{\mathbf{m}}_{ij}(X,\mu,u) = \frac{1}{p}\sum_{n=1}^{n=4}\frac{C_{ij}^{(n)}(X,u)}{(r^2+1)^{(2n+1)/2}}. \tag{C16}$$

The degree of depolarization caused by small $\delta\hat{\mathbf{m}}$ term is also small, $D(X) \ll 1$. Then, function $D(X)$ can be approximated as follows

$$D(X) = (S_0^{(s)2} - S_1^{(s)2} - S_2^{(s)2} - S_3^{(s)2})/(2S_0^{(s)2}) \simeq \left((\delta\hat{\mathbf{m}}\cdot\mathbf{S}^{(i)})_0 - (\delta\hat{\mathbf{m}}\cdot\mathbf{S}^{(i)})_1 - (\delta\hat{\mathbf{m}}\cdot\mathbf{S}^{(i)})_2 - (\delta\hat{\mathbf{m}}\cdot\mathbf{S}^{(i)})_3\right)/(\hat{\mathbf{m}}'\cdot\mathbf{S}^{(i)})_0^2. \tag{C17}$$

Equation (C17) is a consequence of the identity $(\hat{\mathbf{m}}'\cdot\mathbf{S}^{(i)})_0^2 - (\hat{\mathbf{m}}'\cdot\mathbf{S}^{(i)})_1^2 - (\hat{\mathbf{m}}'\cdot\mathbf{S}^{(i)})_1^2 - (\hat{\mathbf{m}}'\cdot\mathbf{S}^{(i)})_3^2 \equiv 0$. The Gaussian part of the spectral profile $E^{(0)}(p)$ cancels out in expression for $D(X)$. The characteristic values of $D(X)$ scale with the temperature as T_e/m_ec^2 and vary with X on a scale of order unity.

References

[1] Sheffield J *et al* 2010 *Plasma Scattering of Electromagnetic Radiation* 2nd edn (New York: Elsevier)
[2] Hutchinson I H 2001 *Principles of Plasma Diagnostics* (Cambridge: Cambridge University Press)
[3] Naito O *et al* 1993 *Phys. Fluids* B **5** 4256
[4] Beausang K V and Prunty S L 2008 *Plasma Phys. Control. Fusion* **50** 095001
[5] Salzmann H 1987 Thomson scattering *Proc. Varenna's Course and Workshop on Basic and Advanced Diagnostic Techniques for Fusion Plasma* vol II *(Varenna, Italy, 3–13 September 1986)* p 477
[6] Theimer O and Hicks W 1968 *Phys. Fluids* **11** 1045
[7] Orsitto F and Tartoni N 1999 *Rev. Sci. Instrum.* **70** 798
[8] Zhuravlev V A and Petrov G D 1980 *Sov. J. Plasma Phys.* **6** 113

[9] Segre S E and Zanza V 2000 *Phys. Plasmas* **7** 2677
[10] Mirnov V V *et al* 2013 Electron kinetic effects on interferometry, polarimetry and Thomson scattering in burning plasmas *Proc. IAEA Fusion Energy Conf., ITR/P5-32 (San-Diego, USA, 8–13 October 2012)* (Vienna: IAEA) p 604
[11] Mirnov V V *et al* 2015 *Fusion Reactor Diagnostics (Varenna, Italy, 9–13 September 2013); AIP Conf. Proc.* **1612** 157
[12] Mirnov V V *et al* 2014 *Rev. Sci. Instrum.* **85** 11D302
[13] Parke E *et al* 2014 *Proc. 16th Int. Symp. on Laser-Aided Plasma Diagnostics (Madison, WI, 2013); J. Instrum.* **9** C02030
[14] Mirnov V V *et al* 2016 *Phys. Plasmas* **23** 052108
[15] Pechacek R E and Trivelpiece A W 1967 *Phys. Fluids* **10** 1688
[16] Prunty S L 2014 *Phys. Scr.* **89** 128001
[17] Landau L D and Lifshitz E M 2005 *The Classical Theory of Fields* 4th English edn (New York: Elsevier)
[18] Kukushkin A B 1981 *Sov. J. Plasma Phys.* **7** 63
[19] Giudicotti L and Pasqualotto R 2015 *Plasma Phys. Control. Fusion* **57** 035001
[20] Giudicotti L and Pasqualotto R 2015 *Plasma Phys. Control. Fusion* **57** 125015
[21] Giudicotti L *et al* 2016 *J. Instrum* **11** C01071
[22] Giudicotti L *et al* 2016 Extending the T_e range of the ITER core Thomson scattering system by detecting the unpolarized scattering radiation *Poster 6.2.38, 21st Topical Conf. on High-Temperature Plasma Diagnostics (Madison, 2016); Nucl. Fusion* in preparation
[23] Born M and Wolf E 1980 *Principles of Optics* (Oxford: Pergamon)
[24] Degl'innocenti E L and Landolfi M 2005 *Polarization in Spectral Lines* (Dordrecht: Kluwer)
[25] Collett E 1993 *Polarized Light (Fundamentals and Applications)* (New York: Dekker)
[26] Goldstein D H 2011 *Polarized Light* 3rd edn (Boca Raton, FL, London: CRC Press, Taylor and Francis Group)
[27] Rytov S M *et al* 1988 *Principles of Statistical Radiophysics* vol 2 (Berlin: Springer) p 99
[28] Stupakov G V 2013 private communication
[29] Sheffield J 1975 *Plasma Scattering of Electromagnetic Radiation* (New York: Academic)
[30] Bindslev H 1991 *Plasma Phys. Control. Fusion* **33** 1775
[31] Bindslev H 1992 *PhD Thesis* Oxford University
[32] Tsytovich V N 2013 *Phys.—Usp.* **56** 180
[33] Ratcliffe J A 1959 *The Magneto-Ionic Theory and its Applications to the Ionosphere* (Cambridge: Cambridge University Press)
[34] Rytov S M *et al* 1989 *Principles of Statistical Radiophysics* vol 3 (Berlin: Springer) p 231
[35] Abramowitz M and Stegun I A 1964 *Handbook of Mathematical Functions* (Washington, DC: US Department of Commerce, National Bureau of Standards)
[36] Ginzburg V L *et al* 1968 *Sov. Phys.—Usp.* **11** 34
[37] Scheuer P A G 1968 *Astrophys. J.* **151** L139
[38] Walsh M J *et al* 2006 *Rev. Sci. Instrum.* **77** 10E525
[39] Naylor G A *et al* 2012 *Proc. 15th Int. Conf. on Laser-Aided Plasma Diagnostics (Jeju, Korea, 2011); J. Instrum.* **7** C03043
[40] Brosseau C 1998 *Fundamentals of Polarized Light: A Statistical Optics Approach* (New York: Wiley)
[41] Wolf E 2007 *Introduction to the Theory of Coherence and Polarization of Light* (Cambridge: Cambridge University Press)
[42] Martinez-Herrero R *et al* 2009 *Characterization of Partially Polarized Light Fields* (Berlin: Springer)
[43] Wolfram Research, Inc. 2010 *Mathematica Version 8.0* (Champaign, IL: Wolfram Research)
[44] Williamson J H and Clarke M E 1971 *J. Plasma Phys.* **6** 211
[45] Zhuravlev V A and Petrov G D 1979 *Sov. J. Plasma Phys.* **5** 3
[46] Sheffield J 1972 *Plasma Phys.* **14** 783
[47] Mattioli M *et al* 1975 *Plasma Phys.* **17** 165
[48] Matoba T *et al* 1979 *Japan J. Appl. Phys.* **18** 1127
[49] Selden A C 1980 *Phys. Lett.* A **79** 405
[50] Palastro J P 2010 *Phys. Rev.* E **81** 036411
[51] Sheffield J 2012 private communication
[52] Kukushkin A B and Kogan V I 1981 *Sov. J. Plasma Phys.* **7** 669
[53] Kurskiev G S *et al* 2015 *Nucl. Fusion* **7** 053024
[54] Bassan M *et al* 2016 *J. Instrum.* **11** C01052
[55] Giudicotti L J and Kempenaars M 2016 private communication
[56] Wolf R C *et al* 2016 First plasma operation of Wendelstein 7-X *Preprint: 2016 IAEA Fusion Energy Conf. (Kyoto, Japan, 17–22 October 2016)* OV/3-1 (Vienna: IAEA)
[57] Pedersen T S *et al* 2016 *Nucl. Fusion* **55** 126001
[58] Pedersen T S 2016 private communication
[59] Giudicotti L J and Orsitto F 2016 private communication
[60] Granucci G *et al* 2004 *Fusion Sci. Technol.* **45** 387–401
[61] Orsitto F *et al* 1995 *Rev. Sci. Instrum.* **66** 1167